Quantum optics in the infrared: Single-cycle THz field electro-optical sampling with single-photon detectors

Taylor Shields

Submitted in fulfilment of the requirements for the
Degree of Doctor of Philosophy

James Watt School of Engineering
College of Science and Engineering
University of Glasgow

April 5, 2023

Contents

Abstract

This thesis represents a summary of the activities I performed throughout my PhD, mainly on quantum optics in the infrared. The field of quantum optics was revolutionised by the experimental demonstration of correlated photon-pair generation via the non linear interaction known as spontaneous parametric down-conversion (SPDC). Quantum-enhanced optical systems utilising the unique properties of these quantum sources have blossomed in recent years particularly in the fields of quantum communications and quantum metrology. Currently, most measurements taking advantage of these non-classical sources have narrowed their focus on the near-infrared to telecommunications spectral region ($0.7 - 1.6\,\mu$m) with good reason. Going beyond this spectral range, at longer wavelengths, presents significant technological problems in both generation, manipulation and detection of mid-infrared radiation. Fundamental advantages such as reduced scattering and propagation losses in well-established fields presents a compelling case to investigate non-classical states within the mid-infrared window. This thesis details the challenges associated with delving into the $2\,\mu$m regime and demonstrates the realisation of a compact and robust quantum source of entangled photon-pairs using custom designed non-linear crystals and superconducting nanowire single-photon detectors (SNSPD). The demonstration of two-photon interference and polarisation entanglement at $2.1\,\mu$m provides a solution which could prove valuable in the implementation of future free-space daylight quantum communications and high sensitivity metrology. This

thesis follows up on this work by addressing a promising application of 2 μm sources in the field of integrated photonics. The testing of the performance of a type of novel hollow-core nested antiresonant nodeless fibre (HC-NANF) with mid-infrared radiation indicates high polarisation purity and low attenuation properties. This technology may provide the radical solution to ensure the future capacities of modern communication networks are met.

The proposal to employ the quantum properties of entangled photon states generated via SPDC to enhance detection in wavelengths far beyond the mid-infrared is a challenging concept. This thesis moves in the direction of the application of non-classical states for the metrological detection of terahertz (THz) radiation of which has garnered significant interest in countless areas of scientific endeavour in recent times. It tackles the enhanced phase estimation granted by using NOON states in metrology applications and takes the first step in utilising alternative detection strategies for measuring THz radiation. Traditional techniques for measuring or reconstructing THz electric fields rely on balanced detection using photodiodes with inherent shot-noise limitations on the system. Terahertz time-domain spectroscopy (THz-TDS) using electro-optic sampling (EOS) and ultrashort pulsed probes is typically employed to measure directly the electric field of THz radiation. This thesis reports on the first step in the direction of using non-classical states for THz detection demonstrating that electric fields can be measured with single-photon detectors using a squeezed vacuum as the optical probe. The approach achieves THz electro-optical sampling using phase-locked single-photon detectors at the shot-noise limit and thus paves the way toward quantum-enhanced THz sensing.

List of Figures

List of acronyms

SPDC Spontaneous Parametric Down-Conversion

SHG Second Harmonic Generation

PM Phase Matching

CPM Critical Phase Matching

NCPM Non-Critical Phase Matching

QPM Quasi-Phase Matching

PPLN Periodically-Poled Lithium Niobate

NIR Near-Infrared

QKD Quantum Key Distribution

LIGO Laser Interferometer Gravitational-Wave Observatory

HC-PBGF Hollow-Core Photonic Bandgap Fibre

TPA Two-Photon Absorption

DIQKD Device-Independent Quantum Key Distribution

MgO-PPLN Magnesium-Doped Periodically-Poled Lithium Niobate

SNSPD Superconducting Nanowire Single-Photon Detectors

TTTR Time-Tagged Time-Resolved

TTL Transistor-Transistor Logic

LVTTL Low Voltage Transistor-Transistor Logic

CAR Coincidence-to-Accidental Ratio

SM Single-Mode

OPO Optical Parametric Oscillator

AR Anti-Reflection

HOM Hong-Ou-Mandel

PM Polarisation-Maintaining

EPR Einstein-Podolsky-Rosen

HVT Hidden Variable Theory

CHSH Clauser-Horne-Shimony-Holt

HWP Half-Wave Plate

DHWP Dual-Wavelength Half-Wave Plate

QWP Quarter-Wave Plate

PBS Polarising Beam Splitter

DM Dichroic Mirror

FWHM Full Width Half Maximum

DPBS Dual-wavelength Polarising Beam Splitter

SDE System Detection Efficiency

NANF Nested Antiresonant Nodeless Fibre

SEM Scanning Electron Micrograph

NA Numerical Aperture

MFD Mode Field Diameter

PER Polarisation Extinction Ratio

TDS Time-Domain Spectroscopy

EOS Electro-Optic Sampling

EOM Electro-Optic Modulator

GaAs Gallium Arsenide

BBO Beta Barium Borate

PCA Photoconductive Antenna

SFG Sum-Frequency Generation

TCSPC Time-Correlated Single Photon Counting

SNR Signal-to-Noise Ratio

DR Dynamic Range

SNL Shot-Noise Limit

HL Heisenberg Limit

List of publications

The work conducted in this thesis was published in the following papers:

T. Shields, A. C. Dada, L. Hirsch, S. Yoon, J. M. R. Weaver, D. Faccio, L. Caspani, M. Peccianti and M. Clerici, "Electro-optical sampling of single-cycle THz fields with single-photon detectors", *Sensors*, vol. 22, p. 9432, 8 2022.

S. Prabhakar, T. Shields, A. C. Dada, M. Ebrahim, G. G. Taylor, D. Morozov, K. Erotokritou, S. Miki, M. Yabuno, H. Terai, C. Gawith, M. Kues, L. Caspani, R. H. Hadfield and M. Clerici, "Two-photon quantum interference and entanglement at 2.1 μm", *Science Advances*, vol. 6, pp. 5195-5222, 3 2020.

Acknowledgements

I would like to express my sincere gratitude to my supervisor Matteo Clerici for his continuous support and invaluable insight throughout this project. His patience and encouragement to improve myself both in and out of the lab was fundamental to the completion of this work and for that I will be forever grateful.

I would like to thank all the colleagues I have had the pleasure of working and interacting with in the past 4 years. From day one of this project, I have been surrounded by incredibly encouraging and knowledgeable people which have provided both academic and motivational support throughout. The help and guidance provided by Shashi and Tunmise throughout these measurements was invaluable. I am grateful to my past colleagues such as Sean and Damian who spent many evenings with me in Oakfield Avenue discussing completely unrelated topics to this work. I'd also like to thank the current members of the UNO group: Seungjin, Dionysis, Ivi, Lenny, Lijun and Mehdi for listening to my endless experimental issues over the years. I continue to thank all fellow collaborators working on this and related projects.

Finally, I would like to thank Iona, my close friends and family who have shared the highs and lows of this journey first hand. Without their motivating spirit and helpful support at any time of the day or night, I would never have completed this marathon.

Chapter 1

Introduction

This thesis contains a collection of research focussing on infrared quantum optics. Many quantum optics measurements utilise a non-linear optical process called spontaneous parametric down-conversion (SPDC) which generates pairs of photons with peculiar properties. This process has been implemented in countless demonstrations of optical quantum measurements and has been widely adopted as a reliable source of correlated entangled photon pairs.

The theoretical framework for the SPDC process is presented in Chapter 2 with both classical and quantum descriptions. The efficiency of this three-wave mixing process fundamentally relies on the phase matching conditions associated with the interaction. Several techniques employed to achieve phase matching in non-linear media are presented and the quasi-phase matched (QPM) configuration utilised throughout this work is demonstrated. Different types of SPDC emission are categorised based on the properties of

the non-linear medium and the phase matching conditions and the interesting properties of the resulting non-classical states are detailed.

In the first experimental section of this work, the generation, manipulation and detection of entangled photon pairs at 2.1 μm is presented in Chapter 3. Quantum-enhanced optical systems require robust quantum sources of entangled photon pairs and in recent times, the 2- to 2.5-μm spectral range has been proposed to revolutionise applications in quantum communications, sensing and metrology. The motivations behind an efficient free-space quantum source at 2.1 μm are discussed before the correlated properties of the generated photon pairs are characterised using coincidence detection. The indistinguishability of the down-converted photons is demonstrated by performing high visibility two-photon interference. The realisation and detection of a polarisation-entangled state using a Type-2 SPDC configuration at 2 μm is also performed opening the pathway to technological QKD applications in this spectral regime.

The work in the mid-infrared is continued in Chapter 4 where the feasibility of using hollow core fibre technology to propagate quantum states of light is addressed. Characterisation of a 1 km long Nested Antiresonant Nodeless Fibre (NANF) was performed using a CW fibre laser to assess attenuation and coupling losses at 2 μm. NANF fibres are of interest as propagation takes place in an air core reducing non-linearities and providing low loss in comparison to conventional single-mode fibres. Measurement of the polarisation purity demonstrates that NANF fibre technology preserves the polarisation

of the state and could be used for propagation of quantum states.

In Chapter 5, the thesis moves in a direction of the application of non-classical states for the detection of terahertz (THz) radiation. Based on electro-optic sampling (EOS), THz time-domain spectroscopy (THz-TDS) is an established detection technique which takes advantage of the Pockels effect in non-linear crystals measuring a phase proportional to the THz field strength. The sensitivity of this type of detection is fundamentally limited by the shot-noise of the optical probe used to sample the THz field. The theory for this electro-optic interaction is detailed before characterisation of THz radiation generated using a photoconductive antenna (PCA) is performed. The question that was proposed: can quantum properties of non-classical states be used to enhance THz detection? This work moved towards an answer by devising a lock-in style polarimetric technique using single-photon detectors to measure a phase shift induced on a squeezed vacuum probe. The novel balanced detection scheme was calibrated using an electro-optic modulator (EOM) to simulate a THz-induced phase rotation. Using a characterised THz source, THz electro-optic sampling was successfully performed using phase-locked single-photon detectors at the shot-noise limit. Work was conducted to better understand the metrological potential of using NOON states to enhance THz detection by characterising a NOON state generated using a Sagnac interferometer.

Chapter 2

Spontaneous parametric down-convesion

2.1 Introduction

Spontaneous Parametric Down-Conversion (SPDC), also defined as parametric fluorescence, is a 2^{nd} order non-linear optical phenomenon that lies at the heart of many quantum optics applications. The process can be understood as the splitting of a pump photon into a pair of correlated photons with half the excitation energy after interaction with a non-linear medium [1, 2]. It is worth mentioning for later theoretical considerations that SPDC is associated with the time reversed phenomenon called Second Harmonic Generation (SHG) where two input photons interact to produce a single output photon with double the frequency of the incident state. The "spontaneous" nature

of SPDC emission is typically understood to require quantum vacuum fluctuations to stimulate the process and tends to suffer from poor efficiency when compared to SHG due to the weak nature of non-linear quantum optical processes [1, 3]. The conceptual idea of SPDC was first proposed in the early 1960's and it wasn't long until numerous experimental demonstrations of the process were performed at the turn of the decade [4, 5]. The experimental verification of the quantum correlation properties of the generated photon pairs was performed in 1970 [6] and ever since, the process has been utilised for numerous applications from the measurement of second order non-linear susceptibilities of important non-linear optical materials [7] to the calibration of the quantum efficiencies of detection systems [8, 9]. Many experimental quantum optics measurements utilise the crucial capability of SPDC to generate non-classical states of light with numerous degrees of freedom, as well as heralded single photons [10, 11]. The use of correlated single photons from down-conversion events has enabled breakthroughs in photonic quantum applications such as quantum computational algorithms [12, 13], quantum teleportation [14], integrated circuits [15, 16] and fundamental loophole-free violations of local realism [17, 18].

2.2 Theoretical framework

2.2.1 Classical description of SPDC

In this section, a classical approach to understanding the behaviour of this type of three-wave mixing process will be followed by examining the description of the propagation of light through a non-linear medium derived from Maxwell's equations. Considering a non-linear dielectric medium in source-free regions of space, Maxwell's equations take the form

$$\nabla \cdot \mathbf{D} = 0\,, \tag{2.1}$$

$$\nabla \cdot \mathbf{B} = 0\,, \tag{2.2}$$

$$\nabla \times \mathbf{E} = -\frac{\partial \mathbf{B}}{\partial t}\,, \tag{2.3}$$

$$\nabla \times \mathbf{H} = \frac{\partial \mathbf{D}}{\partial t}\,, \tag{2.4}$$

where $\mathbf{D}$ is the electric displacement field, $\mathbf{B}$ is the magnetic field flux density, $\mathbf{E}$ is the electric field intensity and $\mathbf{H}$ is the magnetic field intensity if we assume no free charges or electric currents. Following the derivations presented in more substantial detail in [1], the relationship between the displacement field $\mathbf{D}$ and electric field intensity $\mathbf{E}$ in a non-linear material can be defined

$$\mathbf{D} = \varepsilon_0 \mathbf{E} + \mathbf{P}\,, \tag{2.5}$$

where ε_0 is the vacuum permittivity and $\mathbf{P}$ is the induced field polarisation. From the most basic understanding of non-linear interactions, the relationship between the induced polarisation $\mathbf{P}$ of a time-varying field is proportional to a power series containing both the linear and non-linear components of the electric field strength vector $\mathbf{E}$ in the form

$$\mathbf{P} = \mathbf{P_L} + \mathbf{P_{NL}} \equiv \varepsilon_0[\chi^{(1)}\mathbf{E} + \chi^{(2)}\mathbf{EE} + \chi^{(3)}\mathbf{EEE} + \cdots], \tag{2.6}$$

where $\chi^{(n)}$ is the nth-order susceptibility of the medium. SPDC is a second-order non-linear optical process and therefore depends on the second-order non-linearity $\chi^{(2)}$ term [19]. The magnitude of a non-linear process is dependent on the combined effects of both the external electric fields and the higher order susceptibilities (namely $\chi^{(2)}$ and $\chi^{(3)}$). These $\chi^{(n)}$ coefficients exist as tensors of rank (n+1) whose tensorial elements are highly dependent on the atomic structure of the non-linear material. For $\chi^{(2)}$ interactions to take place, the atomic crystalline structure must not exhibit inversion symmetry thoughout its volume i.e. the medium must not be centrosymmetric. In centrosymmetric materials, all tensor elements of the $\chi^{(2)}$ susceptibility equal zero and hence exhibit a negligible non-linear response for even-order optical processes [20]. Higher order processes such as $\chi^{(3)}$ effects don't have the same structural limitations. The non-linear susceptibilities for countless optical materials have been studied [21, 22].

In order to understand the important role field polarisation plays in non-linear processes, some assumptions need to be made on the behaviour of the medium. The wave equation can be derived by taking the curl of the equation (2.3) for Faraday's law and using equation (2.4) to obtain the expression

$$\nabla(\nabla \cdot \mathbf{E}) - \nabla^2 \mathbf{E} + \frac{1}{\varepsilon_0 c^2} \frac{\partial^2 \mathbf{D}}{\partial t^2} = 0\,. \tag{2.7}$$

By assuming an isotropic medium, the first term of this expression tends to zero and the linear form of relation (2.5) can be reduced to $\mathbf{D} = \varepsilon_0 n^2 \mathbf{E}$ where n is the linear index of refraction. The wave equation for an isotropic non-dispersive material can then be represented by

$$\nabla^2 \mathbf{E} - \frac{n^2}{c^2} \frac{\partial^2 \mathbf{E}}{\partial t^2} = \frac{1}{\varepsilon_0 c^2} \frac{\partial^2 \mathbf{P_{NL}}}{\partial t^2}\,, \tag{2.8}$$

detailing the relationship between the non-linear response of the polarisation and the related electric field. This is a simplification of the treatment required for a dispersive medium, where each frequency component of the interacting field must be considered independently [1]. This equation will provide the framework for describing the SPDC three-wave mixing process and produces solutions for each frequency of light involved. Using frequencies for the pump field ω_p and resultant signal ω_s and idler ω_i fields, solutions to the wave equation can be found by adopting fields propagating in the z-direction with

the form of the pump

$$E_p(z,t) = A_p e^{i(k_p z - \omega_p t)} + C\,, \tag{2.9}$$

where the pump electric field $E_p(z,t)$ is described in terms of a plane wave with fixed amplitude A_p, wavenumber component $k_p = \frac{n_p \omega_p}{c}$ and complex conjugate C [2]. Signal and idler fields $E_s(z,t)$ and $E_i(z,t)$ follow the same formalism. Similarly, the definition of the source of the non-linearity can be introduced on the polarisation of the pump field P_p. Substituting the solution $E_p(z,t)$ into equation (2.6), the pump polarisation can take the form

$$P_p(z,t) = 2\,\varepsilon_0\,\chi^{(2)} A_s A_i e^{i(k_s z + k_i z - \omega_p t)} + C\,, \tag{2.10}$$

where $\chi^{(2)}$ is closely related to the effective non-linear susceptibility d_{eff} which is dictated by the type of non-linear crystal being used and will be further discussed in later sections. As before, the signal P_s and idler P_i polarisation relations can be derived. A substitution of respective electric field (2.9) and polarisation terms (2.10) for pump, signal and idler fields into the wave equation defined previously allows coupled-amplitude equations to be estimated for each photon in the system. These coupled-amplitude equations introduce the *phase-matching* conditions (discussed in more detail later in this chapter) with the wavenumber terms rearranged into the form $\Delta k = k_p - k_s - k_i$. The two coupled-amplitude equations for both signal and

idler fields can then be described by

$$\frac{dA_s(z)}{dz} = i\frac{A_p\,\omega_s^2\,\chi^{(2)}}{k_s\,c^2}A_i(z)e^{i\Delta kz}\,, \tag{2.11}$$

$$\frac{dA_i(z)}{dz} = i\frac{A_p\,\omega_i^2\,\chi^{(2)}}{k_i\,c^2}A_s(z)e^{i\Delta kz}\,, \tag{2.12}$$

showing the variation on the field amplitudes as a result of the coupling to the other interacting frequencies as they propagate in the +z direction. At the fundamental phase matched condition $\Delta k = 0$, the Manley-Rowe solutions for both signal and idler fields can be extracted

$$A_s(z) = A_s(0)\cosh(\kappa z)\,, \tag{2.13}$$

$$A_i(z) = i\zeta\frac{A_p}{|A_p|}A_s(0)\sinh(\kappa z)\,, \tag{2.14}$$

where $\zeta = \sqrt{\frac{n_s\omega_i}{n_i\omega_s}}$ and $\kappa = \frac{\chi^{(2)}\zeta}{c}|A_p|$ are introduced coupling constant quantities for some simplification [1]. Violation of the phase matching condition ($\Delta k \neq 0$) results in rotation of the phase of the coupling between output fields as they propagate through the medium in comparison to a constant relative angle when phase matched. The importance of the phase matching condition on the viability of the SPDC process becomes more apparent by dissecting these solutions. For example, increasing the interaction length along propagation (non-linear crystal thickness) corresponds to an improvement in coupling between output photons. From the solutions above, it becomes obvious that the SPDC model breaks down when the assumption $A_s(0) = 0$ is

made. An entirely classical description is clearly insufficient to describe the creation of down-converted fields from a pump field [23]. To tackle the issues highlighted by this classical description, a quantum mechanical description naturally follows and the next section will delve into the "spontaneous" nature of the process and how quantum fluctuations are required to enable the parametric fluorescence phenomenon.

2.2.2 Quantum description of SPDC

The interaction of electromagnetic fields in a classical framework can successfully describe numerous types of optical phenomena including effects which seem non-classical in nature. However, when describing inefficient interactions such as SPDC where very low photon numbers appear, some fields need to be managed with a quantum theoretical framework. Adopting a quantised approach to electromagnetic field interactions is essential in order to model single photon events and a quantum description is required to predict the behaviour and properties of the photon pair events generated in this process. This theoretical exercise begins with the quanitisation of the electromagnetic field beginning with the previously defined Maxwell equations and follows closely the more detailed description presented in [19]. Quantum mechanically, the three-wave mixing process can be described using the interaction Hamiltonian in the form

$$\hat{H} = \sum_{j=1}^{3} \hbar\omega_j \left(\hat{a}_j \hat{a}_j^\dagger + \frac{1}{2}\right) + \hbar\kappa_c [\hat{a}_s^\dagger \hat{a}_i^\dagger \hat{a}_p] + H.C.\,, \tag{2.15}$$

where $\hbar\omega_j$ is the energy of a single photon in mode j, κ_c is a coupling constant reliant on non-linear susceptibility $\chi^{(2)}$ of the interaction and we introduce the quantum operators $\hat{a}^\dagger$ and $\hat{a}$. For simplicity of the argument, the Hermitian conjugate term (H.C.) denoting the inverse process contributing to SHG is ignored. Explicitly, the photon creation operator $\hat{a}^\dagger$ helps account

for appearance of photons and the photon annihilation operators $\hat{a}$ denotes the removal of photons from the interaction. The coupling term $\hat{a}_s^\dagger \hat{a}_i^\dagger \hat{a}_p$ denotes the targeted three-wave mixing process where a pump photon $\hbar\omega_p$ is destroyed and a pair of signal and idler photons created with energy $\hbar\omega_s$ and $\hbar\omega_i$ respectively. It can be useful to compare the quantisation of electromagnetic fields to the expressions of the quantum harmonic oscillator where equivalent quantum operators are used to transition between energy levels. For a state $|j\rangle$ where j denotes the number of photons, the quantum operators behave according to the following

$$\hat{a}^\dagger |j\rangle = \sqrt{j+1}\,|j+1\rangle \ , \tag{2.16}$$

$$\hat{a}\,|j\rangle = \sqrt{j}\,|j-1\rangle \ , \tag{2.17}$$

where they closely resemble ladder operators in the quantum harmonic oscillator framework. From the interaction Hamiltonian defined, the photon number operator $\hat{N}_j = \hat{a}_j \hat{a}_j^\dagger$ can be defined and the commutation of these operators is important to ensure the conservation of observables of the evolving system.

Considering a time-dependent state defined as $|\Psi(t)\rangle$ in the Schrödinger picture, the quantum evolution is of the form

$$|\Psi(t)\rangle = e^{-\frac{1}{i\hbar}\int_0^t \hat{H}\,dt}\,|\Psi(0)\rangle\ , \tag{2.18}$$

where $|\Psi(0)\rangle$ is the initial state at time t=0 and the unitary operation is performed on the previously described Hamiltonian term $\hat{H}$ for the duration of the interaction up to time t [24]. The intial state for the SPDC process consists of only pump photons with photon number N_p and the interaction time limits are related to the propagation time across the length of the non-linear crystal L. Expansion of the Hamiltonian term using a perturbative approach up to the first order leads to a state approximated by

$$|\Psi(t \Rightarrow L)\rangle = C\,|N_p, 0_s, 0_i\rangle + C_{dc}\,|N_p - 1, 1_s, 1_i\rangle\ , \tag{2.19}$$

where the coefficient associated with down-conversion C_{dc} is related to the coupling constant κ_c, propagation time through the medium and the pump photon number N_p. The significance of the weighting between these coefficients is apparent as the down-conversion coefficient is substantially smaller than the first coeffcient term C from the expansion. Typically, $C_{dc} << 1$ and the consequence of this approximation results in almost all of the input pump state propagating through the medium without interaction as detailed in the first term of this equation. This details the inherent inefficiency in the SPDC process and shows that the probability of generating photon pairs is typically

very small. As will be discussed later in this chapter, the efficiency of the three-wave mixing process is heavily reliant on the coupling term κ_c which depends on the susceptibility of the medium $\chi^{(2)}$ and the phase-matching conditions.

2.3 Phase matching

This spontaneous three-wave mixing process typically relies on the conversion of an incident pump photon into two signal and idler photons with half the energy of the excitation field. In combination with complete transfer of pump momentum p_p to signal and idler momenta (p_s, p_i), these conditions are defined as the *phase-matching conditions*. Figure 2.1 shows the fundamental energy $E = \hbar\omega$ and momentum $\mathbf{p} = \hbar\mathbf{k}$ conservation laws given by

$$\hbar\omega_p = \hbar\omega_s + \hbar\omega_i \,, \tag{2.20}$$

$$\hbar\mathbf{k_p} = \hbar\mathbf{k_s} + \hbar\mathbf{k_i} \,, \tag{2.21}$$

where ω and $\mathbf{k}$ are the frequency and wavenumber associated with each respective photon [6, 25]. In order for non-linear processes such as three-wave mixing to generate down-converted photons efficiently, the relative phase relationship between interacting photons needs to be conserved. When a phase mismatch occurs and the phase matching condition is not satisfied, the output photons will sinusoidally move in and out of phase with the other throughout the length of the non-linear crystal drastically affecting the conversion efficiency of the process. The obvious issue that occurs during such a non-linear process is the subsequent change in phase velocities between interacting photons of different frequencies in the active medium due to its inherent refractive properties.

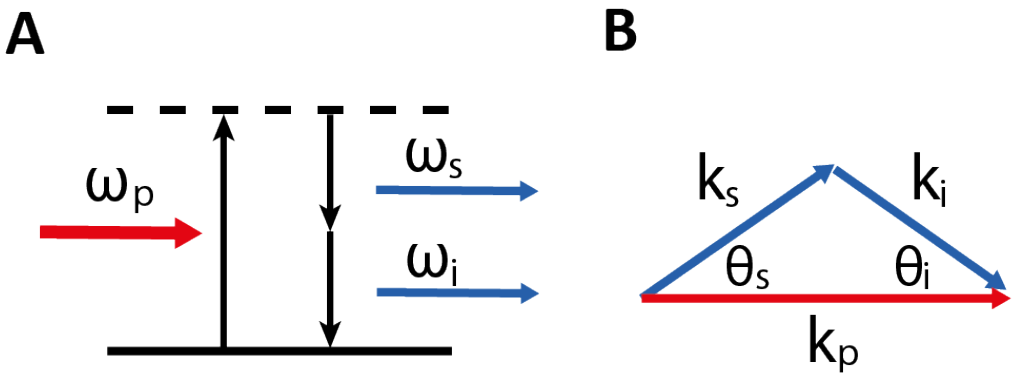

Figure 2.1: The phase matching conditions for SPDC (A) The energy diagram for the annhilation of the pump photon of frequency ω_p into two daughter signal and idler photons with frequencies ω_s and ω_i (B) The conservation of momentum considerations and respective output angle of signal θ_s and idler θ_i photons.

There are numerous approaches that can be implemented in order to ensure the efficient conversion effect occurs throughout the full interaction of the medium. One such method utilises the birefringent property of the nonlinear material which is defined as the dependence of the refractive properties of a medium on the polarisation orientation of the interacting radiation [1]. Specific choice of the orientation of the crystalline material and tuning the relative angle between the medium and the incident field is known as *critical phase matching*. This technique relies on the dependence on the refractive properties on the angular alignment of the system and typically vulnerable to walk-off between interacting fields. Naturally, the efficiency of the nonlinear processes suffers as a result of this. However this problem can be mitigated by considering a *non-critical phase matching* technique. By fixing

the relative angle of the crystal perpendicular to the propagation direction, phase matching can be obtained by utilising the temperature dependence of the refractive properties of some crystals. However, the narrow ranges of temperatures which achieve phase matching can typically be far from ambient room temperature and, therefore, crystal ovens are often required to accurately monitor temperatures and minimise fluctuations. An alternative method of ensuring the efficient energy transfer between the interacting fields is by spatially modulating the non-linear medium in a technique called *quasi-phase matching*. A popular implementation of this method involves engineering the non-linear crystal structure to help compensate for the phase mismatch. By periodically inverting the crystal domains along the propagation axis, the non-linearity susceptibility coefficient d_{eff} then cyclically changes sign ensuring the build up of the output field throughout the length of the medium [23].

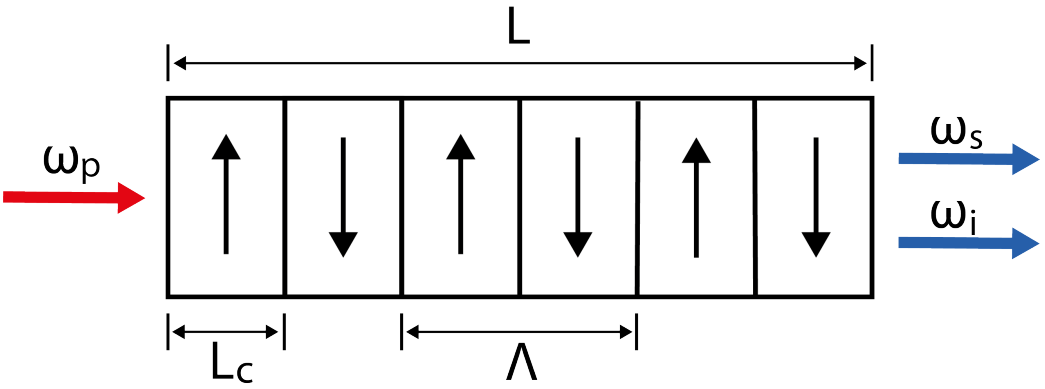

Figure 2.2: Schematic depicting the periodically-poled crystal structure of period Λ over the full crystal length L used to achieve quasi-phase matching. Inversion of the poling structure (black arrows) occurs after each iteration of the coherence length L_c and has the effect of inverting the sign of the non-linearity susceptibility coefficient d_{eff}. This periodic alternation helps ensure efficient field accumulation of ω_s and ω_i frequencies throughout the crystal structure.

The mathematical representation of this spatially modulated non-linear coefficient over the propagation direction z through the crystal length L can be defined by the Fourier series

$$d(z) = d_{eff} \sum_{n=-\infty}^{\infty} \frac{2}{\mathrm{n}\pi} \sin\left(\frac{\mathrm{n}\pi}{2}\right) \exp(ik_n z)\,, \tag{2.22}$$

where $k_n = 2\pi n/\Lambda$ is defined as the grating vector for the n-th Fourier component of the series [1]. When a crystal is "periodically-poled", as shown in Figure 2.2, the modulation period Λ is typically engineered to be twice the frequency of the coherent length L_c of the interaction in order to reverse the sign of d_{eff} at periodic regions where phase mismatching should occur [26].

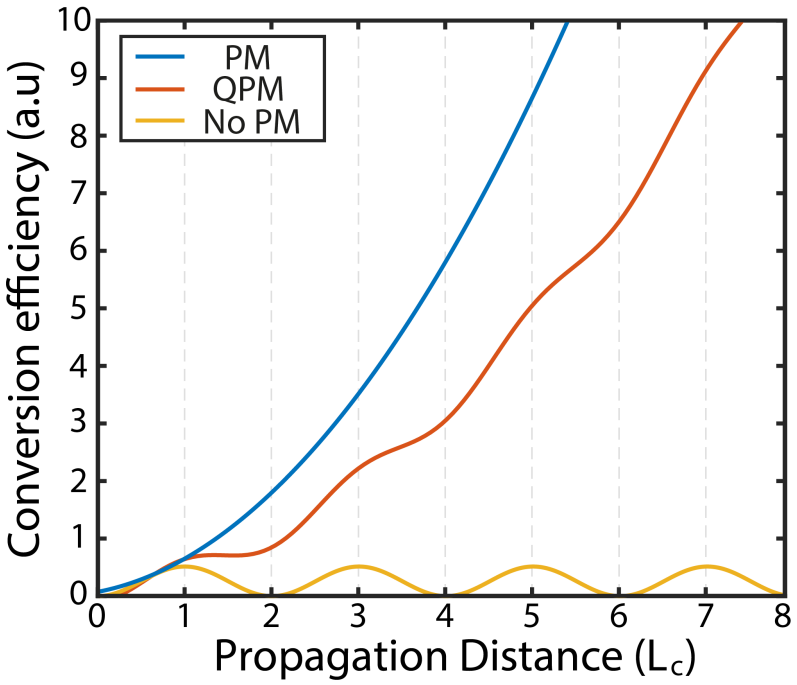

Figure 2.3: Schematic demonstrating the trend of conversion efficiency for a typical three-wave mixing process for phase matched (PM), quasi-phase matched (QPM) and no phase matching (No PM) conditions against the propagation distance measured in units of the coherence length (L_c).

A schematic showing the periodicity of this effect is shown in Figure 2.3. For the non-phase matched case, the conversion efficiency oscillates with propagation distance with peaks every odd iteration of the coherence length L_c. In the quasi-phase matched (QPM) case, for one L_c period of propagation distance, the QPM configuration tracks the non-PM case until the periodic poling flip occurs resulting in a step-by-step growth in conversion efficiency

as the propagation distance increases. The result of this modulation of the d_{eff} produces a total non-linear coefficient d_{QPM} defined by

$$d_{QPM} = \frac{2}{n\pi} d_{eff} \,, \tag{2.23}$$

where n is the "order" of QPM where typically $n = 1$ is the optimum condition [1, 26]. This factor $\frac{2}{n\pi}$ effectively restrains the overall non-linear coefficient to below the phase matched condition but shows that efficient interactions can take place even if the phase mismatch still takes place. This ultimately results in QPM providing a high conversion efficiency without relying on birefringent properties of the medium meaning different choices of field polarisations can be used effectively. Due to the lack of walk-off, the thickness or length of the non-linear crystal can be longer which helps increase the efficiency of the generation [23]. Some materials such as lithium niobate ($LiNbO_3$) cannot apply birefringent phase matching methods however can be spatially modulated with ferroelectric domains periodically inverted to ensure coherence between pump field and generated photon pair pulse via QPM. For the measurements performed throughout this thesis, periodically-poled lithium niobate (PPLN) was specifically chosen for the properties defined and temperature tuned to produce high-quality SPDC generation.

2.4 SPDC generation configuration

The photon pairs generated are intrinsically correlated in energy and momentum but in order to prepare a Bell state (specific maximally entangled two-photon states) [27], further local operations are required which will be dissected later in this chapter. The type of SPDC radiation emitted is highly dependent on the properties of the non-linear crystal and the phase matching conditions but can generally be split into three categories defined by the polarisation of the photons involved. In a Type-0 configuration, birefringent phase matching is not utilised here and the polarisation of the output photon pair stays unchanged in comparison to the input photon polarisation. In a Type-1 configuration, the input photon polarisation is orthogonal to the parallel orientated polarisations of both the signal and idler photons. Figure 2.4 shows the typical SPDC emission profile in these configurations. The emitted photon pair from both Type-0 and Type-1 configurations typically exit the non-linear material at the same angle $\theta = \cos^{-1} \frac{\mathbf{k_p} \cdot \mathbf{k_{s,i}}}{k_p \cdot k_{s,i}}$ in reference to the crystal axis but on opposing symmetrical sides of a cone centred on the pump field [28, 29]. In the degeneracy and collinear condition, the two photons emitted from these processes are indistinguishable from each other which is crucial for quantum measurements discussed in later work.

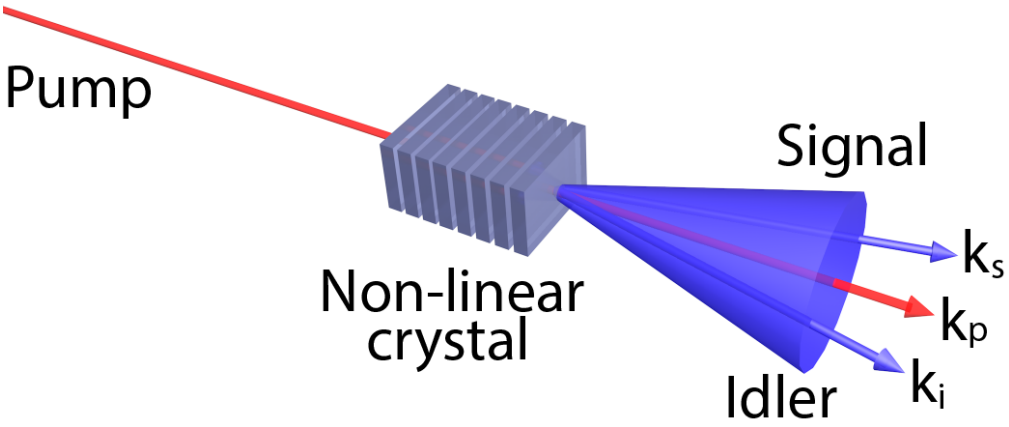

Figure 2.4: Schematic of SPDC in a Type-0 or Type-1 configuration depicting pump field (red) incident on a non-linear crystal generating signal and idler photons with momenta k_s and k_i constrained to symmetrical edges of a cone (blue) centred on the pump field k_p.

In Type-2 configuration, the signal and idler photons are orthogonally polarised to each other and subsequently, produce emission cones (similar to the previous process) however in the non-collinear condition, these can overlap at specific points producing photons in a superposition of polarisation states [1]. The resulting non-classical state of this system (shown in Figure 2.5) is given by

$$|\Psi^+\rangle = \frac{1}{\sqrt{2}}\Big(|HV\rangle + e^{i\phi} |VH\rangle \Big), \tag{2.24}$$

where ϕ denotes the relative phase difference between the two output amplitudes sensitive to the crystal position and optical path alignment [30, 31].

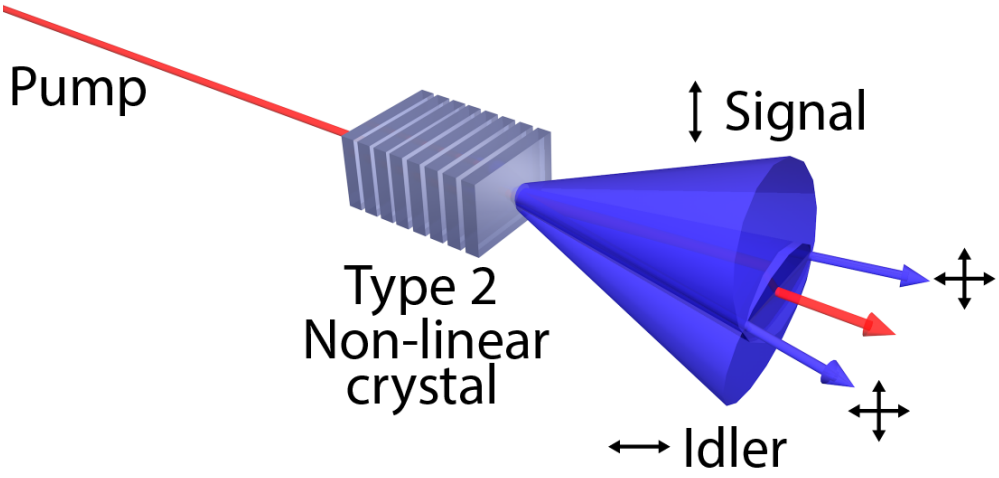

Figure 2.5: Schematic detailing the non-collinear Type-2 generation of photon pairs correlated in the polarisation degree of freedom. The light identifiable at horizontal and vertical cone intersection points is a non-classical polarisation entangled state crucial for many quantum optics applications.

Accounting for spatial and temporal discrepancies can produce polarisation indistinguishable states such as Bell states which are maximally entangled polarisation states (see Chapter 3). This experimental method can also produce NOON states which are states composed of a superposition of N photons in one mode and zero photons in another. An interesting property of NOON states is that phase sensitivity can approach the Heisenberg limit, a fundamental boundary for measurement precision which enhances measurement sensitivity by a factor of $\sqrt{N}$ in comparison to classical limits [32]. The enhancement in phase detection will be investigated in further chapters.

The non-linear SPDC process can be described by the following Hamiltonian,

$$\hat{H} \approx \varepsilon_0 \int d\omega_s d\omega_i \psi(\omega_s, \omega_i) \xi(\omega_s, \omega_i) a^\dagger(\omega_s) a^\dagger(\omega_i) + H.C., \tag{2.25}$$

where ε_0 is the dielectric permittivity of the vacuum, $a^\dagger$ are the creation operators for the signal and idler photons and H.C. means Hermitian conjugate. The phase matching function $\xi(\omega_s, \omega_i)$ typically takes the form of a sinc function depending on crystal length L and phase mismatch Δk [2]. Energy conservation is fixed by the enveloped pump pulse function $\psi(\omega_s, \omega_i)$ which takes the form of the pulse shape. If we assume the pump pulse is Gaussian, the enveloped function can be given by,

$$\psi(\omega_s, \omega_i) = \exp\left[- \frac{(\omega_i + \omega_s - \omega_p)^2}{\Delta\omega_p^2} \right], \tag{2.26}$$

where $\Delta\omega_p^2$ is the frequency bandwidth of the pump [33]. The pump beam is down converted into beams of photon pairs with paths constrained to a cone centred on the pump with radius, r, which is proportional to the width of the down converted ring [34]. Emission depends closely on the phase-matching conditions and the pump shape. In most cases, the output field in the near-field and far-field are highly incoherent [35]. In the instance of this work, the non-linear PPLN crystal used is spatially modulated with ferroelectric domains periodically inverted to ensure coherence between pump field

and generated photon pair pulse via quasi-phase matching. Throughout the work conducted here, PPLN crystals (from Covesion Ltd.) of varying configurations and specifications are used to generate photon pairs at degeneracy wavelengths at telecom and mid-infrared wavelengths.

Chapter 3

Generation and detection of entangled photon pairs in the mid-infrared

3.1 Motivation behind 2 μm

The ability to generate and detect quantum states of light is crucial in numerous field applications in science, medicine and beyond. Quantum technology is a fast growing field of physics and engineering which utilises fundamental properties of these states from quantum mechanics such as quantum entanglement and quantum superposition and implements them in real world applications such as quantum communication, quantum cryptography and quantum sensing. Based on their requirements, a wide range of quantum sources at

varying wavelengths are required depending on the propagation medium, detector efficiencies and system interactions being investigated. Quantum-enhanced optical systems are available for visible, near-infrared (NIR) and telecom wavelengths but are absent for the 2- to 2.5-μm mid-infrared spectral region. This section details the motivation behind the generation, manipulation and detection of entangled photons in the mid-infrared and why they have the growing potential to revolutionise emerging applications in communications, sensing, and metrology.

Generation and detection of the quantum states is fundamental to the unconditional security of both guided wave and free-space communication systems [36,37]. A new horizon of secure communications was realised when the computational vulnerabilities of traditional public key cryptosystems led to the birth of quantum key distribution (QKD) [38]. By harnessing the intrinsic quantum properties of single photons, unconditional security between parties can be ensured using the fundamental laws of quantum physics. The security gained by sharing encoded photonic information between parties is secured by the quantum no-cloning theorem which states that it is impossible for a supposed eavesdropper to create a copy of an unknown quantum state [39]. However, the practical realisation of QKD on a global scale across thousands of km of optical fibre or free space is fundamentally limited by photon loss in the communication channel [40, 41]. Nevertheless, high-fidelity long-distance distribution of quantum entanglement has been successfully demonstrated in free-space conditions even when subject to significant attenuation from atmo-

spheric conditions [42]. In recent groundbreaking work, free-space QKD has enabled quantum-secured intercontinental communication between locations 7600 km apart on Earth exploiting spaced based links where channel loss is more negligible [43]. To reduce the effect of the solar background radiation, satellite-based QKD has only been possible at night. However, recent studies have proposed operating optical links near telecommunication wavelengths to help alleviate this issue and enable daylight quantum communications [44]. A possible solution to this comes from the use of infrared radiation for free-space communications where there is considerable lower Rayleigh scattering from subwavelength-sized particles. At 2.090 μm, the target of my studies, the atmosphere is nearly as transparent as at 1.5 μm but outwith the atmosphere grants a threefold reduction in solar irradiance per unit area for a 50 nm bandwidth [45]. The potential benefits of a robust quantum source operating at 2 μm for free space ground-to-satellite and satellite-to-satellite based quantum communications makes a strong case for investigating both sources and detection of non-classical light fields at the mid-infrared and beyond [46].

Development of quantum sources in the 2 μm spectral region is also of particular interest in numerous sensing fields such as medicine, LIDAR and atmospheric sensing [47–50]. In the high-sensitivity metrological regime, the Laser Interferometer Gravitational-Wave Observatory (LIGO) has proposed to extend the reach of future gravitational wave detection beyond our galaxy by setting an operational wavelength at 2 μm [51]. The proposed plans for

LIGO-Voyager class detectors are to achieve quantum noise rejection through the injection of 10 dB squeezed light at 2 μm in a step towards a 2 μm "squeezer" crucial for sensitivity targets. The set wavelength upgrades benefit from a reduction in optical scattering loss from crystalline silicon (which scales with $1/\lambda^2$) used as cryogenically cooled test masses but also from a lower absorption in optical coatings with amorphous silicon in comparison to 1.5 μm wavelengths [52].

A further reason to explore the 2 μm window comes from the areas of guided wave optics and integrated photonics. The drastic increase in network capacity since the beginning of the digital age is approaching a theoretical limit where conventional technology upgrades are required to avoid a "capacity crunch" and cope with modern bandwidth demands [53, 54]. A promising solution is the implementation of novel hollow-core photonic bandgap fibers (HC-PBGF) operating a 2 μm where propagation takes place in an air core reducing nonlinearities and providing low loss in comparison to conventional single-mode fibres [54–57]. Being a potential candidate for exceptional low latency, high capacity transmission, HC-PBGF's are currently being tested as candidates for full network implementation and could revolutionise future telecommunications [58, 59]. Additionally, integrated silicon photonics have an interest into expanding to the 2 μm range. At 2.1 μm, photon pairs are unable to excite electrons inside the crystal and the limiting effect of two-photon absorption (TPA) subsides as shown in Figure 3.1 [60]. Longer wavelengths also benefit from lower linear and non-linear losses expected

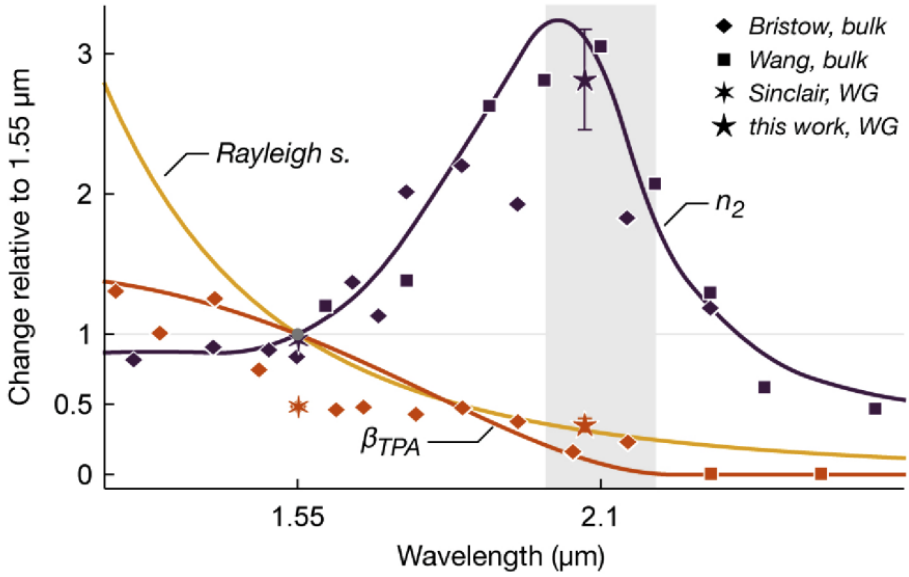

Figure 3.1: Performance of silicon photonics at 2.1 μm. The effects of two-photon absorption (TPA) and Rayleigh scattering are reduced at the target wavelength [59]. Figure reproduced from "Mid-infrared quantum optics in silicon.", Opt. Express 28, 37092-37102 (2020).

from silicon based interations with examples of Si-Ge waveguides capable of providing 10 GB/s communication speeds over a few centrimetres being recently reported [61].

As previously discussed, both the integrated and free-space communication infrastructure face significant challenges operating at these wavelengths due to less developed advancements in detector and optical technologies in comparison to telecom or visible wavelengths. Future infrastructure in both guided wave and free space communications at 2 μm will inevitably require a level of security which provides a clear motivation to develop quantum sources capable of secure QKD at longer wavelengths [60, 62]. The bulk of

my work presented here focuses on the demonstration of two-photon interference and polarisation entanglement using a robust source of photon pairs at 2.090 μm. The generation, manipulation and detection of a correlated photon pair source operating in the mid-infrared provided the foundation to further studies on device independent quantum key distribution (DIQKD) reported in [63], representing a substantial step forward for quantum technologies in 2 μm waveband.

3.2 Characterisation of SPDC efficiency at 2.1 μm

The first measurement performed was designed to characterise and optimise the degenerate photon pair generation via SPDC in a Type-0 phase-matched configuration. In this measurement, a pump photon driven by an ultrashort pulsed laser is converted via vacuum noise amplification into a pair of correlated photons with half the energy of the excitation field. This non-linear process is driven by a Ytterbium-based ultrashort pulsed laser (Chromacity Ltd.) with a central wavelength of 1.045 μm, pulse duration of 130 fs and a repetition rate of 80 MHz. The output polarisation of the laser was linear and the average power generated at the carrier wavelength was up to 3.1 W. In order to control the power output from the pump laser, a manual variable attenuator (EKSMA Optics) consisting of a zero order half wave plate and two thin film brewster type polarisers was used. Polarisation contrast is obtained by operating the two thin film polarisers at 70° angle of incidence to transmit p-polarised light while reflecting s-polarised light. This aids control of the polarisation of the excitation field which is focused in a non-linear crystal in Type-0 configuration in a process where the polarisation of the excitation field and the generated daughter photons are the same. To this end, we used a 1-mm-long periodically poled, magnesium-doped lithium niobate crystal (MgO-PPLN; Covesion Ltd.). The crystal length was chosen

to guarantee maximum conversion efficiency and minimal temporal separation between the pump pulse and the generated SPDC field. The crystal has been poled with the ferroelectric domains periodically inverted to assure coherence between the pump field and the generated photon-pair phase via quasi-phase matching for the whole length of the crystal and over a broad bandwidth [1]. Characterisation of the MgO-PPLN crystal and the dependence of SPDC generation efficiency on crystal temperature was performed by measuring the down-conversion field generated from the crystal using an InGaAs amplified photodetector (Thorlabs PDA10DT-EC). To optimise the signal-to-noise ratio as the down-conversion efficiency is low, phase locked detection was performed by using an optical chopper at a frequency of 1383 Hz as a reference for a lock-in amplifier (Stanford Research, SR830) to detect the generated signal. A 50 nm bandpass filter was used to select the portion of the down-converted field in the degenerate 2.090 μm spectral region. Additional filters, such as long-pass ($\approx 1.85\,\mu$m edge) anti-reflection coated germanium windows, were used to reject the intense laser excitation field. Adding the 50 nm bandpass filter reduced the number of temporal modes to 1.8 ± 0.1 which is the condition at which these measurements were conducted. Characterisation of the crystal on the basis of crystal temperature was performed by pumping the crystal using the full laser power of 965 mW which was measured after the optical chopper. Different poling periods were tested to determine the optimal condition and throughout these series of experiments reported here, a poling period of 30.8 μm (Grating 1 in Figure 3.2)

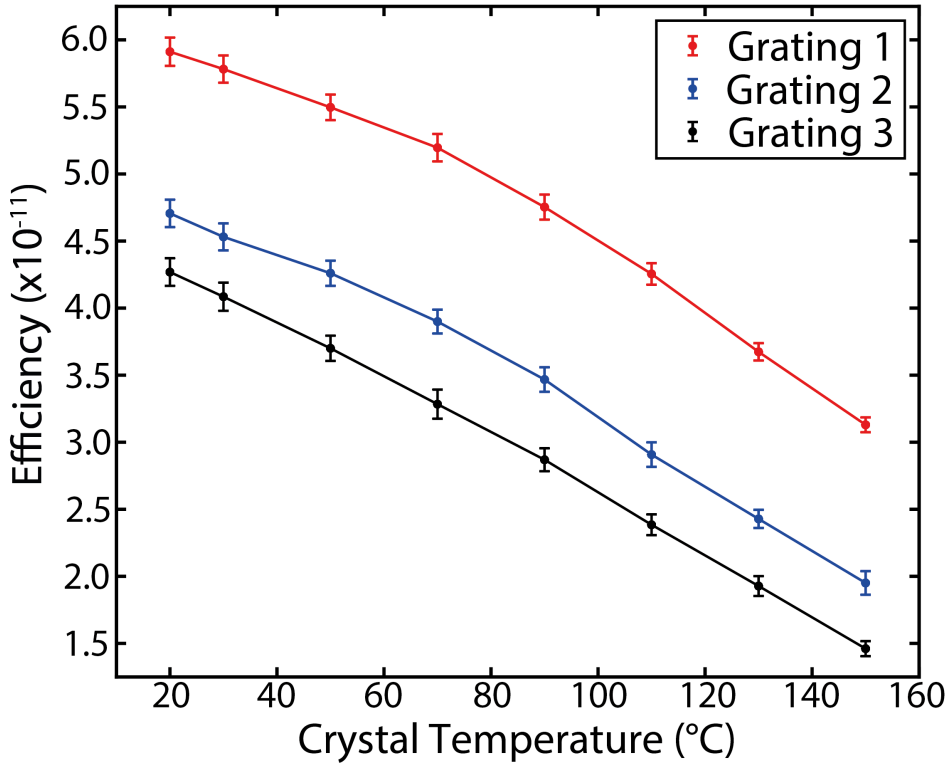

Figure 3.2: The characterisation of the SPDC generation efficiency for three of the nine periodically poled crystal gratings (1, 2 & 3) to optimise collinear generation of degenerate photon pairs at 2.090 μm. The red, blue and black curves are simply to guide the eye.

was used with a stable temperature of (30 ± 0.1)°C controlled by a crystal oven. With the correct poling period and crystal temperature optimised for degenerate photon pair generation at the target wavelength, the efficiency of the generation was characterised by calibrating the lock-in detector and accounting for losses from optical components namely filters.

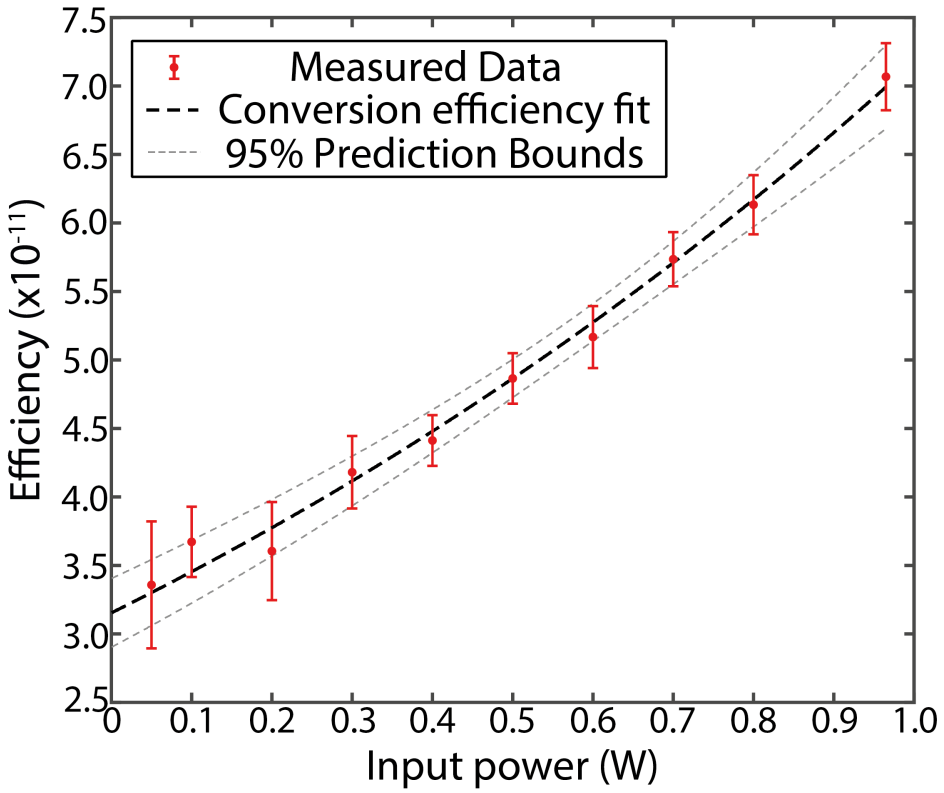

Figure 3.3: Characterisation of the spontaneous down-conversion efficiency in a 50-nm bandwidth centered at the 2090 nm degenerate emission wavelength. The black dashed line is a fit of the conversion efficiency based on the simple model mentioned in the main text. The light gray dashed curves indicate the 95% prediction bounds.

As shown in Figure 3.3, the conversion efficiency increases non-linearly with increasing excitation power. The fit to the data follows the standard equation expressing the down-converted power,

$$P_{SPDC} = \alpha sinh^2(\gamma\sqrt{P_{pump}}), \tag{3.1}$$

where α is the loss coefficient, P_{pump} and γ is the product of the generation crystal length and the non-linear coefficient. The efficiency can be extracted using the ratio of the SPDC and pump powers,

$$\eta = \frac{P_{SPDC}}{P_{pump}}. \tag{3.2}$$

For an excitation power of 10 mW, we extract an SPDC efficiency η of $3.0 \pm 0.2 \times 10^{-11}$ in the targeted photon starved regime with a photon pair generation rate of $\approx 0.04 << 1$ per laser pulse. From Figure 3.3, the conversion efficiency increases non linearly with increasing pump power however in the low power regime the efficiency behaviour can be described by

$$\eta = \alpha\gamma^2 + \frac{1}{3}\alpha\gamma^4 P_{pump}. \tag{3.3}$$

At low power, the expected SPDC efficiency is constant as the first term dominates. It is essential to operate in the photon starved generation regime to avoid saturating the single-photon detectors used to measure the SPDC field and to also avoid generating multiple photon pairs per pulse which is problematic for quantum-secured communication protocols. Figure 3.4 shows the measured number of photons per pulse generated for varying input power. At high power, we observe the generation of a bright squeezed vacuum state with ≥ 16 photons per pulse indicating a pump power < 50 mW is required to operate in the photon-starved regime critical for our further measurements.

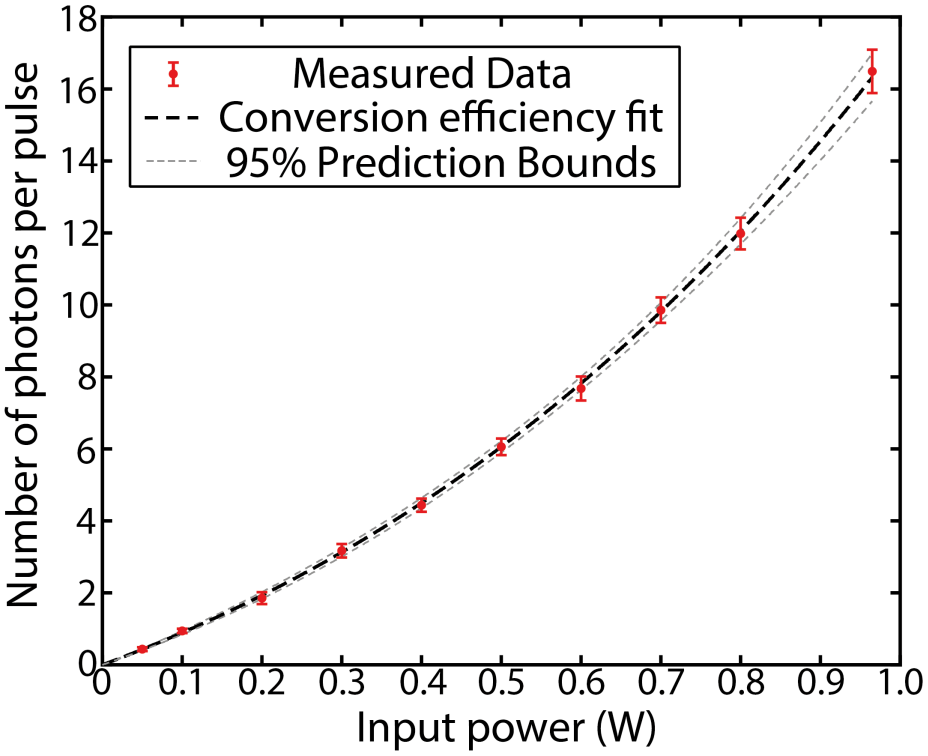

Figure 3.4: Measured number of photons generated for input powers up to 1 W. The black dashed line is based on the fit described in Figure 3.3.

3.3 Coincidence detection of correlated photon pairs at 2.1 μm

3.3.1 Coincidence-to-accidental ratio of correlated photon pair source at 2.1 μm

An important demonstration required when characterising the non-classical properties of generated SPDC radiation is to show the correlation between the signal and idler photons of the SPDC field. As the photon pairs are generated together in the non-linear crystal, coincidence detection can be performed by separating the pair upon propagation in the far-field. The signal and idler photons emerge at opposite angles from the nonlinear crystal around the excitation-field propagation direction as a result of conserving transverse momentum as can be observed in Figure 2.4. The experimental setup shown in Figure 3.5 indicates the process of spatial separation and coincidence detection of the generated photon pairs. The excitation field is focused into the non-linear crystal using a lens with 50 mm focal length lens chosen specifically to help maximise coupling of the down-converted field into the single-mode fibres used in detection [64]. The pump beam characteristics were confined to ensure the Rayleigh length was close to half the crystal length which in our case was 1 mm long.

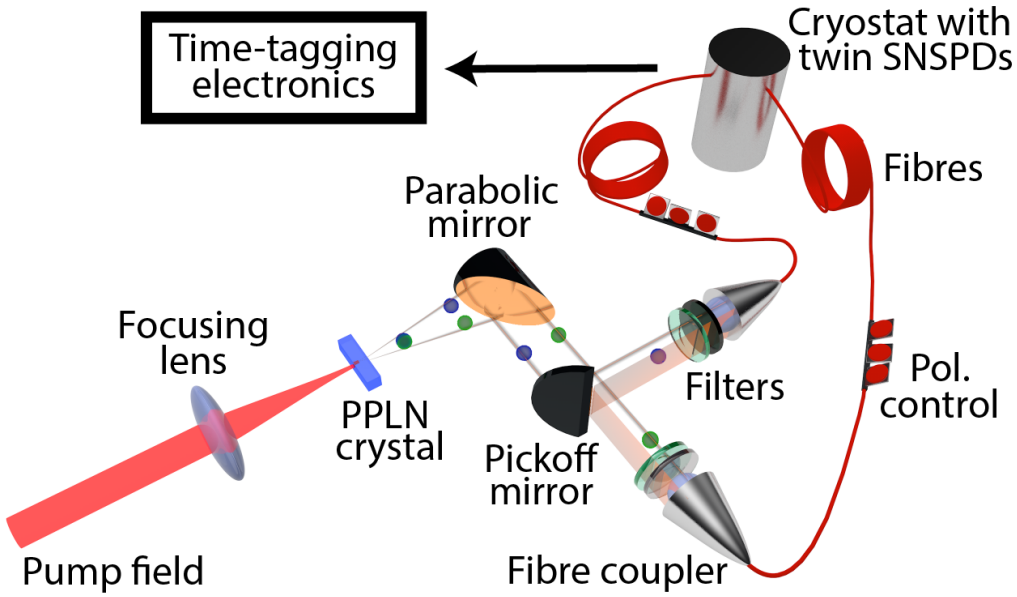

Figure 3.5: Experimental setup for coincidence detection of degenerate photon pairs at 2.090 µm with SNSPD's.

Using the characterisation data previously obtained, the optimal condition for maximised Type-0 SPDC generation was using a poling period of 30.8 μm at a crystal temperature of $30 \pm 0.1°C$. The generated SPDC field was collimated using a short focal length parabolic mirror before being spatially separated in the far-field using a pickoff (D-shaped) mirror. Separated signal and idler photons were filtered in bandwidth with 50 nm bandpass filters before being coupled into a pair of 15 m long single-mode fibres (SM2000) with polarisation control which were routed into a cryostat containing superconducting nanowire single-photon detectors (SNSPDs). The alignment of the optical setup was performed using the parasitic 520 nm signal i.e. the

second harmonic of the 1040 nm pump. The SHG and pump fields were suppressed by inserting a Germanium filter in line (with a band gap of 0.66 eV) which rejects excitations below ≈ 1.8 μm [65]. Single-photon detection was performed using the SNSPD's with time-tagging electronics (PicoQuant Hydraharp) to record the arrival time of each photon and populate a coincidence histogram. Single-photon detectors utilise trigger detection in order to collect all correlated photons within a specific time interval. Photon counting devices are characterised by their quantum efficiency ν, which can be described trivially as the ratio of the detected photo-counts to the number of incident photons. Accidental events occur as a result of a number of background uncorrelated photons from dark counts and even from photons from earlier or later down conversion events and they were not subtracted from the data set. The HydraHarp software can produce time-tagged time-resolved (TTTR) data in order to detect correlated photon events with high temporal resolution. The HydraHarp software offers two alternative time-tagging modes, T2 and T3 modes. T2 mode simply records each input independently and contains arrival time information in reference to when the measurement began. T3 mode is designed for periodic signals received from pulsed lasers where the repetitive output is connected to a specific sync channel. Channels are tagged in the same way as T2, however it is possible to data mine which sync period the photon derives from. This allows one the ability to deduce the time of arrival with respect to the total experimental time. A particularly useful feature of the Hydraharp software is the ability to insert external event

markers into the data stream fed as TTL input signals. This is unnecessary for coincidence measurements such as these however such high precision synchronisation tools are utilised in measurements described in later chapters. For coincidence detection at 2 μm, only two channels were required operated in T2 mode (one operating as a SYNC) and an example of a typical coincidence histogram is shown in Figure 3.6.

The coincidental arrival of the down-converted photon pairs is characterised by accumulated counts at the zero delay filtered in time by the bin size selected. The individual coincidence peaks were recorded throughout with a 256-ps time resolution (time bin window) and during later analysis, 10 bins were combined with an overall bin time of 2.6 ns. Experimentally, there is typically a non-zero delay between the main coincidence peak which can mostly be attributed to unavoidable experimental factors. Throughout this series of measurements, the accounted delay between the coincidence peak arrival was $\simeq$ 89.5 ns. The observation of the coincidence peak is accompanied by secondary peaks which occur periodically above the background noise distribution. These "accidental" peaks occur due to photons generated from different pulses arriving with periodicity associated directly to the repetition rate of the laser system which is our case was 80 MHz corresponding to delay shown in Figure 3.6 of $\delta t = 12.5$ ns. Accidental events occurred as a result of uncorrelated background photons, dark counts and event from down-converted photons arriving from earlier or later pulses.

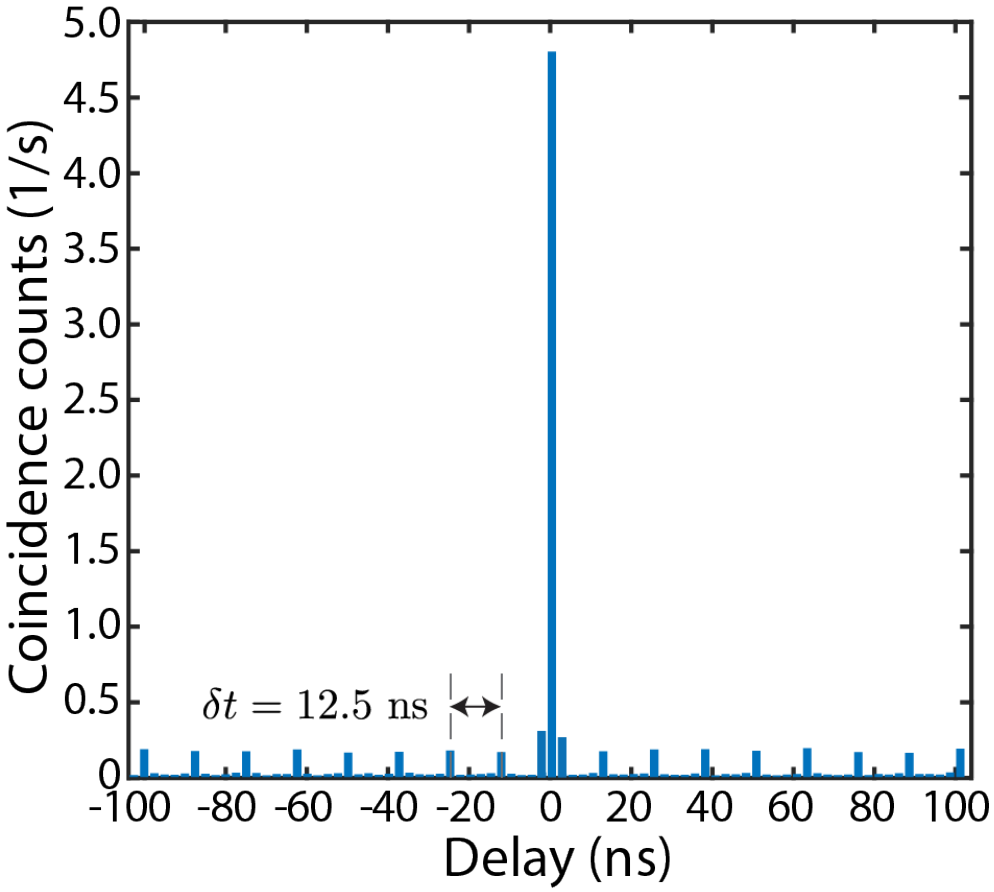

Figure 3.6: Coincidence measurement showing the expected peak at zero delay, with accidental peaks at the inverse of the laser repetition rate δt. The bin size considered is ~ 2.6 ns.

In order to quantify the number of photons which contribute to a typical coincidence histogram measurement, the most obvious starting point comes from the detection characteristics. One of the main challenges that arises from photon pair generation processes is the contamination of the useful single photon states with high photon number states and an important figure

of merit for quantifying the effect of this on a correlated photon pair source is the coincidence-to-accidental ratio (CAR). Explicitly, the CAR is defined as the ratio between coincidences from photon pairs generated from the same pulse (at zero delay) to the "accidental" coincidence events detected from different pulses visible 12.5 ns apart corresponding to the repetition rate of the laser source. A time correlation between signal and idler photons can be inferred when the CAR exceeds 1 and as the temporal correlations between photons increases, so does the measured CAR associated with the source [66]. In simplified form, the CAR can be defined by the expression,

$$CAR = M\frac{C\,R}{S_1\,S_2}\,, \tag{3.4}$$

where C is the raw coincidence counts between two detector channels, R is the laser repetition rate and S_1 and S_2 are single counts detected in detector 1 and 2. [66–68]. The number of temporal modes M was measured by performing a Hanbury-Brown and Twiss measurement where coincidences are recorded at the output ports of a 50:50 beam splitter when only the signal field is inserted. Given the thermal statistics of the SPDC field, the degree of second-order coherence at the zero delay value is related to the number of temporal modes M by the relation $g^{(2)}(0) = 1 + \frac{1}{M}$. The number of temporal modes used for the duration of these measurements was 1.8 ± 0.1 using a 50-nm bandpass filter centred at 2090 nm.

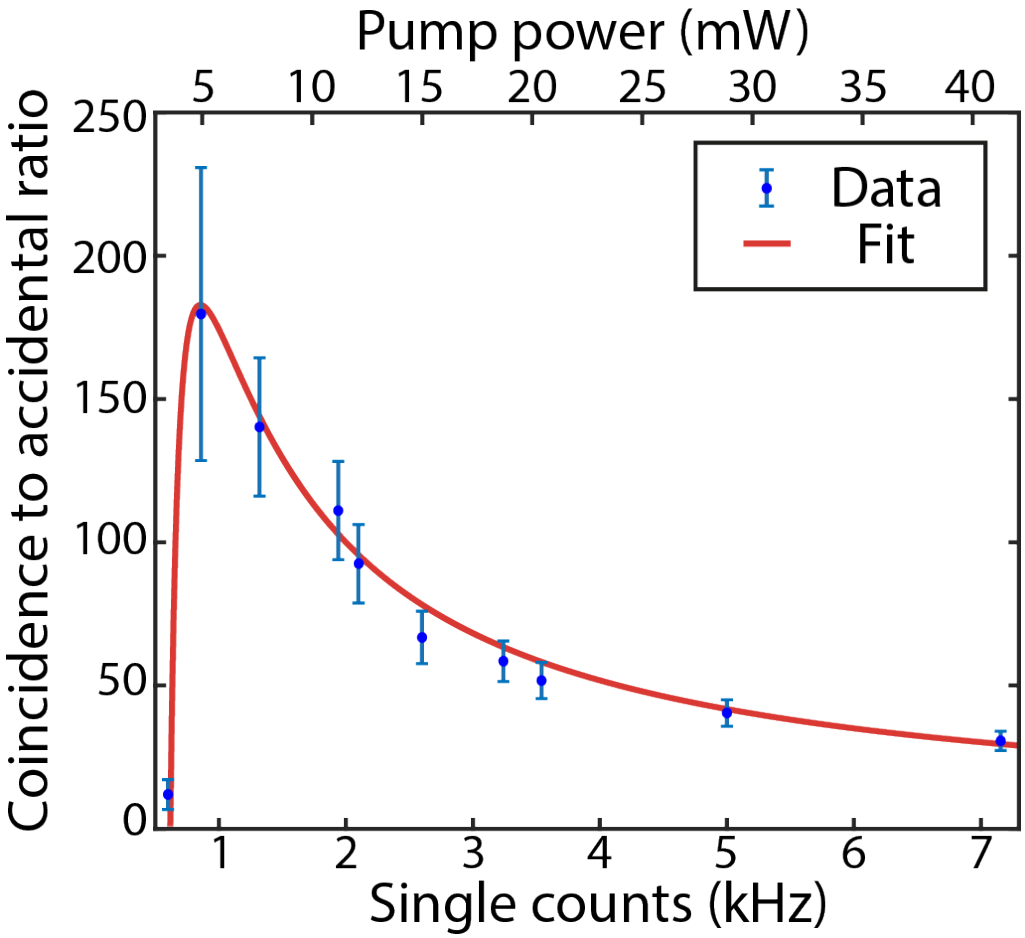

Figure 3.7: Measured coincidence-to-accidental ratio (CAR) as a function of the averaged single count rates between detectors 1 and 2. The red curve is a fitted CAR based on the model detailed in the main text.

The deterioration of the CAR with higher pump powers can be attributed to the convergence between coincidence signal and noise counts. At increasing pump powers there is an increased probability of generating multiple photons per pulse which suppresses the CAR by contributing to additional accidental counts. The trend of the measured CAR against single counts detected (and

input pump power) is shown in Figure 3.7. The effects on the coincidence histogram (and the resultant CAR) from both very low (<< 2 mW) and higher pump powers (>> 40 mW) are shown in Appendix A for reference. In the condition when very low pump powers (<< 2 mW) are used, the effects of the detector dark counts and noise photons start to dominate over generated counts [69, 70]. The recorded dark count rates for detectors 1 and 2 used were $\simeq$ 600 Hz and $\simeq$ 550 Hz respectively which are included in all singles counts used throughout. As shown in Figure 3.7, the CAR peaks at a maximum measured CAR of 180 ± 50 with an input pump power of $\simeq 5$ mW corresponding to singles counts of $\approx$ 960 Hz and $\approx$ 760 Hz. Each data point was measured for an integration time of 30 minutes with a bin size of 2.6 ns. The fit used to model the CAR can be defined by

$$CAR = 1 + \frac{\alpha\eta_1\eta_2}{(\alpha\eta_1 + d_1)(\alpha\eta_2 + d_2)}\,, \tag{3.5}$$

where α is the average number of photon pairs per pulse, d_1 and d_2 are the dark counts per pulse for channels 1 and 2 for detectors with respective total efficiencies η_1 and η_2 [62, 66, 69]. The channel efficiencies used here combined the measured detection efficiencies of the single-photon detectors and losses associated with propagation, coupling, filters used etc detailed later in the chapter. This high CAR result demonstrates the production of high purity correlated photon-pairs at the degeneracy wavelength of 2.1 μm from the source used. The next step in the characterisation process of

the SPDC source was to expand the measurement setup to investigate the indistinguishability of the photon-pairs using two-photon interference.

3.3.2 Characterisation of losses and detection efficiencies of single-photon detectors

Throughout this series of measurements, custom designed twin SNSPD's were used which were optimised for absorption of mid-infrared radiation. Fabricated by collaborators at James Watt School of Engineering at the University of Glasgow, each SNSPD device consisted of a backside-illuminated NbTiN nanowire (which were 60 nm wide and 6 nm thick) meandered over a 15 μm by 15 μm active area and inserted into an optical cavity with a 600 nm thick SiO_2 dielectric layer custom designed to improve absorption at the wavelength of interest [71, 72]. The SNSPD's operate at a working temperature of close to 2 K and are therefore mounted in a close cycle Gifford McMahon cryostat. In experimental working condition, the SNSPDs used throughout these measurements had dark count rates of 600 Hz for channel 1 and 550 Hz for channel 2. The custom active area design of the cavity and nanowire dimensions combined with using SM2000 single-mode fibres throughout helped improve the efficiency of detection at 2.090 μm. In order to characterise the SNSPD's at the target wavelength, an optical parametric oscillator (OPO) from Chromacity Ltd. was used as a source. The spectrally broad output of the OPO was filtered using the same bandpass filter used throughout the experiment and the flux subsequently attenuated using non-dispersive filters to closely control the detector input power. Measurement of the detector efficiency was performed by calculating the difference between photon count

rate and detector dark counts before dividing by the photon flux (set at 0.5 photons per pulse). The measured detection efficiency for each of the two SNSPD's, including the fibre losses inside the cryostat, was 2.0 ± 0.2 % for detector 1 and 1.0 ± 0.1% for detector 2 [62]. The polarisation dependence of the SNSPD's (measured using an optical parametric amplifier source at a wavelength of 2.3 μm) was ± 25 %. Replicating the same measurement independently with the down-converted radiation filtered with the same bandwidth as used in the series of measurements (50 nm) obtained the same quantum efficiency value. Characterisation of the experimental losses was performed by accumulating the full losses in both signal and idler paths through to the detector input. The measured transmission for the AR-coated Germanium filter and 50 nm bandpass filter at 2 μm were were 0.808 ± 0.001 and 0.65 ± 0.01. Transmission through the 15 m of SM2000 fibre was estimated to be $\simeq$ 0.8. After the splitting of the down-converted field by the D-shaped mirror, the total coupling efficiency of the SPDC into the SM2000 fibre for channel 1 was measured to be 0.1 ± 0.05. The overall transmission from crystal to the detector input for channel 1 was $\simeq$ 0.04 ± 0.01 which corresponds to 14 dB loss. The coupling efficiency for channel 2 was around three times the coupling for channel 1 and as a result of this the transmission for channel 2 was $\simeq$ 0.12 for a loss of 9 dB.

3.4 Two-photon interference in the mid-infrared

3.4.1 Theoretical background of two-photon interference

The two-photon interference effect can not be understood in significant depth without considering the simple geometry of the system. At the core of two-photon interference is understanding of the behaviour of two input modes incident on a beam splitter. A simple insight into this remarkable effect can be obtained by considering the action of a lossless beam splitter on two photons considered here to be identical in all degrees of freedom. The beam splitter consists of two input ports (a, b) and two output ports (c, d) and there are four obvious possibilities to be considered once two modes enter the system depending on the transmission T and reflection R coefficients of the beam splitter. In the specific case of a lossless 50:50 beam splitter, these coefficients are confined to the equation $|R| = |T| = \frac{1}{\sqrt{2}}$ where both are considered to be real [73]. Quantum mechanically, the action of the beam splitter can be defined explicitly by the unitary operator

$$\hat{U} = exp\left[\frac{\theta}{2}(\hat{a}^{\dagger}\hat{b} - \hat{a}\hat{b}^{\dagger})\right], \tag{3.6}$$

where θ is the effective angle used to define T and R coefficients [74]. Referencing the quantum notation for creation ($\hat{a}^{\dagger}$, $\hat{b}^{\dagger}$) and annihilation

($\hat{a}$, $\hat{b}$) operators defined in previous chapters, the unitary transformations associated for two output modes associated with annihilation operators $\hat{c}, \hat{d}$ are defined by

$$\hat{c} = \hat{U}^{\dagger}\hat{a}\hat{U} = \sqrt{T}\hat{a} + \sqrt{R}\hat{b}\,, \tag{3.7}$$

$$\hat{d} = \hat{U}^{\dagger}\hat{b}\hat{U} = \sqrt{T}\hat{b} - \sqrt{R}\hat{a}\,, \tag{3.8}$$

using the two input modes $\hat{a}$ and $\hat{b}$ [2]. In order to measure a coincidence event, single photons must exit each port of the beam splitter however two of the four possible outcomes result in both photons being transmitted or both being reflected. The probability of the coincidence detection P_c of an input state of the form $|\Psi_{in}\rangle = |1_a\, 1_b\rangle$ at output ports c and d can be described by

$$P_c = \langle \Psi_{in}|\hat{c}^{\dagger}\hat{d}^{\dagger}\hat{d}\hat{c}|\Psi_{in}\rangle = |T - R|^2 = 0\,, \tag{3.9}$$

where a cancellation of the coincidence events occurs when a perfect 50:50 beam splitter is used [2, 75]. This destructive interference effect occurs when the path equivalence condition is met and the photons are entirely indistinguishable. Once the temporal arrival time difference exceeds the coherence length of incident photons, the interference effect disappears and the coincidences occur with probability of 1/2. Further developing the interpretation of the effect of beam splitting operation, the output state evolves according to $|\Psi_{out}\rangle = \hat{U}\,|\Psi_{in}\rangle$. For an input two-photon Fock state input such as $|1_a\, 1_b\rangle$,

the output state can then be defined by

$$|\Psi_{out}\rangle = (T - R)\,|1_c\,1_d\rangle + \sqrt{2RT}\,|2_c\,0_d\rangle - \sqrt{2RT}\,|2_c\,0_d\rangle\ , \tag{3.10}$$

which clearly shows the resulting photon bunching effect when the first term tends to zero. The coincidence cancellation ensures interacting photons under these conditions exit the beam splitter via the same output ports and the resulting two-photon state is given by

$$|\Psi_{out}\rangle = \frac{1}{\sqrt{2}}\,|2_c\,0_d\rangle + |2_c\,0_d\rangle\ , \tag{3.11}$$

which can also be identified as the well-known N = 2 NOON state used in quantum metrological applications [76–79]. This result demonstrates the Hong-Ou-Mandel (HOM) effect recognised by the signature cancellation of the coincidence rate known by the HOM dip shown in Figure 3.8.

To further understand the remarkable cancellation of the coincidence signal and the properties of the HOM dip associated with it, its important to better define the pulsed SPDC field used in the measurements performed throughout this project. The behaviour of the number of coincidences N_c as stated in [28] can be observed by

$$N_c = C(T^2 + R^2)\left[1 - \frac{2RT}{R^2 + T^2}e^{-(\Delta z \Delta\omega)^2}\right], \tag{3.12}$$

where Δz is the path difference between the interacting photons and $\Delta\omega$ is

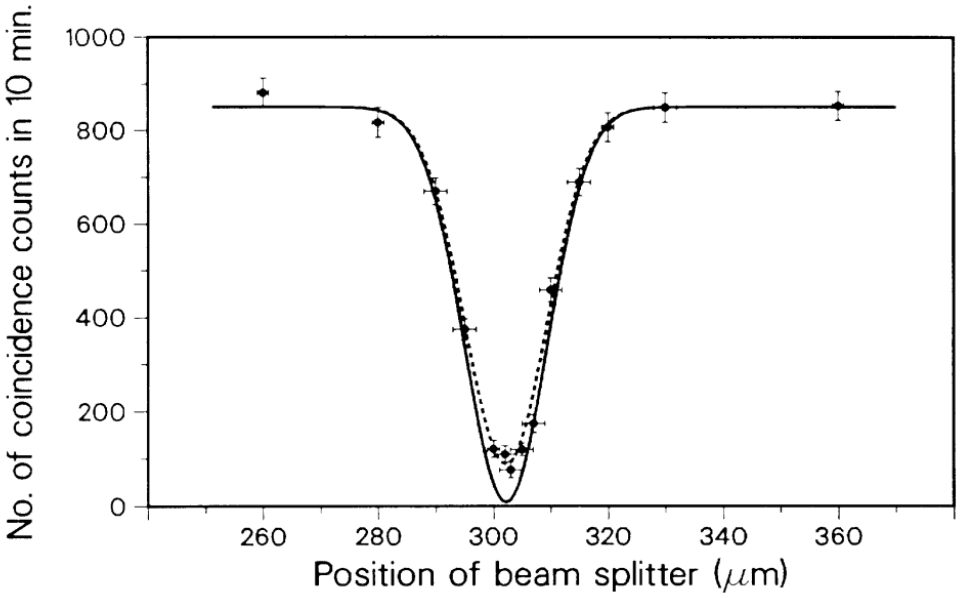

Figure 3.8: The characteristic HOM dip showing the cancellation of the coincidence counts as a function of the delay [27]. Figure reproduced from "Measurement of subpicosecond time intervals between two photons by interference", Phys. Rev. Lett. 59, 2044 (1987).

related to the bandwidth of the state. Clearly, in the condition when Δz=0 then the number of coincidences N_c tends to zero. The shape characteristics of the HOM dip depends on the bandwidth of the pump used and hence a wideband pumping regime must be modelled in order to accurately describe the experimental conditions presented here. In the ultrafast pulsed regime, the correlation function $G^{(2)}$ between signal and idler is dominated by the pump envelope and the phase matching function h(L) defined in [2]

$$h\left(L\right) = \mathrm{sinc}(L/2)\, e^{-iL/2}\,, \tag{3.13}$$

where L is the length of the non-linear crystal used. This convolution of the Gaussian pump envelope and the phase matching function $h(L)$ alters the shape of the traditionally recognised Gaussian HOM dip presented in [28] changing the behaviour at regions narrowly outside the dip as observed in later experimental results.

3.4.2 Two-photon interference at 2.1 μm

In order to understand the indistinguishably of the mid-infrared photon pairs, two-photon interference was demonstrated using a HOM measurement setup. The dependence of the indistinguishability of the correlated photons is investigated by altering the experimental coincidence setup previously described. In this measurement, the spatially separated signal and idler photons are coupled into two input ports of a 50:50 polarisation-maintaining (PM) fibre beamsplitter. The 2 × 2 port fibre beamsplitter (Nufern) was specifically designed for 2080 nm with a bandwidth of ≈ 80 nm and the fibre was 1 m in length. The changes to the experimental setup are shown in Figure 3.9 below.

One significant change comes by mounting the input fibre couplers on motorised translational stages to provide control on the delay between the paths of each mode. In order to observe the cancellation of coincidence signal at the output ports, the photons must be indistinguishable in all degrees of freedom. By providing 50 nm resolution motorised delay control between paths by moving the fibre couplers, the manufacturing inaccuracies in the specifications of the fibre beamsplitter could be overcome. It is also worth noting that each path was filtered with a 50 nm bandpass (and Germanium filter) prior to entering the fibre beamsplitter. The coincidences recorded between the two output ports of the fibre beamsplitter are measured in the same way defined before. The single count rates throughout this measurement were

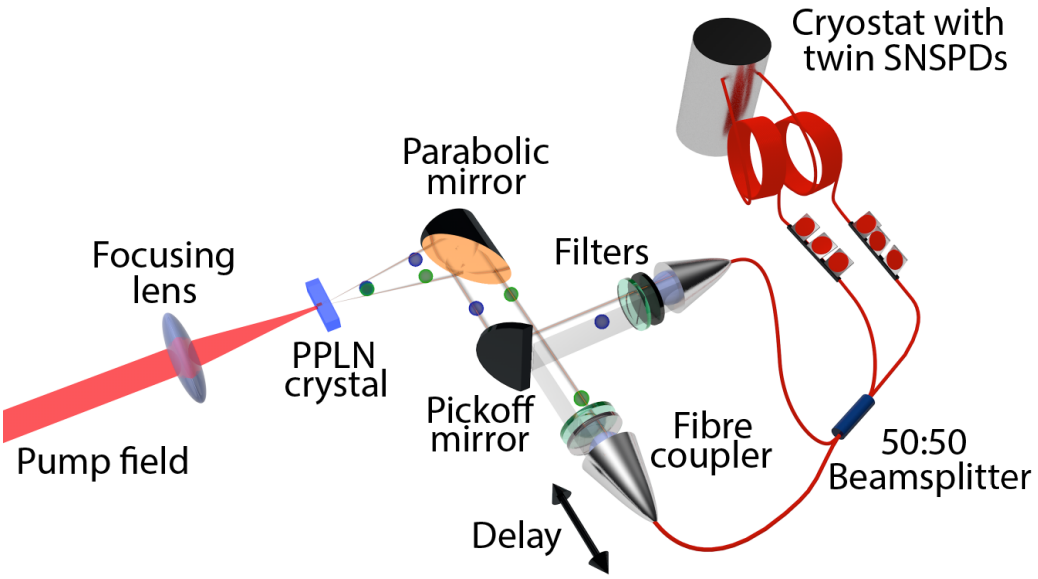

Figure 3.9: Experimental setup for demonstrating two-photon interference at 2.1 µm. The spatially separated down-converted photons are recombined on a custom 50:50 beamsplitter and coincidence detection performed at the output ports. Temporal overlap is controlled using a fibre coupler mounted on a motorised delay stage.

around 2000 Hz with dark counts around 300 Hz throughout recorded with 512-ps resolution. To perform this measurement, the recorded coincidence counts at the output were measured as a function of a sweep of delay between photon arrival times. In order to ensure an useful range of motion, the coupler was mounted on motorised stage at the centre of the 25 mm travel distance to allow tunability. The alignment of this stage was tested to ensure movement of the stage led to no loss in counts landing on the detectors.

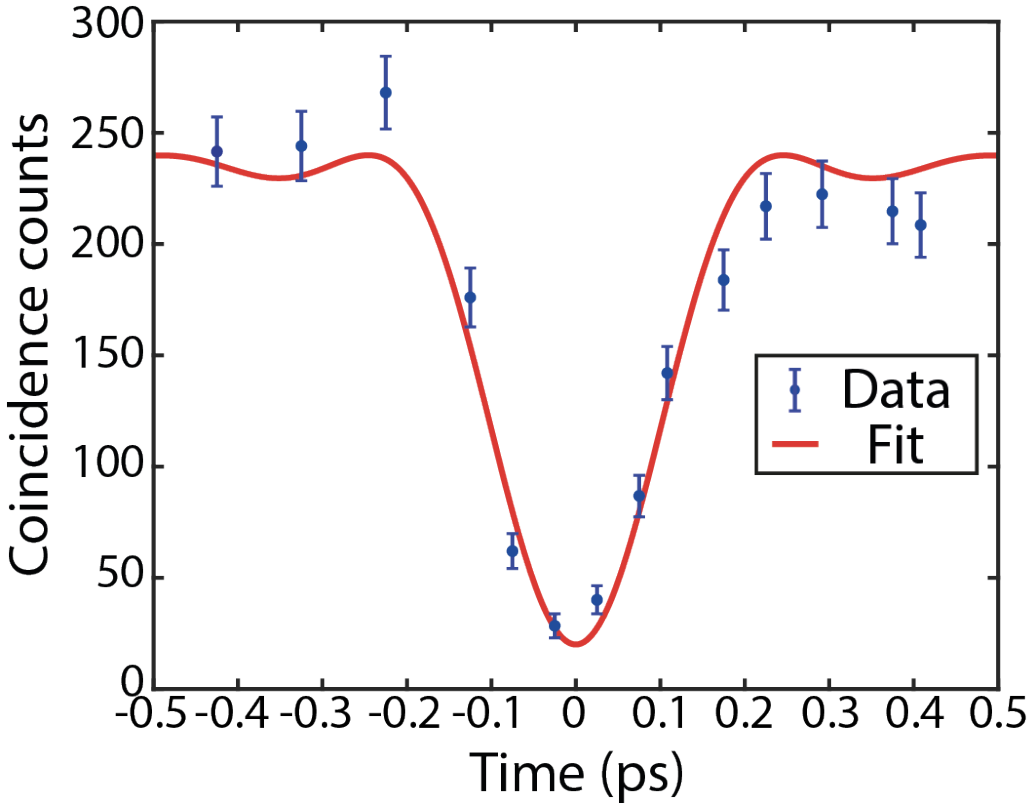

Figure 3.10: The observed two-photon interference (HOM dip) at 2.1 μm. The experimental coincidence counts (blue dots) measured as a function of the delay between arrival time of photon pairs. The fit to the experimental data (red curve) is detailed in text. The integration time required for each data point is 1 hour.

The renowned HOM dip which characterises indistinguishability via photon interference is shown in Figure 3.10 depicting the cancellation of the raw coincidence signal data (blue dots) between signal and idler at zero delay. The error bars associated for each data point were estimated by using Poissonian statistics. The raw data set was fitted with a Gaussian-weighted inverted sinc function (red line) which helped facilitate the approximation of the visibility

of the HOM dip as expected from the theory of pulsed SPDC. Explicitly, the signal-idler correlation function is given by the convolution of the phase matching function (sinc) and the pump envelope (Gaussian) [2]. By considering the minimum coincidence data point obtained inside the dip coupled with a maximum coincidence value far away from the zero-delay region using the fitting function, a visibility of 88.1 ± 1.1 % was obtained. There are asymmetries in the oscillatory behaviour at regions outside of the HOM dip hence these points were unsuitable for calculating the visibility. The good visibility in the dip proves the generation of intrinsically correlated photon pairs at 2.1 μm clearly demonstrating this source can be successfully used for interferometric measurements.

3.5 Polarisation entanglement in the mid-infrared

3.5.1 Theoretical background of polarisation entanglement

In 1935, Einstein, Podolsky and Rosen presented a thought experiment designed to test the completeness of the theory of quantum mechanics. The infamous "EPR paradox" postulated that quantum mechanics is unable to completely describe physical reality and a more complete description required the introduction of further unknown parameters [80]. The proposed existence of local *hidden variables* would account for standard predictions of quantum mechanics without conceding "spooky action at a distance" restoring causality and locality. Niels Bohr's refutation of the framing of the EPR paradox focused on the complementary principle of some measurement properties and the resulting uncertainty associated with them [81]. David Bohm grappled with this argument for a two-photon state entangled in the basis of linear polarisations in the form

$$|\Psi^{\pm}\rangle = \frac{1}{\sqrt{2}} |H\,V\rangle \pm |V\,H\rangle \ , \tag{3.14}$$

where the horizontal and vertical polarisations (H and V) are defined [82]. The unique nature of this polarisation entangled Bell state cannot be solely attributed to each photon individually but according to quantum mechanics,

measurement of one polarisation concedes information on the polarisation of the other. However, the Bohr-Einstein debate was thrust back into the scientific consciousness in 1964 when John Bell published his groundbreaking paper detailing a mathematical mechanism to test for hidden variables. Violation of Bell's inequality with entangled particles set out mathematically the incompatibility of hidden variables with quantum mechanics [83]. Bell's argument detailed that if we consider a hidden variable theory (HVT), then the independent outcomes of spin (polarisation) measurements at each detector are uncorrelated and are solely determined by the single spin (polarisation) values and a hidden variable, λ. To satsify the conditions of the proposed HVT, the hidden variable λ was described by the probability distribution $\rho(\lambda)$ such that $\int \rho(\lambda)d\lambda = 1$ and $\rho(\lambda) \geq 0$ [84, 85]. The independent measurement of the polarisation of each photon can be defined by functions $A(\theta_A, \lambda)$ and $B(\theta_B, \lambda)$ where θ_A and θ_B are the linear polarisation bases of detection restrained to either vertical or horizontal (1 or -1). Under these conditions, the polarisation correlation coefficients can be written in the form

$$E_{HVT}(\theta_A, \theta_B) = \int \rho(\lambda) A(\theta_A, \lambda) B(\theta_B, \lambda) d\lambda \,, \tag{3.15}$$

which denotes one of the four possible polarisation orientations related to polariser angle θ_A and θ_B. By accumulating the four possible polarisation orientations and their respective correlation coefficients, the Clauser-Horne-

Shimony-Holt (CHSH) form of Bell's inequality can be defined generally by

$$S \equiv |E(\theta_A, \theta_B) - E(\theta_A, \theta'_B)| + |E(\theta'_A, \theta_B) + E(\theta'_A, \theta'_B)| \leq 2 \int \rho(\lambda) d\lambda \,, \tag{3.16}$$

where θ_A, θ'_A, θ_B, θ'_B are four alternate orientation angles which contribute to each correlation coefficient E [86]. Considering previous conditions, the CHSH inequality in its simplified form denotes that if the sum of correlation coefficients exceed $-2 \leq S \leq 2$ then this is experimental proof that HVT's are not compatible with quantum mechanical predictions [87]. This is useful for showing particular quantum states experimentally predict S values in violation of the inequality. However there are some external experimental factors which can come into play. If the visibility, V, of the sinusoidal behaviour of the coincidence rates are not maximised, then the S parameter will be reduced. It is generally understood that a coincidence rate visibility of $V > 71\%$ is required to violate the inequality however this is not always essential. For the remainder of this thesis, a two-photon Bell polarisation entangled state such as the $|\Psi^-\rangle$ state generated in our measurement will be measured in numerous polariser orientations to show violation of the CHSH inequality and clearly demonstrating entanglement.

3.5.2 Polarisation entanglement at 2.1 μm

In order to characterise polarisation entanglement in the mid-infrared spectral region, a polarisation entangled state in the form of the Bell state $|\Psi^-\rangle$ was generated using a Type-2 SPDC configuration. Similar to the previous crystal characterisation, the Type-0 crystal was replaced with a 300 μm thick MgO-PPLN crystal which was optimised for Type-2 SPDC phase matching at a poling period of 13.4 μm. The temperature of the crystal was optimised for phase matching at 110 °C. Due to the reduced efficiency of the Type-2 crystal compared with the Type-0 configuration, this characterisation was performed directly with single photon counting using a 50 nm filter with the SNSPD's used throughout (see Appendix B for characterisation data). The modifications to the previous setups are detailed in Figure 3.11. The generated polarisation entangled two-photon singlet state is of the form

$$|\Psi^-\rangle = \frac{1}{\sqrt{2}} |H\,V\rangle - |V\,H\rangle \ , \tag{3.17}$$

where H and V are the orthogonal linear polarisations expected from Type 2 generation. The Type 2 PPLN crystal used was shorter than the Type 0 PPLN crystal to minimise the impact of the group velocity mismatch between the orthogonally polarised signal and idler on the measurements. Assuming that signal and idler are generated in the centre of the 300 μm thick crystal, the group velocity mismatch between orthogonal polarisations is 40 fs which is a fraction of the pulse duration. The signal and idler photons should be

temporally overlapped within the biphoton correlation time defined by the filter used (50 nm bandpass) which is around 290 fs. Temporal compensation would be required as the crystal length approaches 1 mm where group velocity mismatch exceeds 300 fs. Further work using this Type 2 crystal source has demonstrated a nine-fold improvement in degree of entanglement approaching the theoretical maximum violation possible without the requirement of temporal compensation [63]. The polarisation correlation measurements are performed by inserting half wave plates (HWP) and polarisers in each detection arm (identified as A and B) before coupling to the SNPSD's for coincidence detection as detailed earlier in this chapter. In combinination with HWP's orientated at $\theta_A/2$ and $\theta_B/2$, vertical polarisers help project the correlated photons onto measurement bases defined as θ_A and θ_B. As before, the photons were filtered using an AR-coated Germanium filter and 50 nm bandpass filter to select SPDC photons at the degenerate wavelength of 2.1 μm before coincidence detection with a 512-ps gating window. The coincidence count rates C as a function of particular pair of polarisation angles θ_A and θ_B were then measured.

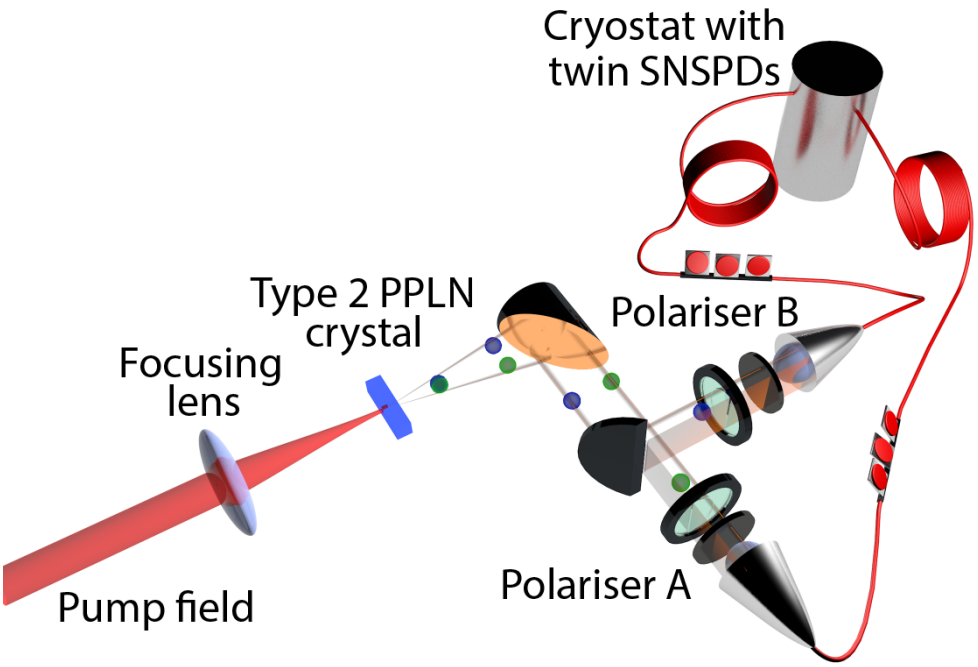

Figure 3.11: Experimental setup for characterisation of entangled photon pairs at 2.1 µm. Using a Type-2 PPLN crystal, coincidences were recorded for different angle orientations of tunable polarisers A and B before each single-photon detection.

The correlation coefficients measure the polarisation constraints imposed by the Bell inequality and can be defined

$$E(\theta_A, \theta_B) = \frac{C(\theta_A, \theta_B) + C(\theta_A + \beta, \theta_B + \beta) - C(\theta_A, \theta_B + \beta) - C(\theta_A + \beta, \theta_B)}{C(\theta_A, \theta_B) + C(\theta_A + \beta, \theta_B + \beta) + C(\theta_A, \theta_B + \beta) + C(\theta_A + \beta, \theta_B)}, \tag{3.18}$$

where β represents a 90° polarisation angle shift. Since for each quantum state there exists four projection measurements and we are considering two photon states with two possible polarisations, a collection of 16 total mea-

surements are required. The usual form for the CHSH inequality is again defined by,

$$S \equiv |E(\theta_A, \theta_B) - E(\theta_A, \theta'_B)| + |E(\theta'_A, \theta_B) + E(\theta'_A, \theta'_B)| \leq 2\,, \tag{3.19}$$

where θ_A, θ'_A, θ_B, θ'_B are four alternate orientation angles that contribute to each correlation coefficient E as a function of coincidence count rate $C(\theta_A, \theta_B)$ [86]. Violation of this condition represents the validity of a non-local model of reality and constrains the polarisation correlation as a function of polariser angular displacement [88]. For the $|\Psi^-\rangle$ state defined above, coincidence measurements were performed for a combination of 16 orientation angles of $\theta_A = 0$, $\theta'_A = \frac{\pi}{4}$, $\theta_B = \frac{\pi}{8}$, $\theta'_B = \frac{3\pi}{4}$. This combination results in the maximum output of the CHSH inequality, $S_{TB} = 2\sqrt{2}$ known as the Tsirelson bound which violates the Bell inequality and thus disproves all hidden variable theories [87, 89]. A results table containing the measured coincidence counts for the N=16 combinations of orientation angles resulting in maximal violation of the CHSH inequality in the case of the $|\Psi^-\rangle$ state is shown in Figure 3.12.

The S parameter corresponding to the source was determined to be

$$S \equiv |-0.5799 - 0.4095| + |-0.5944 + (-0.6129)| = 2.1967 \pm 0.0886\,, \tag{3.20}$$

clearly demonstrating entanglement violating the CHSH inequality by more

N	θ_a	θ_b	C	N	θ_a	θ_b	C
1	0	$\pi/8$	36	9	$\pi/4$	$\pi/8$	65
2	0	$5/8\pi$	164	10	$\pi/4$	$5/8\pi$	164
3	0	$3/8\pi$	121	11	$\pi/4$	$3/8\pi$	51
4	0	$7/8\pi$	48	12	$\pi/4$	$7/8\pi$	162
5	$\pi/2$	$\pi/8$	136	13	$3/4\pi$	$\pi/8$	89
6	$\pi/2$	$5/8\pi$	36	14	$3/4\pi$	$5/8\pi$	41
7	$\pi/2$	$3/8\pi$	24	15	$3/4\pi$	$3/8\pi$	105
8	$\pi/2$	$7/8\pi$	162	16	$3/4\pi$	$7/8\pi$	20

Figure 3.12: Measurement settings for the CHSH-Bell test for N = 16 orientations of polariser angles θ_A and θ_B to obtain raw coincidence counts (C) used to determine the Bell parameter S = 2.20 ± 0.09, demonstrating polarisation entanglement at 2.1 μm. The integration time was 30 min for each measurement.

than 2 standard violations [90]. Considering the Poissonian statistical error associated with photon detection from the ith coincidence measurement C_i, the uncertainty associated with the S parameter, σ_S can be defined by

$$\sigma_S = \sqrt{\sum_{i=1}^{16} C_i \left(\frac{\partial S}{\partial C_i} \right)^2}, \tag{3.21}$$

where i=1,...,16 is the number of measurement orientations [89]. However, in order to unconditionally confirm a violation of Bell's inequality, the fringe

visibility must be defined to exceed the threshold

$$V = \frac{C_{max} - C_{min}}{C_{max} + C_{min}} \geq \frac{1}{\sqrt{2}}\,, \tag{3.22}$$

where C_{max} and C_{min} correspond to the maximum and minimum coincidence counts measured. Only when the visibility exceeds $\frac{1}{\sqrt{2}}$ and the CHSH inequality $S \geq 2$, can we accept that hidden variable theories are incompatible with quantum mechanics. For the coincidence count rate $C(\theta_A - \theta_B)$, the visibility corresponding to the measured CHSH-Bell parameter obtained was $\mathrm{V} = 77.8 \pm 0.1\%$. It is worth noting here that the polarisation dependence of the SNSPD's used in this measurement was ± 25 %. This was characterised using an optical parametric amplifier source at a wavelength of 2.3 μm. In the Bell test measurements above, the input into the detectors was adjusted by fibre polarisation control for maximum coupling to each SNSPD which is shown in each experimental setup figure for these series of measurements. This was important to ensure the removal of any polarisation dependence of the individual detectors on the measurement as described in [62].

3.6 Discussion and future work

This work has demonstrated the generation, manipulation and detection of entangled quantum states in the mid-infrared spectral region for the first time in free-space. The non-classical properties of this free-space SPDC source was characterised in order to demonstrate its potential to be used for future quantum technology applications. The work conduced here provides a platform for quantum optics and lays the foundations for mid-infrared applications in such as quantum sensing and long distance quantum-secured communications [62]. Considerable challenges were overcome to open the 2- to 2.5- μm window for the advancement of quantum technologies in this area. The underdevelopment of robust quantum sources, detectors and general optical components in the mid-infrared region made this project seem like an uphill battle. Having no available means in the lab to image the SPDC at 2 µm made these measurements significantly tougher. With detection efficiencies including cryostat coupling at 2 µm of $\leq 3\%$, the rate of entangled photons measured with this source was reduced and the coincidence visibility affected by detector dark counts. Future advancements in this spectral region would greatly benefit from the development of superconducting nanowire single-photon detectors (SNSPD) with near-unity system detection efficiency (SDE) similar to which are already possible at telecom wavelenghs [91, 92]. Recent advancements in SNSPD's for mid-infrared wavelengths have exhibited detection efficiencies of 63 % for 2 µm which is promising for future

applications in the spectral regime [93, 94]. Greater than 70 % SDE has very recently been published [95] with some commercial systems (ID Quantique) reporting similar efficiencies at this wavelength. Alternative schemes have been reported which take advantage of near-unity single-photon detection efficiencies at other wavelengths by demonstrating upconversion using infrared photons [49, 96]. Free-space photon counting applications in the mid-infrared have also been demonstrated using state-of-the-art low noise SNSPD's to perform LIDAR with a low power 2.3 μm source. Operating at this wavelength offers reduced atmospheric absorption and the ability to use lower powers at an eye-safe level [97].

By experimentally verifying the indistinguishability of the correlated photon pairs at 2.1 μm using two-photon interference to obtain a high visibility HOM dip, this demonstrates that this source could be used for interferometric measurements in the mid-infrared. Recent gravitational wave detector upgrade proposals at LIGO have highlighted squeezed sources of light at 2 μm as crucial to enhancing the system sensitivity by reducing scattering and losses from silicon test masses [98]. The advantages of transitioning to a mid-infrared operating wavelength can also be observed in integrated silicon photonics where scaling and functionality aren't an issue but non-linear losses at telecom wavelengths can be excessive. Recent work has demonstrated in silicon waveguides the reduction in two-photon absorption rates and the generation of entangled photon pairs with high visibility two-photon interference at 2 μm [60].

The free-space configured source developed in this work has provided the foundations for closely related projects in our research group namely demonstrating near-maximal polarisation entanglement in the mid-infrared and the feasibility of using this source for device independent quantum key distribution (DIQKD) [63]. Realisation of free-space DIQKD in the 2- to 2.5- μm region could take advantage of reduced solar irradiance and lower atmospheric absorption in comparison to telecom alternatives. This demonstration may help enable full day functionality of free-space QKD which is a major requirement in the vision of a worldwide quantum network. However, this vision of worldwide QKD optical links will require seamless integration of both free-space and integrated platforms and stable coupling of free-space radiation into fibre. One potential fibre solution previously discussed which may demonstrate low losses at 2 μm are novel hollow-core fibres (HC-PBGF's). These types of fibres have been proposed to provide significant enhancement in channel capacity over current network infrastructure and identify minimal attenuation at 2 μm [56]. Advancements in hollow core fibre technology have identified significant improvements in optical performance using a Nested Antiresonant Nodeless Fibre (NANF) design. Recent breakthrough publications using NANF have demonstrated record low attenuation in telecom wavelengths of 0.28 ± 0.04 dB/km [99]. However, NANF technology has yet to be extensively deployed in the mid-infrared region. In the next chapter of this thesis, the performance of a custom manufactured NANF will be tested at 2 μm and the polarisation purity properties of the

fibre characterised. This helps provide a platform for the feasibility of more ambitious measurements demonstrating the propagation of quantum states thru hollow core fibre technologies at 2 μm.

Chapter 4

Hollow core fibre propagation in the mid-infrared

4.1 Introduction to hollow core fibre technology

Hollow core fibre technology has the potential to exceed conventional optical fibre transmission performance. Research efforts into alternative transmission media to meet ever-increasing communication demands have resulted in the development of hollow core waveguides with attenuation properties which are fast approaching conventional SMF performance [100]. In recent times, hollow core fibre waveguides at visible and telecom wavelengths have attracted some attention offering low attenuation performance with no bend loss [56, 101, 102]. By confining light to an air core, these waveguides demon-

strate extremely low fibre latency and lower non-linearities than conventional solid fibres [58, 103]. Hollow core fibres can generally be split into two main categories: photonic bandgap fibres (HC-PBGF) and anti-resonant fibres (HC-ARF). The former is based on guiding light using an air core using a periodic structure in the cladding to create a photonic bandgap confining photons inside. PBGF's typically demonstrate low loss propogation and bend robustness however they are is limited in terms of bandwidth. The inherent nature of these fibres allows confinement over a certain range of frequencies and therefore research tends to focus on bandwidth enhancement [104]. ARF designs are an active research area where irregular cladding structures surround the hollow fibre core to reduce transmission loss [100].

ARF designs tend to offer a much wider bandwidth than PBGF's but with high bend sensitivity [104]. One particular design of novel fibre has been found to combine the attractive properties of PBGF's and ARF's. The nested anti-resonant nodeless fibre (NANF) design traps light in a hollow core surrounded by 6 nested non-touching parallel tubes aligned along the outer core. The NANF design is fast approaching the ultra-low propagation loss demonstrated in conventional silica fibre of 0.17 dB/km [105]. Recent breakthrough publications using NANF have demonstrated record low attenuation in telecom wavelengths of 0.28 $\pm$ 0.04 dB/km [99]. Figure 4.1 shows a comparison between the measured loss for different types of HCF's. NANF technology has been used extensively to test non-linearities in the mid-infrared region, e.g. to generate super continuum spanning from 1.85

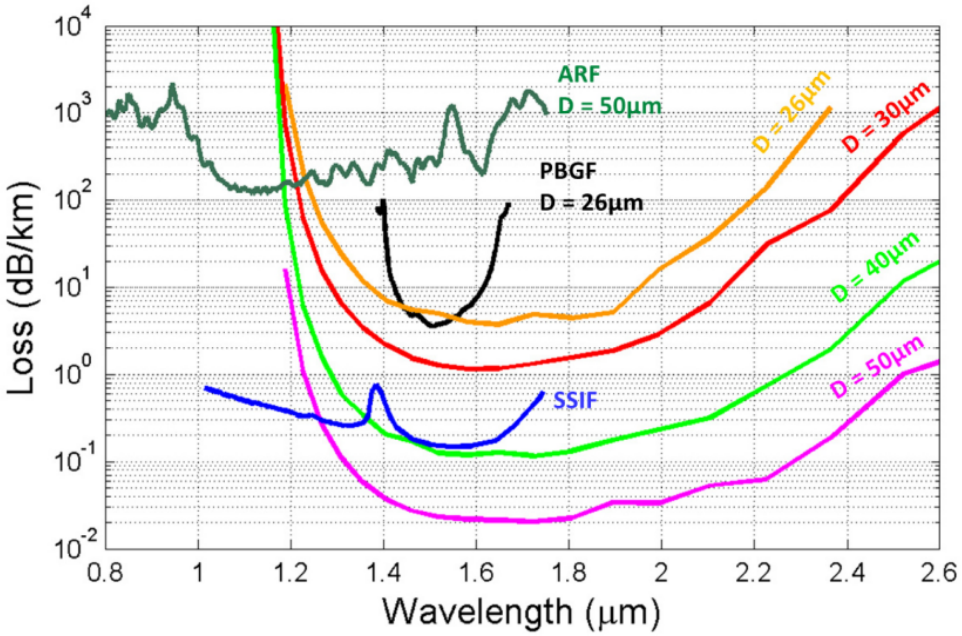

Figure 4.1: Comparison of measured loss of PBGF, ARF and NANF designs (of core diameter, D) with varying wavelength [100]. Figure reproduced from "Nested antiresonant nodeless hollow core fiber", Opt. Express 22, 23807-23828 (2014).

to 5.20 µm and to build a tunable OPO [106, 107]. However, few studies have targeted hollow core fibres for quantum applications. This work takes a step in the direction of understanding the applicability of hollow core fibre technology in propagating quantum states of light at 2 µm. The wider goal of this work is to demonstrate that its possible to propagate quantum states of light (polarisation entangled or time-bin etc.) via hollow core fibres in the hardly accessible 2 µm spectral region.

4.2 Polarisation purity of NANF at 2 μm

4.2.1 Characterisation of properties of NANF

The 6 nested tube NANF (N31-07-B1) provided by the manufacturer for testing was of length 1.177 km with fibre glass diameter of 232 ± 0.5 μm and coated diameter of 385 ± 1 μm. A cross-section of the structure of the NANF being tested is shown in Figure 4.2. The scanning electron micrograph (SEM) cross section shows the relative scale of the 6 nested tubes surrounding a central core of diameter of 36.2 μm. Test data on the attenuation and transmission of the NANF over a range of wavelengths was provided by the manufacturer and is also shown in Figure 4.2.

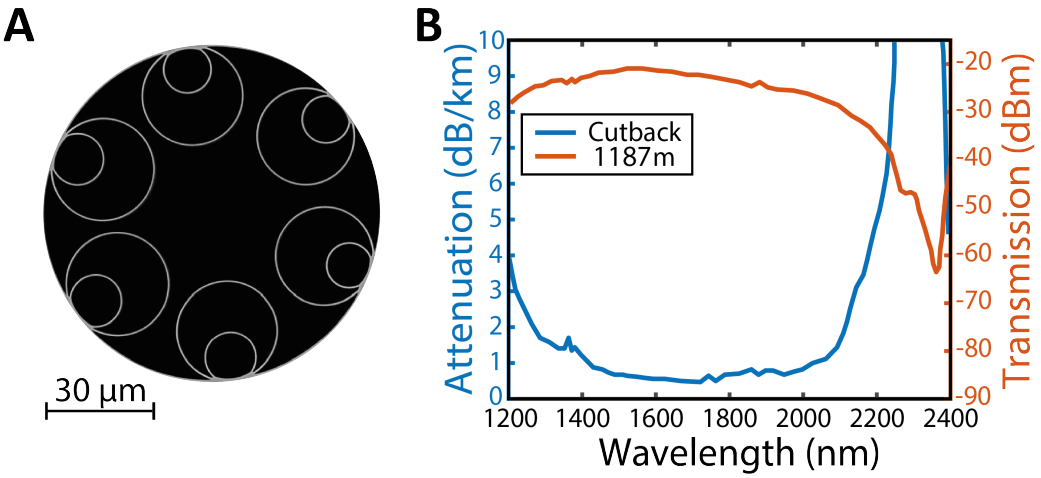

Figure 4.2: NANF properties provided by the manufacturer. (A) Scanning electron micrograph (SEM) cross-section of the structure of the NANF being tested. (B) Test data provided detailing guidelines for the attenuation and transmission properties over a range of wavelengths. This test data provides a reference for expected properties for our experimental tests.

From the data provided, the attenuation loss for relevant wavelengths was 1.39 dB/km at 2000 nm and 0.62 dB/km at 1560 nm. The performance of the NANF was performed by testing with a Thulium-Doped fibre laser source (Thorlabs, LFL2000) with emission wavelength of 2000 $\pm$ 2 nm and output power $\geq$ 25 mW. The benchtop Fabry-Perot fibre laser exhibited a narrow spectral width at the target wavelength and a manually controllable output power making it an ideal candidate for the characterisation of the NANF. The fibre laser output was accessible from a single-mode fibre output which was projected into free space using a single-mode fibre (SM2000) connected to a reflective collimator coupler. The resulting output produced a collimated beam with diameter at $1/e^2$ of 3.3 mm. As the numerical aperture (NA) of the NANF is very low $<$ 0.1 and the alignment at 2 µm challenging, significant control of mounting the fibre was required. Prior to mounting, a small portion of the outer coating of the NANF was stripped and the fibre end cleaved and inspected. This end of the NANF was mounted in the focus of the coupling optics using a tapered V-groove fibre holder (HFV002) fixed on a 6-axis Nanomax stage (Melles Griot HS17MAX600) to aid with alignment. Throughout these series of these measurements, a single-mode fibre laser operating at 1560 nm was used to help with alignment and coupling into the NANF.

The mode field diameter (MFD) of the NANF can be approximated by

$$\text{MFD} \approx 0.75 \times \text{Core Diameter}\,, \tag{4.1}$$

which provides a diameter of 27.2 μm required to couple into the NANF mode. An appropriate CaF_2 bi-convex lens with high transmission at 2000 nm was chosen as the input coupling lens in order to match the fundamental mode field diameter of the NANF fibre and minimise coupling to higher order spatial modes. Both input and output lenses were mounted on small translational stages in order to aid with coupling and collimating at output. An InGaAs IR Xenics camera was an additional tool used to ensure corrrect alignment of optics and irises. At the ouput of the NANF, the collimated beam was directed onto an InGaAs photodetector (Thorlabs, PDA10DT). The photodetector was connected to a lock-in amplifier (Stanford Research, SR8300) which recorded the output voltage across the detector. A mechanical chopper (Thorlabs, MC2000B) was used directly at laser output to modulate the light with a frequency of 877 Hz and this frequency was used as a reference for the lock-in amplifier. The chopping frequency was chosen to be a value which was away from natural sources of noise and chopper wheels appropriate for the laser beam size. The output lock-in voltage was recorded for numerous ND filters and compared to the input readings with the same input power. For the 2000 nm field, the coupling losses were conservatively estimated to be $\sim$ 3 dB. In order to record the attenuation of

the fibre, the power output of the throughput for the entire 1.1 km fibre was recorded before a 1 m length section of the fibre was cleaved. Without altering the input coupling, the 1 m transmission was measured allowing a comparative attenuation to be estimated. For the target wavelength of 2000 nm, the measured attenuation was 3.8 dB/km which was larger than the quoted loss given by the manufacturer of 1.39 dB/km. The measured attenuation of the alignment laser was 0.52 dB/km at 1560 nm which correlated with the manufacturer's guidelines of 0.62 dB/km. The optical attenuation of the NANF was measured using the cutback technique. Once recording transmission through the 1.1 km NANF length, the input NANF end and launching conditions were unaltered however the output end is cleaved to a shorter length in order to calculate the fibre loss presented. As this was our only NANF sample and in order to preserve the length of the NANF, this cleaving was only performed once for both 1560 nm and 2000 nm to give estimation of fibre loss. In ideal conditions, different cleaves with varying lengths of the NANF would provide a more accurate transmission loss and estimate the uncertainty associated with different cleaves. When considering the long duration between the manufacturing testing and the measurements performed in this and ongoing work, a drop in the performance of the NANF is to be expected. The next step was to quantify the polarisation properties of the NANF with this source.

4.2.2 Polarisation extinction ratio of NANF at 2 μm

The measurement of the polarisation coupling of the NANF was performed by performing a crossed-polariser transmission measurement using free space polarisation optics. Figure 4.3 shows the experimental setup where the fibre laser was projected into free-space using a fibre coupler and a single-mode fibre (SMF) suitable for the wavelength.

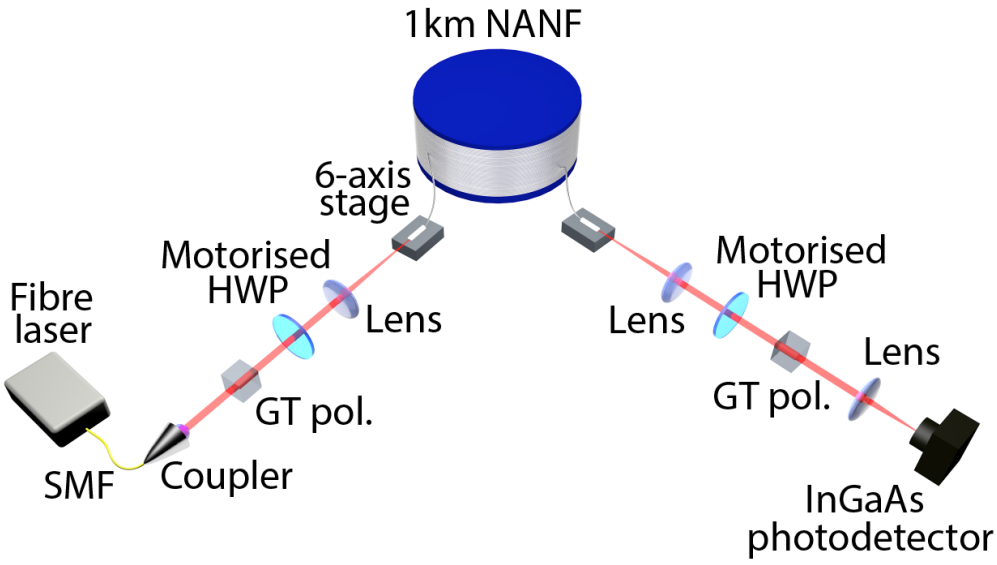

Figure 4.3: Experimental setup for the measuring the polarisation extinction ratio of NANF at 2 μm. The polarisation is set by Glan-Taylor polariser (GT pol.) and motorised half-wave plate (HWP) controls the polarisation entering 1 km long NANF fibre mounted on a 6-axis stage for coupling control. The NANF output is analysed using an identical HWP/GT pair before focusing into an InGaAs photodetector.

The polarisation of the fibre laser output was set using a Glan-Taylor calcite polariser (Thorlabs, GT10) with quoted high extinction of 100,000:1. The polarisation state entering and exiting the NANF fibre is controlled using achromatic half wave plates (B Halle, RAC 6.2.15) mounted on motorised rotational stages (Thorlabs, PRM1Z8). The polarisation optics were required to be characterised to define the limit of measurable polarisation extinction. In order to measure this, the polarisation extinction measurement was performed in free space without coupling to the fibre. The extinction ratio measurable with these optics was characterised first which went beyond the quoted manufacturer values with extinction of approaching 55 dB measured with specific polarisations. These measurements were performed by setting the polarisation with a Glan-Taylor polariser and rotating a half-plate to change the polarisation whilst recording the extinction of power output from the throughput of an identically orientated Glan-Taylor polariser set at the output of another broadband half-wave plate. The power output was once again measured using an InGaAs photodetector (Thorlabs, PDA10DT) connected to a lock-in amplifier (Stanford Research, SR8300). As before, an optical chopper was used (not included in Figure 4.3) and the chopping frequency was used as a reference for the lock-in detection of the output voltage of the photodetector. A code was written to automate the measurement acquisition and to control the motorised HWP's. The input polarisation was set by the input HWP orientation before rotating through a range of 90 degrees with the output HWP to obtain a response curve (see Figure 4.4)

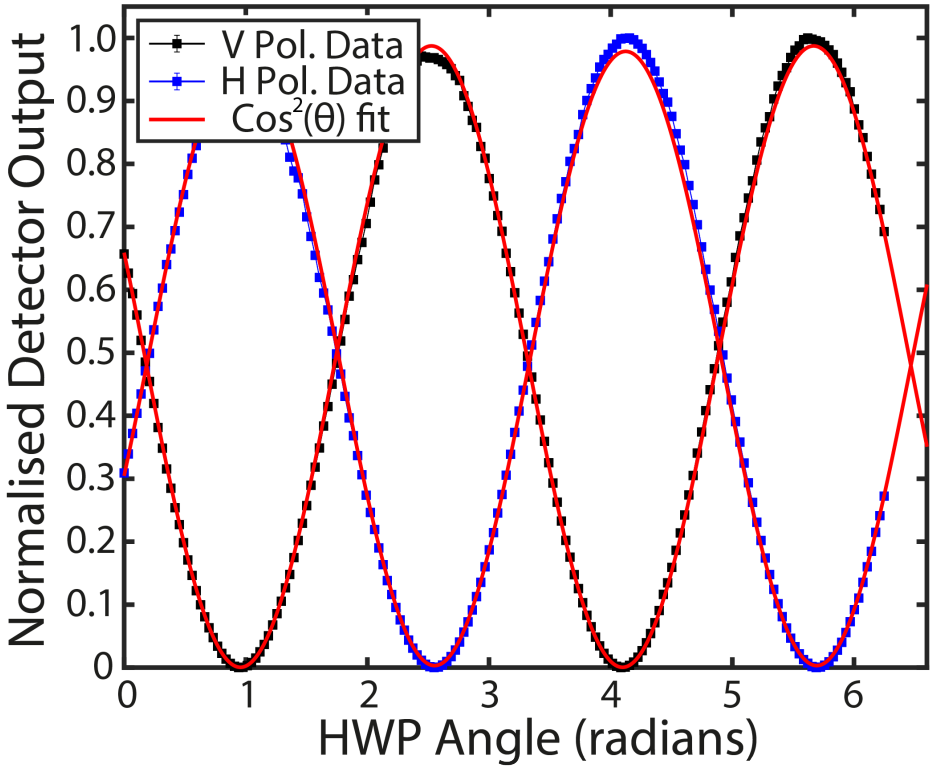

Figure 4.4: Sample of extinction of linear polarisations V (black) and H (blue). The measured voltage output for each polarisation was fitted with a $\cos^2(\theta)$ fit (red) as discussed in text.

corresponding to each input angle. Each data point was averaged over 3 seconds to provide an error which was used to estimate the error associated with final measurement. To measure the polarisation extinction ratio (PER), the raw lock-in voltage data was normalised and fitted with a $\cos^2(\theta)$ function as expected from relevant literature [108].

The PER was calculated using the following

$$PER = -10 \times \log_{10}\left(\frac{S_{max}}{S_{min}}\right), \tag{4.2}$$

where S_{max} and S_{min} correspond to the maximum and minimum measured lock-in signal respectively.

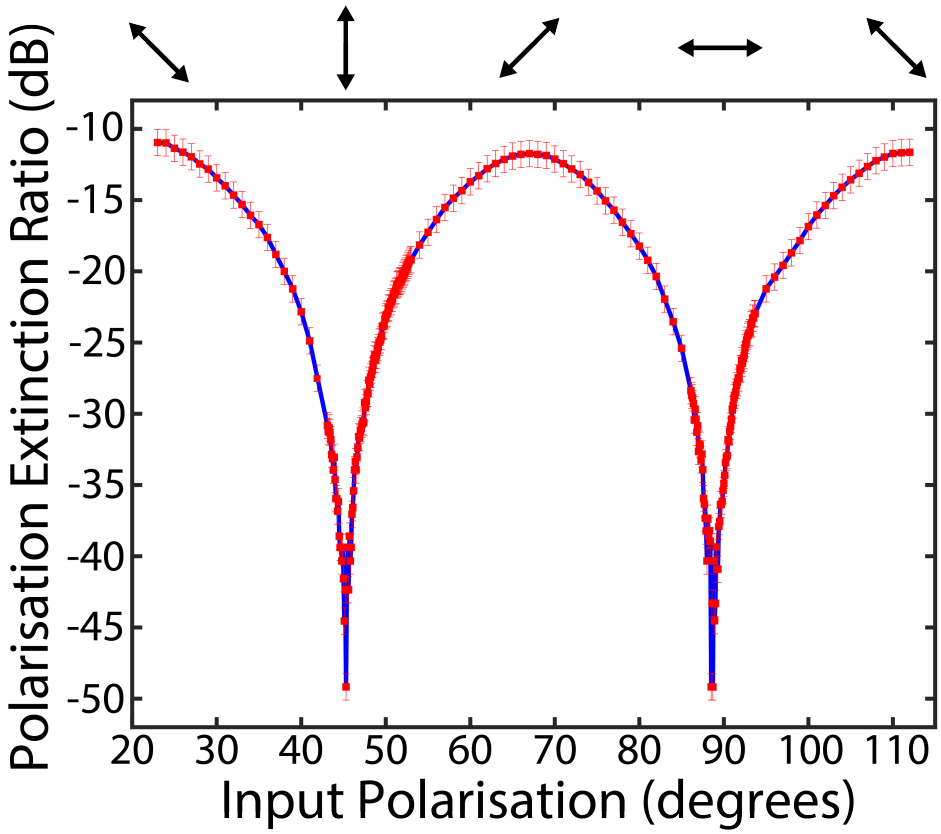

Figure 4.5: The polarisation extinction ratio (PER) measured across 1 km of NANF for a range of input polarisations with a CW fibre laser at 2 μm. Extinction data (red) plotted with blue line used as a guide to the eye. The input polarisation orientation is indicated by arrows above.

The measured PER for a range of input polarisations is shown in Figure 4.5. The high extinction ratio for H and V input polarisations ($\approx$ 50 dB) approach the limit of the measuring capabilities of the optics (55 dB). At intermediate polarisations, the extinction doesn't get worse than 12 dB which demonstrates the NANF fibre does preserve the polarisation of the field as documented in recent literature at telecom wavelengths [109]. This demonstration of the preservation of the polarisation state and low attenuation at the target wavelength of 2 μm is a step towards the aim of this project. However, in order to demonstrate that it is possible to propagate quantum states of light (polarisation entangled or time-bin) via hollow core fibres, further characterisation of the pulsed properties of the fibre are required. Before formulating a measurement with a pulsed SPDC source, characterisation of suitable single-photon detectors was required.

4.3 SNSPD's efficiency characterisation at 2 μm

The SNSPD's used for this efficiency measurement was a Single Quantum multi-channel closed-cycle system for which two of these channels (detector 3 and 4) are designed to operate at a wavelength of 1310 nm. These commercial SNSPD's were characterised at the wavelength of interest using the same Tm-doped fiber laser (Thorlabs, LFL2000) with a single-mode fibre output used before with an emission wavelength of 2000 ± 2 nm. Figure 4.6 shows the experimental setup used to characterise the SNSPD's. The 25.5 mW laser output coupled to SM2000 was guided into a module containing multiple electronic variable optical attenuators (Thorlabs, V2000) connected to a box circuit consisting of a voltage divider and potentiometer to control the voltage across each attenuator. Each attenuator was able to provide attenuation of up to around 28 dB when a maximum driving voltage of 5 V was supplied. The module output was coupled via SMF 28 fibre patch into a manual fibre polarisation controller before being directed to the cryostat to allow careful calibration of the power output. An extended InGaAs photodiode power meter with nW resolution was used to performed the power measurements throughout. The stability of the pump laser was observed before any measurement took place. Given the laser output, in order to achieve an attenuated power output of 100 fW corresponding to 1 MHz photon counts,

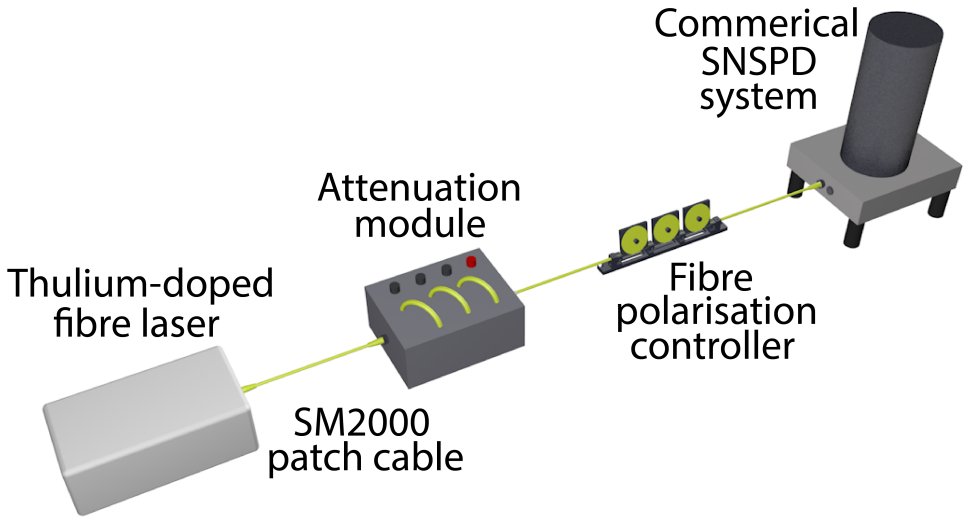

Figure 4.6: Experimental scheme depicting the characterisation of the efficiency of a commercial SNSPD system using a 2 μm Thulium-doped fibre laser. An attenuation module consisting of multiple electronic variable optical attenuators (providing up to 28 dB attenuation each) was used alongside a fibre polarisation controller to measure the efficiency of two SNSPD's at the target wavelength of 2 μm.

the calculated required attenuation across all components was 114 dB. The calibrated attenuation including SMF 28 coupling measured was 121.4 dB. The attenuated output was directed into detector 3 and 4 where the count rate for each was recorded. Figure 4.7 shows the measured efficiencies of detectors 3 and 4 as a function of the bias across the SNSPD's. The measured efficiency using recorded count rate and estimated count rate from calibration was **10.8 ± 0.7%** for detector 3 and **9.2 ± 0.6%** for detector 4 at 2 μm. These values are in line with expected efficiency values for these detectors

which are designed for a wavelength of 1310 nm with efficiency $> 90\%$. These commercial detectors demonstrated higher performance than the SNSPD's used in work conducted in the previous chapter.

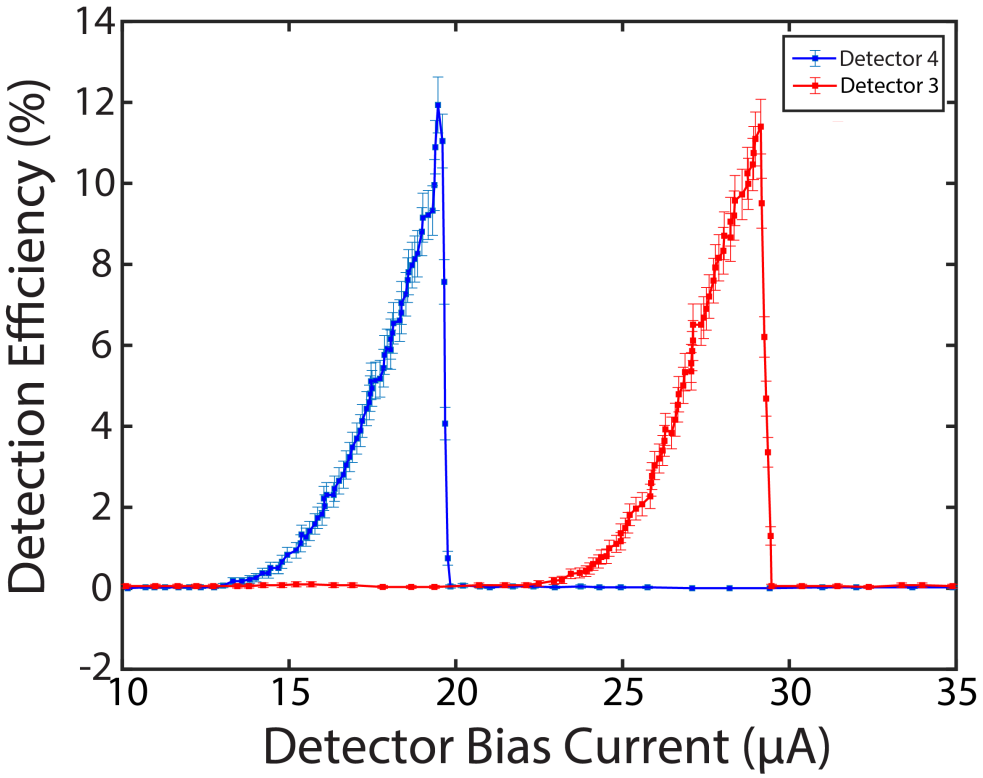

Figure 4.7: The measured detection efficiencies of Detectors 3 (red) and 4 (blue) over a range of detector bias currents with background reduction. Blue and red lines used as a guide to the eye. Removal of dark counts data reduces but does not fully remove the peaks shown when approaching the critical current for each detector.

4.4 Discussion and future work

This chapter has demonstrated ongoing work onto the feasibility of using hollow core fibres for propagating quantum states of light in the mid-infrared. Specifically, a 6 nested tube NANF design was tested to experimentally confirm the attenuation loss provided by the manufacturer and collaborators. The attenuation properties through 1 km of NANF was tested first at 1560 nm (for which alignment and imaging was considerably easier). The measured attenuation with the CW fibre laser at 1560 nm was 0.52 dB/km which correlated with the manufacturers guideline attenuation at this wavelength of 0.62 dB/km. Recent breakthrough publications using NANF have demonstrated record low attenuation in telecom wavelengths of 0.28 $\pm$ 0.04 dB/km [99]. Replacing the laser source with the 2000 nm fibre source, the measured attenuation of 3.8 dB/km was recorded which is higher than the manufacturer guideline attenuation of 1.39 dB/km.

Recent work has demonstrated the exceptional polarisation purity in both ARF and NANF designs of single-mode hollow core fibre at telecom wavelengths [109]. In this work, the polarisation properties of a NANF was performed with a CW source at 2 μm. High extinction was observed at horizontal and vertical polarisations close to the measurable limits set by the equipment. At diagonal input polarisations, the extinction was reduced to 12 dB which demonstrates the potential to use NANF for propagating quantum states of light. Recently published work has proposed utilising

NANF designs for quantum communications, specifically quantum key distribution [107]. The low attenuation properties combined with the ability to transmit low-latency signals over varying spectral ranges could be useful for fibre based QKD applications. The advantage in QKD performance using NANF designs over SMF has already been demonstrated [110]. The future of HCF and NANF technology is bright.

Continuation of this work will involve characterising the properties of the NANF using a pulsed source. Using the same pulsed laser system utilised in Chapter 3, an identical Type-0 SPDC source at 2090 nm will be characterised and coupled into the 1 km long NANF. Work in progress currently involves characterisation of the SPDC source which is very large in diameter and the NANF coupling conditions requires a spot size of around 30 μm. Being incapable of imaging the SPDC due to the unavailability of a camera operating at this wavelength means a knife-edge measurement and demagnification will be required to couple into the NANF. Having characterised twin SNSPD's with higher efficiency at 2 μm than those utilised in Chapter 3 further optimises the detection capabilities for future quantum measurements. The next immediate stage will involve the measurement of the fibre dispersion using the characterised SNSPD's. Using three different bandpass filters and measuring the time-resolved signal on the SNSPD's before propagation into the fibre and after propagation into the fibre, it should be possible to extract the fibre dispersion. Once coupled, the dispersion and polarisation extinction through 1 km of NANF can be characterised. To the knowledge of

this author, the propogation of polarisation entangled photon pairs through a NANF design hollow-core fibre has yet to be demonstrated at 2 μm which is the goal of this ongoing work.

Chapter 5

Single-cycle THz-field electro-optic sampling with single-photon detectors

5.1 Introduction and motivation behind THz sensing

Terahertz (THz) radiation is traditionally defined as a section of the electromagnetic spectrum which lies between the 0.1 - 30 THz frequency range and in recent times has been identified as one of ten emerging technologies that will change the world [111]. Alternatively defined as *submillimetre radiation* and existing between microwave and infrared wavelengths, this spectral re-

gion is commonly described as the "THz gap" due to limitations in detection sensitivity and scarcity of practical high performance sources in comparison with nearby spectral ranges. Having been traditionally studied in cosmological research, recent breakthroughs in photonics has enabled THz technologies which have garnered significant interest in countless fields such as such as imaging, medicine, communications etc. which can be attributed to the distinctive properties of THz waves [112–115]. THz radiation has the ability to identify at the molecular level individual spectral "fingerprints" of substances such as drugs using sophisticated spectroscopic techniques which has particular interest in the pharmaceutical industry [116]. The transparency of non-ionising THz radiation to numerous everyday materials enables applications such as the non-disruptive probing of pharmaceutical samples to non-invasive screening for concealed explosives in real world security scenarios [117–119]. The far-reaching impact of THz imaging can be found in art and cultural conservation efforts where non-invasive imaging of historical architecture and authentication of paintings can help detect art fraud [120,121]. In addition, wireless and on-chip communication networks have identified the THz band as a promising candidate to help meet bandwidth requirements of exponentially increasing data traffic demands [122, 123].

However, the further advancement and widespread adoption of future THz technology relies heavily upon fast and efficient detection. Many off-the-shelf THz detectors utilise pyroelectrics and bolometric techniques which are typically very slow and don't measure coherent features of the field. Research

into superconducting niobium bolometers demonstrate very high sensitivity and low noise performance however they operate at temperatures of 2-7 K therefore require cryogenic environments [124,125]. Many of the above applications of THz radiation rely on the field of photonics to detect the coherent properties of a THz pulse. Most of the spectroscopic applications in the THz regime rely on a powerful technique called time-domain spectroscopy (TDS) capable of measuring the electric field (amplitude and phase) of the THz field. This uses ultrafast laser pulses to generate and subsequently measure the THz field in the time-domain exploiting non-linear optical processes. A traditional THz-TDS system approach is based on electro-optic sampling (EOS), a form of time-resolved polarimetry that takes advantage of the Pockels effect in $\chi^{(2)}$ non-linear crystals inducing a phase shift proportional to the THz field strength [126–129]. The well-established pump and probe system enables the reconstruction of the THz pulse in the time domain so long as the probe pulse is shorter than the THz electric field oscillation period. The noise associated with a THz-TDS measurement is related to the amplitude noise of the THz signal itself and the shot-noise of the optical probe used for sampling the THz field [130]. Amplitude noise can be reduced using clever experimental strategies however the shot-noise of the probe is fundamentally a more difficult problem. Recent research has targeted optimising the detection method [131]. Our proposal was to use quantum states to enhance THz detection using a polarimetric measurement using single-photon detectors. Proposals to enhance THz detection sensitiv-

ity using non-classical probes have also been reported in recent work [132]. The feasibility of using NOON or Fock ultrashort probes for polarimetric measurements have been noted [133, 134] and demonstrates the significant potential using non-classical states as a probe could have on techniques such as THz-TDS. In the work demonstrated in this chapter, a first step in the direction of quantum-enhanced THz sensing is made by demonstrating that THz EOS can be performed using a squeezed vacuum probe generated by SPDC and measured with single-photon detectors. By developing a lock-in style polarimetric scheme, a shot-noise limited balanced detection was performed using single-photon detectors to measure the optical phase shift from THz-induced birefringence [135]. Instead of using a weak coherent probe pulse, squeezed vacuum from SPDC was used as it is a widely employed resource underpinning quantum-enhanced metrology. Although this work details no quantum enhancement in THz detection at this stage, the foundations have been laid for employing non-classical resources such as NOON states to enhance the detection sensitivity.

5.2 Theory of electro-optic detection

Electro-optic detection is a technique which utilises a 2^{nd} order non-linear process in which the presence of an applied electric field results in an change in the refractive properties of a material, typically a non-linear crystal [1]. It exploits the linear electro-optic effect (also named the Pockels effect) and only occurs in non-centrosymmetric materials depending heavily on the specific properties of the second-order non-linear susceptibility $\chi^{(2)}$. The linearity between the change in the refractive properties with the magnitude of the electric field is not observed in centrosymmetric materials. The higher order dependence on electric field strength is known as the Kerr electro-optic effect where the refractive shift scales quadratically. The crystal structure forms an important factor in the birefringence of electro-optic media. The residual birefringence exhibited by a crystal (with no electric field exposure) can be written in terms of its *index ellipsoid* as

$$\left(\frac{1}{n_1^2}\right)x^2 + \left(\frac{1}{n_2^2}\right)y^2 + \left(\frac{1}{n_3^2}\right)z^2 = 1\,, \tag{5.1}$$

where n corresponds to the refractive indexes of each of the principal axes x, y and z as detailed in Figure 5.1 [136].

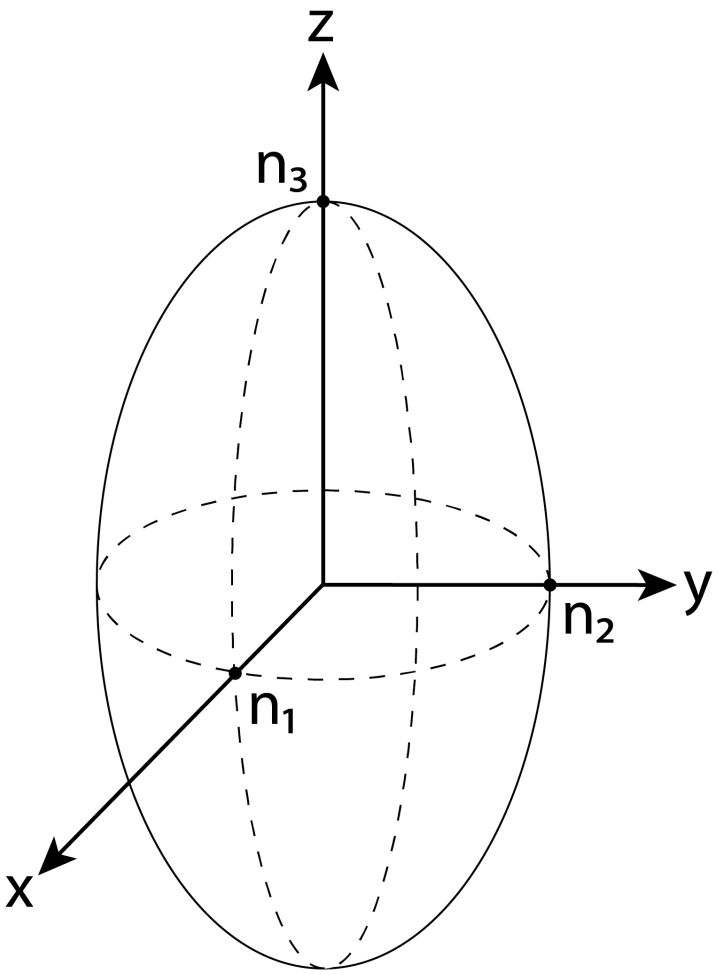

Figure 5.1: Schematic showing the index ellipsoid defined using the principal axes x, y and z. The refractive indices n_1, n_2 and n_3 corresponding to each of the principal axes are also shown.

When an electric field is present, the transformation of the index ellipsoid by the electro-optic effect can be expressed in Cartesian coordinates by

$$\left(\frac{1}{n_1^2}\right)x^2 + \left(\frac{1}{n_2^2}\right)y^2 + \left(\frac{1}{n_3^2}\right)z^2 + 2\left(\frac{1}{n_4^2}\right)yz + 2\left(\frac{1}{n_5^2}\right)xz + 2\left(\frac{1}{n_6^2}\right)xy = 1\,, \tag{5.2}$$

where choosing x, y and z as principal axes reduces the remaining terms to zero [137]. This expression can be reduced to define the deformation of the index ellipsoid by introducing the electro-optic tensor r_{ij} defined by

$$\Delta\left(\frac{1}{n_i^2}\right) = \sum_{j=1}^{3} r_{ij}E_j\,, \tag{5.3}$$

where i= 1, 2, ..., 6 and $E_{1,2,3}$ denotes components of the electric field associated with the principal axes. This relation details the change in the refractive coefficients in the presence of increasing electric field E_j depending on the electro-optic coefficients of the medium. The crystal symmetry structure plays an important role in the form of the electric-optic tensor r_{ij}.

Consider the cubic crystal Gallium Arsenide (GaAs) which belongs to the $\overline{4}$3m symmetry group where the electro-optic tensor takes the form

$$r_{ij} = \begin{pmatrix} 0 & 0 & 0 \\ 0 & 0 & 0 \\ 0 & 0 & 0 \\ r_{41} & 0 & 0 \\ 0 & r_{52} & 0 \\ 0 & 0 & r_{63} \end{pmatrix}, \tag{5.4}$$

where the only electro-optic coefficients which are non-zero and equivalent are r_{41}, r_{52} and r_{63}. The electro-optic coefficient r_{41} for GaAs is 1.5 pm/V and refractive index n of 3.38 at 1560 nm. For the case utilised in these series of measurements, a crystallographic cut of $\langle 110 \rangle$ for GaAs is considered, a typical choice for maximising the electro-optic coefficients for electro-optic detection of THz radiation. A critical detail well-documented in literature of measuring THz radiation using an optical probe incident on an electro-optic crystal is the optimal configuration of probe and THz field orientations with respect to the crystal axis [138]. This non-trivial operation often involves setting the polarisation orientation of the probe field and THz field and rotating the crystal around the z axis $\langle 001 \rangle$ to optimise the THz electric-field measured via balanced detection. A schematic of the experimental setup is shown in Figure 5.7 which details the orientation of the axes in our experimental setup with the probe polarisation being parallel to the z axis. In order

to achieve this, a coordinate transformation is required to align the ellipsoid axes with a new coordinate system. The coordinate rotation which appeals to a $\langle 110 \rangle$ cut crystal tends to be a $\frac{\pi}{4}$ rotation around the z axis $\langle 001 \rangle$ [136]. The outcome of this transformation identifies the best configuration to optimise the induced rotation of the probe polarisation from the THz field. If the orientation of the probe is parallel to the z axis, the THz field must be orthogonal to the probe for maximum phase rotation of the probe and to be detected using an ellipsometric method typically employed in these measurements. In the presence of no THz field, the linear polarisation of the probe passes unaffected through the electro-optic crystal and transforms into a circularly polarised beam after passing through the QWP. When the external THz field is present, an elliptical component of the polarisation is imparted which can be detected by differential measurement between two balanced photodetectors [139]. The phase change can be described by the ratio of the differential measurement ΔI between the intensity of the probe I_p during the interaction by the expression

$$\Delta\Phi = \frac{\Delta I}{I_p} \approx \frac{2\pi r_{41} n^3 L E_{THz}}{\lambda}\,, \tag{5.5}$$

where L is the thickness of the interaction crystal [138,140]. For these type of measurements, the differential signal ΔI is usually set to zero when no external field is applied using the QWP. The main contributing factor to inducing a large phase onto the probe field is maximising the electric field strength

E_{THz} assuming the optimal crystal orientation is used. With the resources available, the peak THz field strength obtained using a GaAs semiconductor-based antenna was characterised and the estimated phase induced on a classical probe verified using THz time-domain spectroscopy.

5.3 THz generation and detection

5.3.1 THz generation using photoconductive antenna

In this experiment, THz generation was performed using an ultrashort pulse of laser radiation incident on a photoconductive antenna (PCA) to produce a high THz electric field pulsed amplitude over a large bandwidth. The generation of THz pulses was conducted by photo-exciting the PCA (Tera-SED, Laser Quantum) with a femtosecond pulsed laser system with a repetition rate of 80 MHz and pulse duration of 100 fs. Throughout these series of measurements, the laser system used was a mode-locked tunable laser (Coherent Discovery) with average power of up to 1.8 W at carrier wavelength of 780 nm. To control the output power, a broadband variable attenuator was mounted directly after the pumped laser source which uses the combination of a half-wave plate and two thin film polarisers to control the power output in a specific polarisation. Using the power controller, up to 600 mW of power at 780 nm was available to photo-excite the THz antenna. The Tera-SED PCA used consists of a planar $3 \times 3\,\mathrm{mm}^2$ GaAs substrate with an interdigitated metal-semiconductor-metal (MSM) electrode structure which is connected and modulated by an external bias field. Figure 5.2 details the basic operation and key structures of the PCA. The incidence of focused femtosecond laser pulses on the GaAs semiconductor excites charge carriers which are subsequently accelerated by the bias voltage provided. This

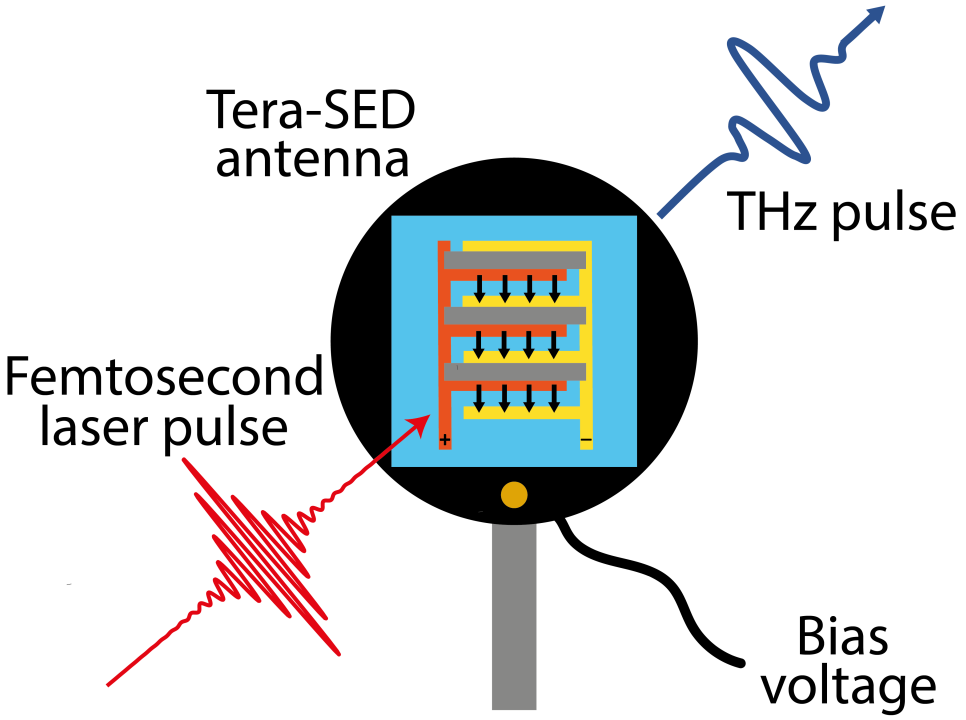

Figure 5.2: Schematic showing the operation of the THz photoconductive antenna. Generation of THz radiation occurs when femtosecond laser pulses (red) are incident upon the active area of the photoconductive antenna (black) biased using an external voltage supply via electrical connection (black cable). The antenna active area consists of an interdigitated MSM electrode structure (orange and yellow) processed onto a GaAs substrate (blue). Opaque metallisation layer (grey rectangles) ensures optical excitation occurs in GaAs regions which share the same electric field direction (black arrows). THz radiation (dark blue) emitted from the antenna thus interferes constructively in the far-field.

bias voltage induces an electric field between the electrodes and the GaAs substrate is appropriate due to its high breakdown field and high carrier mo-

bility [141]. The addition of an opaque metallisation layer (grey rectangles) ensures optical excitation only occurs in GaAs regions which share the same electric field direction. The accelerating charges radiate THz frequencies, however the performance of the antenna is dependent on specific conditions considering the damage threshold of the device. The bias voltage must be kept below 50V and if DC biasing, an optical chopper must be used to modulate the laser input. The PCA has peak emission frequency at 1.5 THz and requires optical excitation at the wavelength range 700-850 nm, where our laser source lies. The excitation condition was optimised by recording the THz power with a pyroelectric detector (THZ5I-BL-BNC-D0, Gentec EO). Collimation and focusing of the emitted THz beam into the pyroelectric detector was performed using two 50 mm focal length parabolic mirrors. A filter is placed over the aperture of the pyroelectric detector to eliminate any pump scattering from the antenna. This is typically a piece of paper or thin plastic which the THz radiation can pass through. This detector was connected to a lock-in amplifier (Stanford Research, SR8300) used to extract particularly weak signals using phase-sensitive detection. The pyroelectric detector is integrated with a low noise current mode amplifier and required a 5 Hz chopping frequency to optimise voltage output. The THz generated by the PCA was optimised by varying the geometry of the focused excitation beam incident on the PCA as noted in relevant literature [142, 143]. The pump beam diameter was altered using a long focal length lens mounted on a translational stage and measured with a beam profiler (Gentec).

In Figure 5.3, the normalised THz power output of the pyroelectric detector as a function of the diameter of the spot size at FWHM of the focused pump is shown. The most effective spot size for excitation of the GaAs substrate was measured to be 297 µm which correlated closely with quoted values in the PCA manual and literature [143].

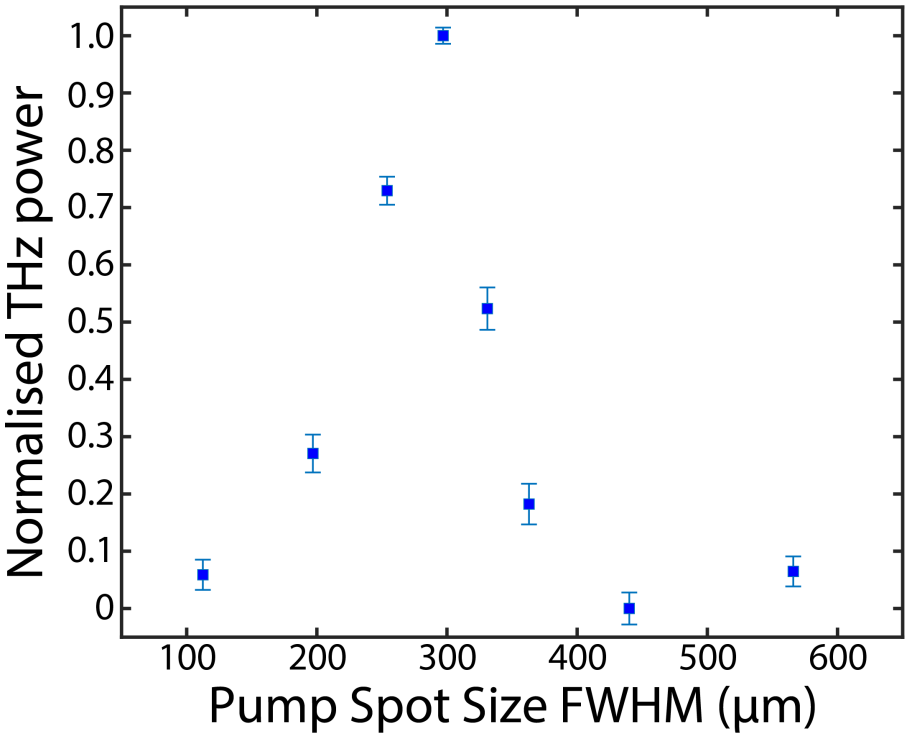

Figure 5.3: Normalised THz power output of the pyroelectric detector versus the FWHM diameter of the spot size incident on the PCA.

At optimised conditions, the peak THz pulse energy measured with the pyroelectric detector was U $\simeq$ 1.25 fJ. The dimensions of the THz beam were also measured using a knife-edge approach, shown in Figure 5.4.

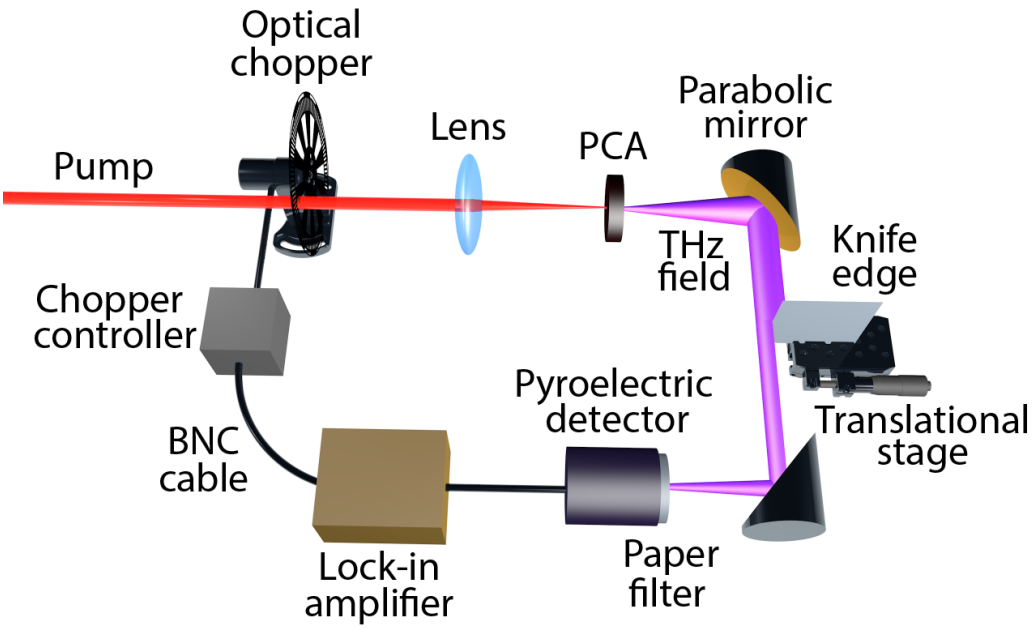

Figure 5.4: Experimental setup for knife-edge measurement of the THz beam diameter in the far-field. The pump beam (red) is modulated by an optical chopper at a frequency corresponding to operation of the pyroelectric detector used for THz detection. The THz radiation emitted by the PCA under incidence of the focused pump is interrupted incrementally by a knife-edge mounted on a manual stage. Lock-in detection is performed using the chopping frequency as a reference and the output detector voltage as signal as the knife-edge interrupts the beam to determine the THz beam properties.

Using a sharp edge mounted on a translational stage, the THz beam was interrupted by the blade and incrementally removed allowing transmission of the beam. The knife edge was scanned across the beam in the far-field until

the voltage output across the detector peaked. The typical curve obtained using the knife edge method used for the fit (red) in Figure 5.5 relies on the standard Gaussian error function (erf) well documented in literature for this method [144]. Since this data was taken in the far-field, the THz beam at the focus of the 50 mm parabolic mirror was estimated by using the beam

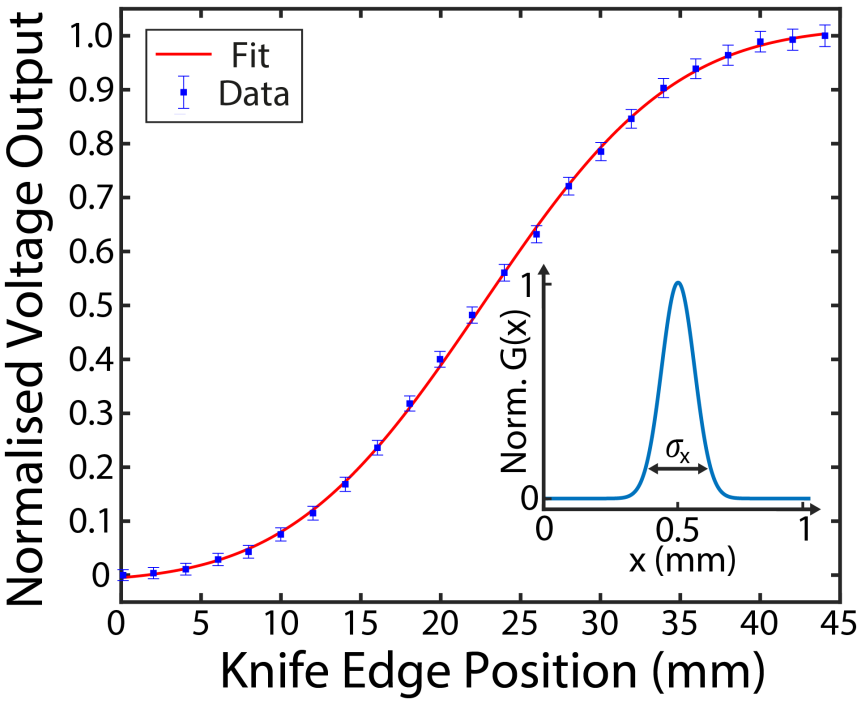

Figure 5.5: Knife-edge measurement of the THz beam diameter in the far-field. The detector output voltage (normalised, blue) recorded as a function of the disruption of the beam. The knife edge starts in a position completely blocking the beam at 0 mm before being incrementally removed and being detected on the pyroelectric detector. The fit (red) is discussed in text. The inset shows the cross-section in the x-direction of the normalised Gaussian profile of THz spot size at the detection focus.

diameter obtained by the knife-edge measurement. The inset of Figure 5.5 shows the estimated Gaussian cross-section G(x) of the THz spot size in the focus in the x-direction, σ_x to be 200 ± 10 μm at the $1/e^2$ condition. Identical results for measurement of the y-direction were also found $\sigma_x = \sigma_y$. The estimation of the THz beam profile G(x,y) was required for calculating the amplitude of the measured THz electric field performed in the next section.

5.3.2 Temporal overlap measurement

In order to fully characterise the nature of the THz radiation in the time-domain, the timing between the THz pulse and the probe is critical. An optical parametric oscillator (OPO) system was used in tandem with the tunable laser system in order to generate a classical probe at 1560 nm to reconstruct the THz pulse using THz-TDS. The OPO (Coherent Levante) was pumped using a fixed 4 W output from the Coherent Discovery laser system to help produce a stable probe signal at 1560 nm. The wavelength of the probe beam was designed a reference to the SPDC probe wavelength used in later measurements in this chapter. The power of the signal probe output was controlled using an optical attentuator and is inserted into the path of the SPDC generation via a dichroic mirror designed with high reflectivity at pump wavelength 780 nm and transmissive at 1560 nm. The spatial overlap between the 780 nm pump and the injected probe was controlled using two mirrors and the coarse temporal overlap was estimated using a fast free-space InGaAs photodiode (Thorlabs, DET08CL/M) connected to an oscilloscope (Rigol, DS4014). The RF output from the laser was used as a trigger. The rough estimation of the temporal overlap between pulses was limited by the temporal resolution of the oscilloscope and the detectors bandwidth. A more precise synchronisation between fields was performed utilising the process of sum-frequency generation (SFG) in a non-linear crystal (as shown in Figure 5.6). As is standard practice in the field, a BBO crystal was mounted on

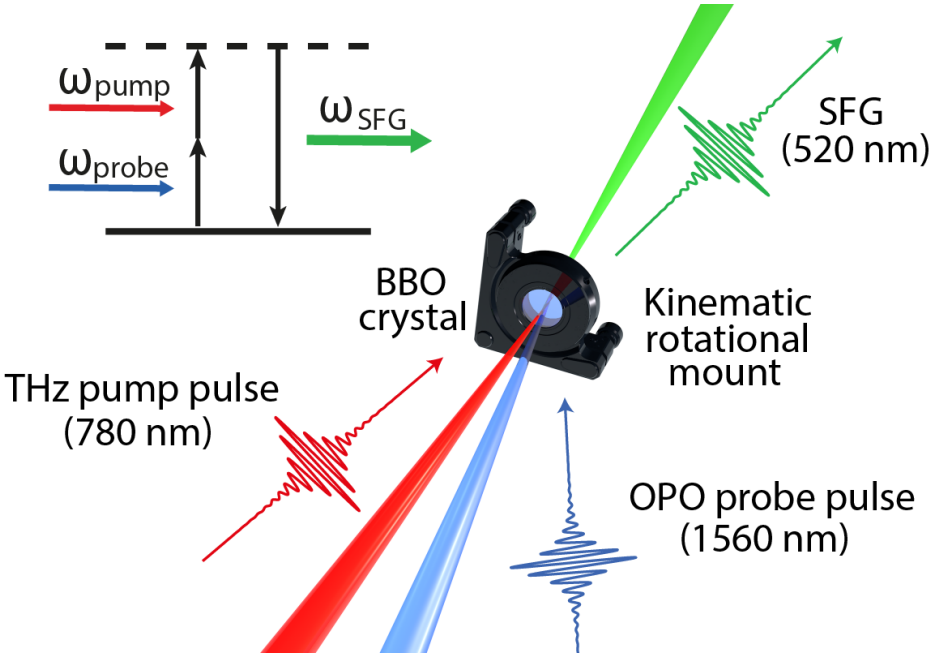

Figure 5.6: Temporal overlap measurement using sum-frequency generation. A BBO crystal mounted in a kinematic rotational mount gives flexibility to achieve the correct crystal tilt angle in order to achieve phase matching between pulsed pump and probe fields. A delay stage in the THz generation path (see Figure 5.13) varies arrival time of the THz pump pulse at 780 nm in relation to the probe pulse at 1560 nm generated by an OPO until SFG at 520 nm is observed in the spatial and temporal overlapped condition. The inset shows the energy diagram for the SFG process where pump and probe photons with frequencies ω_{pump} and ω_{probe} combine to generate a photon with frequency ω_{SFG}.

a rotational stage and placed in the focus of the THz pump field (780 nm) and the OPO probe field (1560 nm). The delay between them was altered until the SFG was observed ($\simeq$ 520 nm) indicating the correct delay between pulses had been found. The GaAs detection crystal was placed in this position on a translational stage along the direction of propagation. It is worth

briefly mentioning that the GaAs wafer used was only $\approx 53\%$ transmissive at the target wavelength when first tested. This wafer was subsequently anti-reflection (AR) coated improving transmission at 1560 nm to 95 % reducing losses considerably.

5.3.3 THz time-domain spectroscopy

In order to fully characterise the nature of the THz radiation which was detected, we used the conventional optoelectronic technique called free-space electro-optic (EO) sampling. This method exploits the Pockels effect whereby the birefringence of an EO material is externally modulated by an applied electric field and the measured waveform becomes the cross-correlation of the incident pump and THz pulses [145]. In THz time-domain spectroscopy (THz-TDS), the electric field of the THz pulse can be reconstructed by coupling it with an ultrafast optical pulse inside an electro-optic medium which in our case is an AR coated GaAs $\langle 110 \rangle$ detection crystal to optimise transmission at 1560 nm. In our setting, the birefringence of the GaAs crystal is modulated by the THz electric field and probed by polarimetry performed with a short optical pulse overlapped to different temporal sections of the THz field [145]. Under incidence of a THz pulse, the refractive index properties of the electro-optic crystal properties change proportional to the magnitude of the electric field of the radiation. The 200 fs probe pulse used for the optical sampling was delivered by an Optical Parametric Oscillator (OPO, Levante IR, Coherent) tuned at 1560 nm at the same wavelengths of the squeezed vacuum source employed for the later single-photon-level measurement. In a THz TDS experimental setup, two pulsed laser outputs (one at 780 nm used to excite the PCA and generate THz pulses and one at 1560 nm from the OPO) traverse equidistant paths in a conventional pump and probe experi-

ment. The relative delay between the probe and the THz pulses is controlled by a delay stage (Newport M-VP-25XL) with a range of up to 25 mm. The residual pump field incident on the PCA is removed with a paper filter before reaching the GaAs detection crystal. The THz and the probe field were cross-polarised and the orientation of the GaAs was optimised to maximize the electro-optical modulation [138].

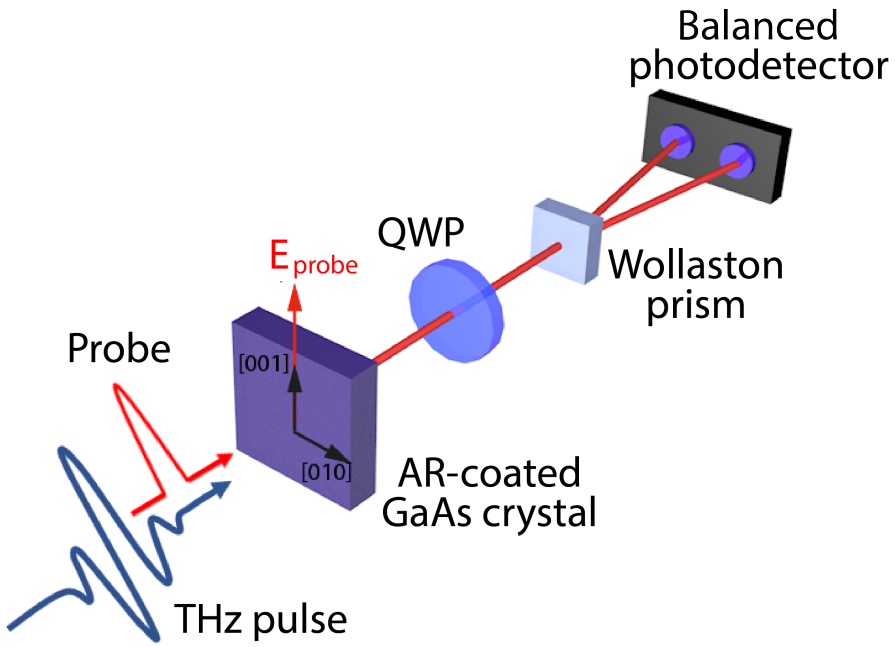

Figure 5.7: Optical detection scheme for electro-optic sampling (EOS) using balanced photodetectors. After interaction inside the AR-coated detection crystal, the probe beam is incident upon a quarter wave plate (QWP), Wollaston prism and balanced photodetectors. The orientation of the QWP controls the ratio of polarisation components incident on the photodetectors to ensure the differential signal $\Delta I = 0$ in the absence of THz field.

The probe pulse and THz field are subsequently focused onto the same region of the GaAs detection crystal. The phase delay induced by the THz field on the probe pulse at the detection crystal is analysed by means of a standard polarimetric arrangement shown in Figure 5.7. This scheme is comprised of a quarter wave ($\lambda/4$) plate, a Wollaston prism (Thorlabs WPA10) and balanced photodiodes (Thorlabs,PDB210C/M). Calibration of the system in absence of the THz radiation is performed using the rotational capabilities of the $\lambda/4$ plate to balance the signal in each detection arm in such a way that no differential signal (ΔI) is produced by the probe injected into the setup in absence of the THz field. The linearly polarised light from the probe beam on passing through the $\lambda/4$ waveplate will be converted to circularly polarised light before being incident on a Wollaston prism which will result in a non-zero output at the balanced photodetectors positioned at small angles with respect to the two separated beams. The balanced detector amplified signal is measured and digitalised by a lock-in amplifier (Stanford Research, SR8300), synchronized to the 10 kHz signal employed to modulate (on-off) the 30 V bias voltage applied to the PCA. Using high lock-in frequencies allows for reducing the impact of the 1/f noise [146–148].

Figure 5.8 (A) shows an example of a THz trace acquired using EOS acquired after purging the experimental enclosure with pure nitrogen gas. Figure 5.8 (B) shows the spectrum obtained by Fourier transform of the time-domain signal shown in Figure 5.8 (A) (red curve). An identical scan in a non-purged environment for comparison (blue curve) shows the strong absorption features of atmospheric water [149, 150].

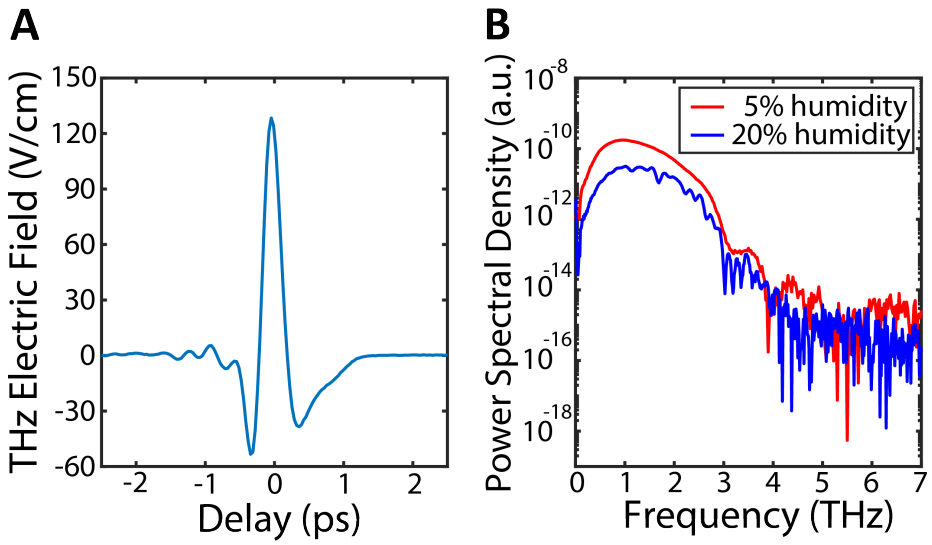

Figure 5.8: (A) THz time-domain spectroscopy using EOS to characterise the THz field trace and spectrum using a classical balanced detection scheme. (B) Power spectrum corresponding to the measurement in A (red curve) and in an un-purged setup (blue curve).

The amplitude $E_{THz}(t)$ of the measured THz electric field trace $E_{tr}(t)$ from THz-TDS was calibrated using

$$E_{THz}(t) = \frac{E_{tr}(t)}{max(|\varepsilon_{tr}(t)|)} \sqrt{\frac{2\,U\eta_0}{\int G(x,y)\,dx\,dy \int \frac{|\varepsilon_{tr}(t)|^2}{max(|\varepsilon_{tr}(t)|^2)}\,dt}}, \tag{5.6}$$

where ε_{tr} is the complex electric field trace and $E_{tr}(t) = \mathbb{R}[\varepsilon_{tr}(t)]$. The THz pulse energy U and THz beam profile $G(x, y)$ were measured in the previous section and η_0 is the vacuum impedance [151]. Using this calibration, the peak THz field amplitude reached $\simeq 130$ V/cm as shown in the Figure 5.8. The maximum phase shift $\Delta\Phi$ that the measured THz field imparts on a probe field inside the detection crystal is

$$\Delta\Phi = \left| \frac{E_{THz} r_{41} n^3 \omega L}{c} \right|, \tag{5.7}$$

where n, r_{41} and L are the GaAs detection crystal refractive index, electro-optical coefficient and thickness [138, 152]. Using the recorded THz field amplitude and considering the refractive index (n = 3.38 at 1560 nm) and thickness (L = 300 μm) of the GaAs crystal used throughout these measurements, an estimated maximum phase shift of $\Delta\Phi \simeq 2.4 \times 10^{-4}\,\pi$ is obtained. Estimation of the maximum phase shift our peak field induces allowed us to estimate the integration time required in order to observe the phase change due to the THz electric field with single-photon detectors.

5.4 Balanced detection scheme for single-photon detectors

An electronic balanced detection scheme was developed to mirror a standard THz-TDS balanced detection performed by photodiodes connected to a lock-in amplifier. As detailed in the previous sections, the modulation frequency of the THz emitting antenna is used as a reference frequency for the lock-in amplifier. We were required to find a similar in-sync gating technique to extract phase information from balanced detection on a photon detection level. Utilising the ps-time tagging resolution of photon counting software, a lock-in style detection scheme was developed capable of extracting phase information from the proposed polarimetric experiment using a down-converted field as the probe. Prior to using this scheme for THz phase detection, balanced detection was performed using a stronger modulation of the SPDC probe using an electro-optic device to test the system.

5.4.1 Time-tagging electronics

For single-photon detection, time tagging electronics are required in order to record with a specified resolution the arrival time of photon events. The Hydraharp 400 module is a multichannel event timing device with time resolution on the ps scale. The time-correlated single-photon counting (TCSPC) module is accessible via USB 3.0 which is capable of processing high data

rates essential for this measurement. The Hydraharp 400 mode most applicable is the time-tagged-time-resolved (TTTR) one which facilitates the recording of photon time of arrival on multiple channels. In our case, ID230 SPAD are used in Geiger mode which allow for reliable photon counting. The ID230 detectors utilise InGaAs/InP avalanche photodiodes, which are thermoelectrically cooled to 183 K providing a low dark count rate and efficiency of up to 25 % at the target wavelength. The output pulse generated by the detectors on photon arrival is a low voltage transistor-transistor logic (LVTTL) pulse with a width of 100 ns accessible via SMA connection. Due to the nature of the output detector pulses, a 20 dB attenuated pulse inverter (PicoQuant SIA 400) was used to help produce pulses compatible with the Hydraharp timing modules. The TTTR data stream produced at this stage simply records which channel, in our case 1 and 2, and the timing of events. In order to help insert a reference throughout our data record, an additional indicator was used to help synchronise which events occurred under external field conditions. A critical feature of the detection scheme we developed was the synchronicity between the modulated field and the count data record. An elegant solution to this problem was to utilise another functionality of the Hydraharp software which was to insert synchronisation information in the form of a marker into the data stream. The Hydraharp has the capability to insert markers into count data by manually inserting a positive 1V TTL input signal into one of four marker inputs found on the front panel SYNC module. This inserts a unique channel code into the data stream to help

discern between real photon event records and markers. These marker pulse functions were generated using a secondary output of the function generator which was phase-locked to the other output (the one used to provide modulation to the system). The rise edge time of the function was set to 50 ns and the peak voltage of +800 mV was directed into the Hydraharp via a BNC to NIM-CAMAC LEMO receptacle attenuated with a 50 Ω load. A LabVIEW code was written in order to record the consistency of the timing of the inserted markers in the photon record. By reading the time tags associated with each marker and the delay between each subsequent marker, the marker accuracy was recorded to exceed $> 94\%$ in regularly sampled datasets.

5.4.2 Phase detection using difference operation

Once a measurement was performed, the Hydraharp software saved the time-correlated single-photon counting data as tagged binary files with the .ptu file extension. In T2 mode, every input is treated as functionally identical with the record essentially consisting of event times with respect to the time elapsed from the start of the measurement. Since converting the .ptu file from binary-to-ASCII is a slow and inefficient detour, a robust data analysis routine was developed to interpret the 32-bit record using arrays in the PC memory. The record consists of three inputs: marker timing information (M) and event timing data from Detector 1 (D1) and Detector 2 (D2).

In Figure 5.9, a sample of event data stream with respect to time, t, is shown. The data analysis code is triggered by the arrival of a marker

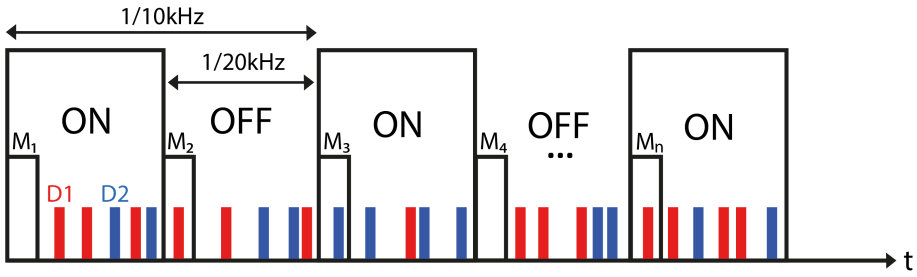

Figure 5.9: Sample depiction of the TTTR data stream using photon counting software. A difference measurement was performed between counts in detectors D1 and D2 using markers M_n every half cycle of the 10kHz antenna modulation

inserted at a frequency of 20 kHz i.e. every half cycle of the modulation function. The 10 kHz square waveform function used provides an ON-OFF modulation with markers introduced every 20 kHz to distinguish between active and inactive fields. The significance of the modulation frequency on the dynamic range (DR) for this measurement was numerically investigated as detailed in Appendix C. The phase information was recorded by performing the following difference operation between ON-OFF modulation period n of the photon record

$$\Delta\Phi_n = \underbrace{\frac{\Delta N_n}{\Sigma N_1 + \Sigma N_2}}_{\text{ON}} - \underbrace{\frac{\Delta N_n}{\Sigma N_1 + \Sigma N_2}}_{\text{OFF}}, \tag{5.8}$$

where N_1 and N_2 are the photon counts incident on Detector 1 and Detector 2.

The analysis code processed the record over the full duration of the measurement to provide an array of $\Delta\Phi$ values. Due to the substantial photon rates used in these measurements, the resulting measurement file sizes were inevitably too large to run these measurements for longer than 15 minutes. The code was streamlined to output an array of $\Delta\Phi$ values and disregard irrelevant or previous analysed photon/marker events. For a sanity check, the sum of phase events was checked to be proportional to the number of markers detected, i.e. half cycle of modulation. The phase information obtained from each measurement was analysed by assuming Poissonian statistics in the input field. The difference operation between two Poissonian fields was implemented using the Skellam distribution [153]. For two Poissonian distributions with means λ_1 and λ_2, the Skellam distribution is defined by

$$P(k) = e^{-(\lambda_1+\lambda_2)}\left(\sqrt{\frac{\lambda_1}{\lambda_2}}\right)^k B_k\left(2\sqrt{\lambda_1\lambda_2}\right), \tag{5.9}$$

where $B_k\left(2\sqrt{\lambda_1\lambda_2}\right)$ is the modified Bessel function of the first kind with index k [154]. Fitting of the Skellam function to the measured $\Delta\Phi$ array was tested using an electro-optic modulator to induce a fixed phase shift on the probe.

5.5 Measurement calibration using electro-optic modulator

A crucial step in measuring the THz radiation with single-photon detectors is understanding the strength of field required to observe a measurable phase shift in the single-photon regime. In order to calibrate the balanced detection acquisition for the single-photon measurement, a free-space electric-optic modulator (EOM) was used in order to characterise the magnitude of the expected phase shift induced by the THz signal. The Pockel cell type amplitude modulator consists of dual MgO-doped lithium niobate ($LiNbO_3$) crystals where an external electric field can be applied. When a driving voltage is applied, a change in the refractive properties of the crystal occurs resulting in a change in the polarisation state of the probing beam. This mechanism is useful to simulate the detectable phase induced on the weak probe by the proposed THz field. The electro-optic amplitude modulator used was also configured so that the applied voltage is applied in a direction which is perpendicular to the propagation direction. In this measurement, the calibration of our single-photon balanced detection scheme can be performed in an experimental setting using a EOM to induce a phase shift onto the squeezed vacuum probe beam. Degenerate photon pairs are produced via spontaneous parametric down-conversion (SPDC) by focusing the pump field into a 0.5 mm long periodically poled magnesium-doped lithium niobate crystal (MgO-

PPLN) in a Type-0 phase matched configuration. Off-axis parabolic mirrors of equivalent focal length 50 mm were used to focus the pump beam to 13 µm into the crystal and to collect and collimate the generated radiation. As performed before, the source was characterised in the high-photon flux regime varying the crystal temperature to maximise the flux incident on an InGaAs photodiode (Thorlabs, PDA10DT) within a 12 nm spectral region centered at 1560 nm (Thorlabs FBH1550-12). The experimental scheme in Figure 5.10 shows the setup designed to understand the shift induced by an externally modulated electric field on a squeezed vacuum probe. In order to maximise transmission at the field wavelength of 1560 nm, all optical components were anti-reflection (AR) coated.

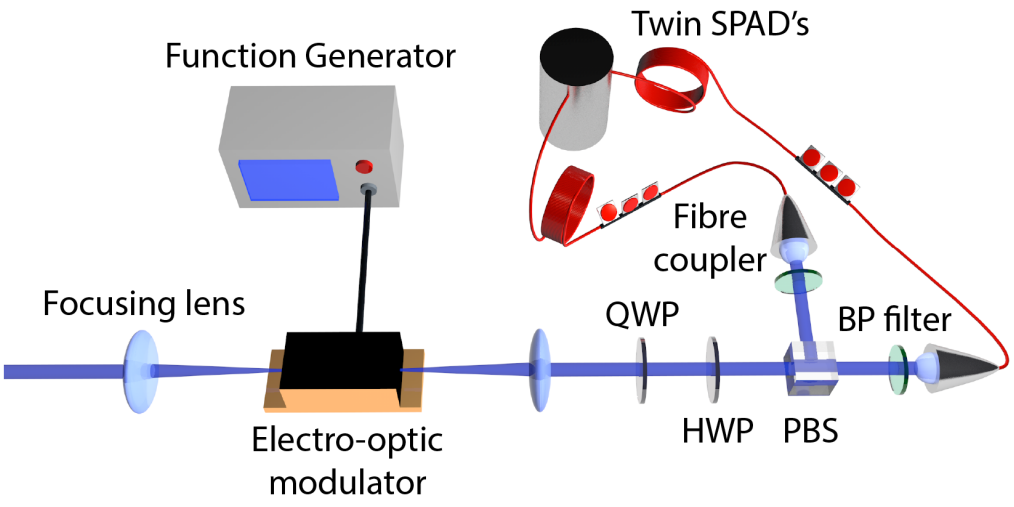

Figure 5.10: Experimental scheme for calibration of phase detection using a modulated EOM on a squeezed vacuum source. Strong external fields induce a phase shift observed by the difference between single counts detected by twin SPAD's.

A 200 mm AR-coated lens was used to focus the SPDC field into the 2 mm diameter clear aperture of the Thorlabs Electro-optic Amplitude Modulator (EO-AM-NR-C3). The voltage supply was provided by a Siglent function generator (SDG2042X) which produced a modulated square wave with frequency 10 kHz, duty cycle of 50% and a peak output voltage of + 20 V. The characteristics of this modulation function were chosen with the THz field measurement in mind. To this end, the minimum possible rise time setting of 8.4 ns was chosen in order to improve modulation resolution for time-tagging electronic devices employed in detection. By understanding the relationship between the phase shift induced, $\Delta\Phi$ and the applied voltage across the EOM,

$$\Delta\Phi = \frac{2\pi L}{\lambda d}(r_{33}n_e^3 - r_{13}n_o^3)V_{app}\,, \tag{5.10}$$

where λ is the operating wavelength, L is the optical path length, r_{ij} are the electro-optic coefficients and d is the electrode spacing. The half-wave voltage V_π, the voltage required to induce a π radian phase shift, of lithium niobate can be defined by,

$$V_\pi = \frac{\lambda d}{(r_{33}n_e^3 - r_{13}n_o^3)L}\,, \tag{5.11}$$

where λ is the operating wavelength, L is the optical path length and d is the electrode spacing. It is worth mentioning that the extraordinary and ordinary indices of refraction n_e, n_o are also temperature dependent and therefore

exhibit a static birefringence which can lead to polarisation discrepancies with no external field present. This effect is minimised in amplitude modulators by configuring the two crystals in orthogonal orientations to each other in order to reduce the temperature dependent static birefringence. Clearly, the V_π will also be larger for higher wavelengths compared with visible wavelengths.

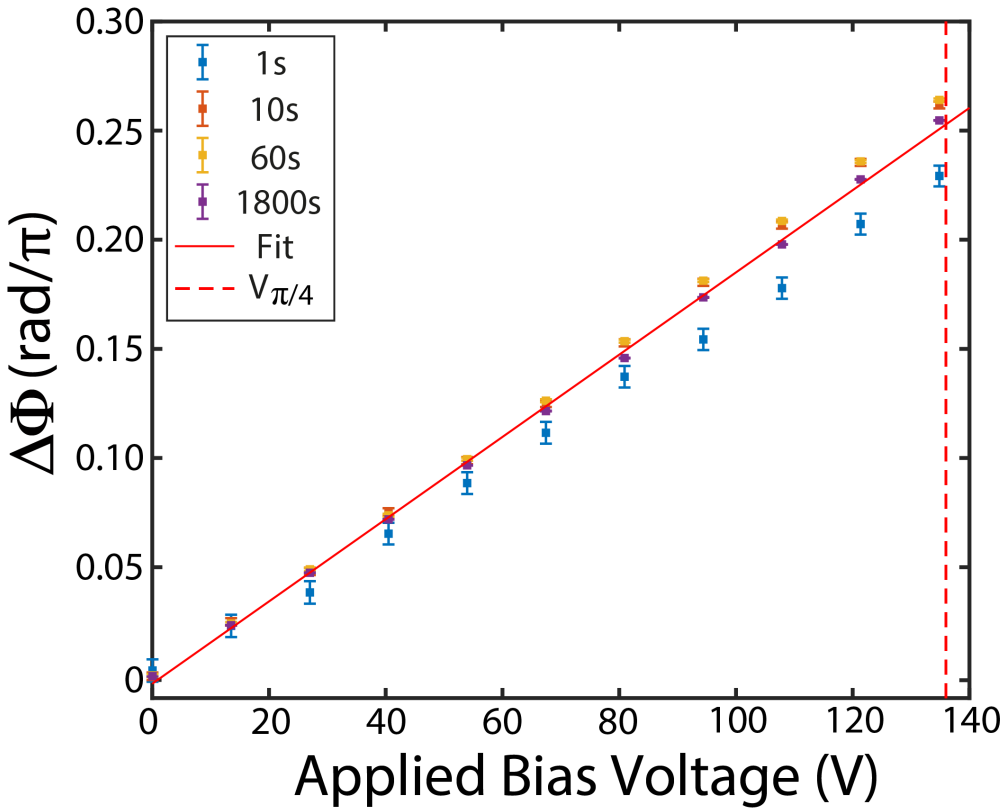

Figure 5.11: The phase change $\Delta\Phi$ is extracted as a function of the external potential across the EOM up to the quarter-wave voltage $V_{\pi/4}$ (red, dashed) for various integration times. A linear fit to the 1800 s integrated data (red) is included to guide the eye.

For our experimental specifications, the V_π was around 539 V and therefore a Thorlabs high voltage amplifier (HVA200) was employed to amplify the function generated signal to up to a maximum output voltage of 200 V. This amplification allowed us to provide an applied bias voltage of up to the quarter-wave voltage $V_{\frac{\pi}{4}}$. Once the EOM was configured, the SPDC field was collimated by another AR-coated lens before passing through a quarter-wave plate (Newport, 10RP04-40) followed by an achromatic half wave-plate (B. Halle, RAC 6.2.10) used to control the polarisation orientation. In a standard polarimetric detection scheme, the light enters a polarising beam splitter (PBS) with high extinction ratio before passing 12 nm bandpass filters and coupling into twin single-photon avalanche detectors (SPAD). The Hydraharp time-tagging electronics allow for free-running multi-channel photon detection and the counts detected were optimised on the SPDC field generated. The balanced detection scheme detailed before was incorporated to extract phase information corresponding to the external applied field. Figure 5.11 shows the linear relationship for the phase shift as a function of the applied bias voltage for various integration times. Numerical work on the Poissonian noise sampled from the two detectors used was performed. This allowed us to take advanced of the Skellam distribution to better understand the effects of the difference measurement from each Poissonian noise distribution for each detector. In the ideal case, the phase shift induced by the EOM will result in an unbalance of the signal on one photon counter with respect to the other, such that $\Delta N = (\langle N_1 \rangle + \langle N_2 \rangle)\Delta\Phi$ where $\langle N_1 \rangle$

and $\langle N_2 \rangle$ are the average counts on each of the two detectors. In a shot-noise limited measurement, the minimum detectable phase shift will then be $\sigma(\Delta\Phi) \approx (\langle N_1 \rangle + \langle N_2 \rangle)^{-\frac{1}{2}}$ as found in relevant literature [133]. Figure 5.12 shows the expected variance of the detection method using an EOM with 300 kHz counts indicating the measurement was shot-noise limited.

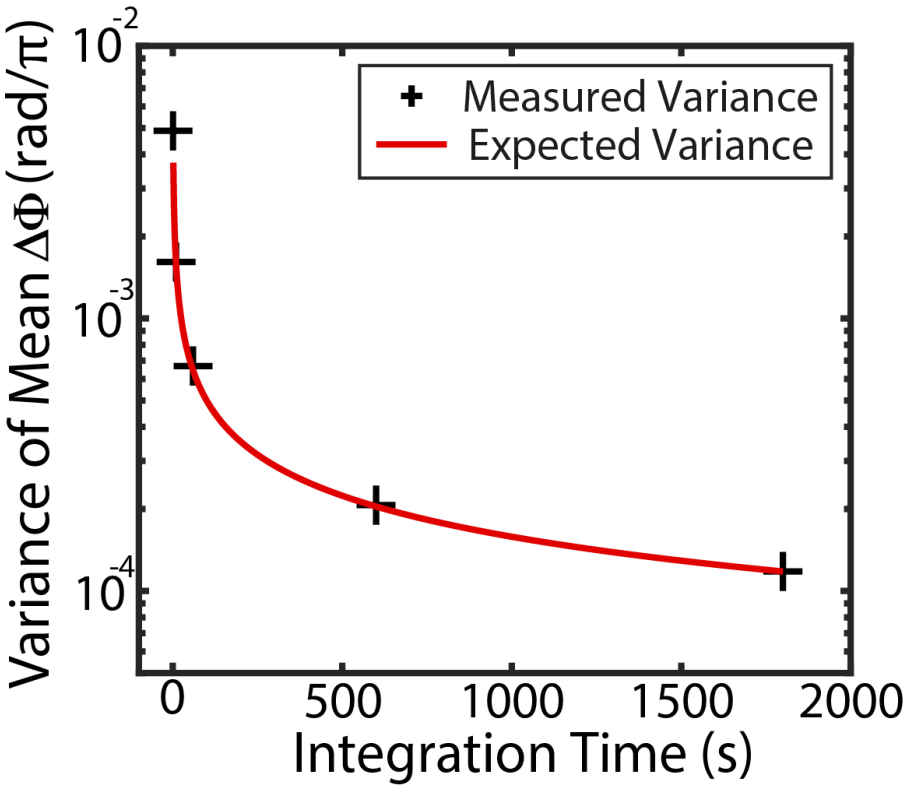

Figure 5.12: Measured variance of the $\Delta\Phi$ detection method against measurement time using an EOM with a squeezed vacuum probe. The fit (red) details the expected variance discussed in text showing shot-noise limited detection.

5.6 THz detection with single-photon detectors

Having experimentally confirmed the shot-noise limited sensitivity of the detection system with the EOM calibration, the experimental setup was modified for the detection of single-cycle THz fields. From the previously estimated THz peak field ($\simeq$ 130 V/cm) measured with the classical THz-TDS setup, the expected maximum phase shift introduced was $\Delta\Phi \simeq 2.4 \times 10^{-4}\pi$. Figure 5.13 shows a complete sketch of the experimental setup.

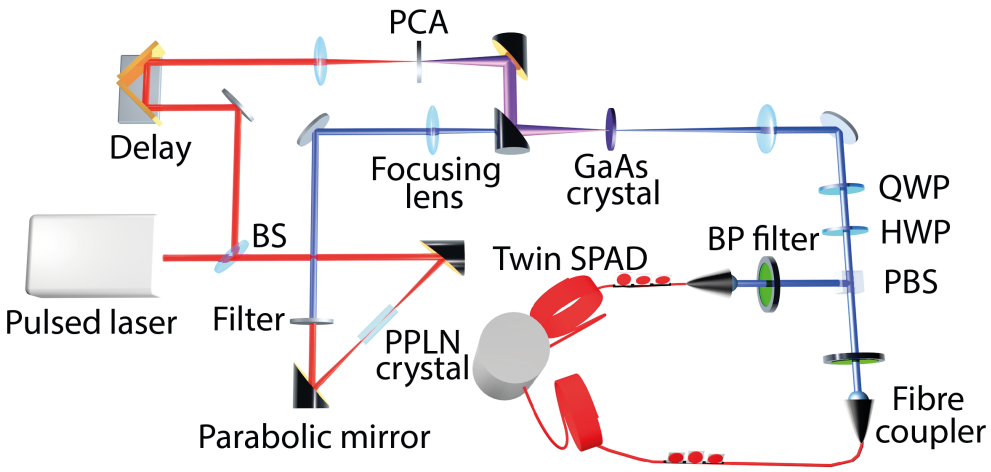

Figure 5.13: Experimental scheme for measuring THz fields using a squeezed vacuum probe. The THz field generated from a photo-excited PCA was overlapped with the squeezed vacuum pulse into a GaAs electro-optical crystal. The phase shift introduced by the THz pulse on the squeezed vacuum probe is measured by a balanced detection using single-photon detectors.

The EOM was substituted with the AR-GaAs detection crystal excited with the THz radiation previously characterised. In order to ensure the maximum THz field amplitude, the experiment was once again housed in a sealed enclosure purged with Nitrogen gas. A THz-induced shift was estimated to become visible at the correct delay after 10 minutes of acquisition determined using the estimated maximum phase shift and a 800 kHz photon rate. As before the squeezed vacuum probe was filtered in 12 nm bandwidth centred at 1560 nm. The delay around the peak of the THz field was scanned for 10 minutes integration time for each point but it was insufficient to obtain a signal above the noise.

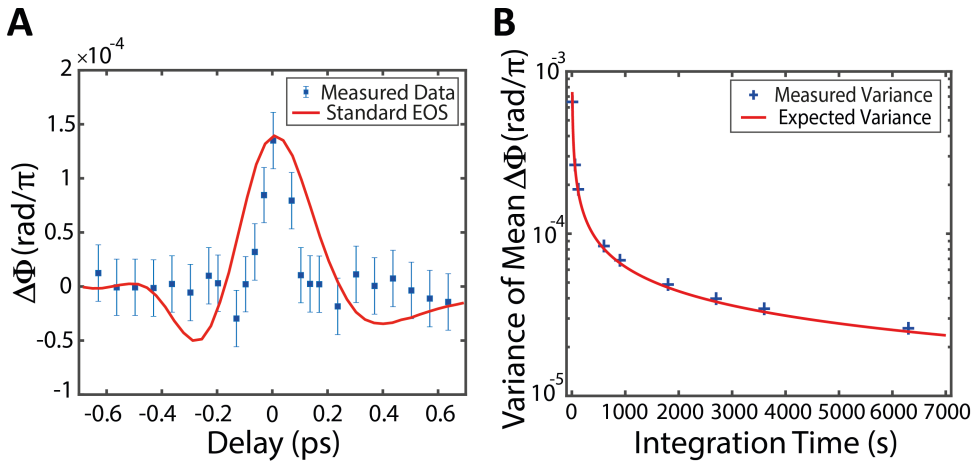

Figure 5.14: Terahertz detection using single photons. (A) Measured phase shift ($\Delta\Phi$) induced by THz field (blue squares) overlapped with the phase shift from standard electro-optic sampling (red line). The integration time for each data point was 105 mins. (B) Measured variance of the detection method indicating the final measurement is shot-noise limited so THz field is not adding noise.

The challenge associated with this measurement was ensuring all of the contributing variables were correct and many scans of the region of interest were performed without obtaining a signal. Optimisation of the spatial and temporal overlap between interacting fields was more rigorously performed and longer integration times used in order to obtain a signal. Figure 5.14 (A) shows the measured phase shift induced by the THz radiation on the infrared squeezed vacuum probe pulse as a function of their relative delay (blue squares). A signal-to-noise of 5 was obtained with an acquisition time of 105 minutes for each data point. This was compared against the normalised THz trace measured with the classical THz-TDS obtained via electro-optic sampling (red curve). The peak measured phase shift of $\Delta\Phi \simeq 1.35 \times 10^{-4}\pi$ is smaller than the value expected from the classical probe ($\Delta\Phi \simeq 2.4 \times 10^{-4}\pi$) but is a small difference when considering the experimental challenges with spatial overlap/ coupling. There are temporal differences in the pulse duration of the field trace measured with the squeezed vacuum and the coherent probe. The shot-noise limited nature of the measurement can be shown in Figure 5.14 (B) where the phase noise at the THz temporal coordinate is measured (blue crosses) and plotted against the expected values for the experimental conditions (red curve). This measurement demonstrated that it is possible to obtain phase information with THz-TDS using a probe pulse at the single-photon level. This form of ultrafast phase modulation on squeezed vacuum radiation within a picosecond window has not been demonstrated before to the author's knowledge. This is a step in the direction of using more

exotic quantum states to potentially enhance the detection of THz radiation.

5.7 NOON state for quantum-enhanced THz detection

Having performed the time-resolved detection of THz single-cycle pulses using single-photon detection and overcome the challenges which lay there, the next step moving in the direction of quantum-enhanced THz detection was to generate a suitable quantum state. Many quantum metrology schemes feature a type of path-entangled state called the NOON state. Consider the general form of the NOON state with a superposition of N photons being in mode a and *not* in mode b and vice versa:

$$|NOON\rangle = \frac{1}{\sqrt{2}}(|N_a, 0_b\rangle + |0_a, N_b\rangle). \tag{5.12}$$

This particular state has been applied to numerous measurement applications in interferometry and beyond [155–157]. These states give rise to one the key concepts of quantum metrology called *phase super-resolution* where upon evolution the state acquires a phase $N\Phi$ rather than just Φ. Hence they produce interference fringes which oscillate with frequency $\cos N\Phi$ which is N times faster than a classical interference pattern over a cycle of 2π [158]. Phase super-resolution has been demonstrated many times since the N=2 case in a Mach-Zehnder interferometer [159] and for increasing N. However, in order to obtain a quantum advantage, the visibility of the interference

fringes V and detection efficiency η must satisfy the threshold

$$\eta N V^2 > 1. \tag{5.13}$$

This is required in order to acheive *phase super-sensitivity* which is the reduction in phase uncertainty $\Delta\Phi$ compared with a classical counterpart. The limit on phase sensitivity with no quantum correlations is the shot-noise limit (SNL) which is defined by $\Delta\Phi_{SNL} = \frac{1}{\sqrt{N}}$. NOON states have the capability to not only violate the SNL but to approach the fundamental limit of phase uncertainty, the Heisenberg limit (HL),

$$\Delta\Phi_{HL} = \frac{1}{N}\,, \tag{5.14}$$

which is a significant improvement in comparison to the SNL. Recent experimental demonstrations have shown unconditional violation of the shot-noise limit using N=2 NOON states with high detection efficiency and visibility [160]. To expand on the previous THz work, a N=2 NOON state similar to the referenced measurement above was generated and characterised with a Sagnac double-pass scheme.

5.7.1 NOON state using Sagnac interferometer

To drive this non-linear process, the same tunable Coherent Discovery laser with average power of up to 1.8 W at 780 nm was used. From the source, the pump pulse propagated with a full width half maximum (FWHM) beam width of 0.9 mm which was expanded to 2.2 mm using an optical telescope in order to satisfy the optimal coupling criterion identified in [64].

Figure 5.15 shows the design of the Sagnac interferometer setup. The design (found in relevant literature) utilised a dual-wavelength polarising beam-splitter (DPBS) coated for pump and signal wavelengths to generate counter propagating pump beams [161] . The balance of the bidirectional inputs was controlled using a half waveplate prior to incidence of the DPBS entering the Sagnac interferometer. The embedded PPLN crystal was positioned on a translational stage in the focal points of two identical off-axis parabolic mirrors to focus the bidirectional pump beams and collimate the down-converted signal beams. The focal length of the focusing parabolic mirrors (f=101.6 mm) and input beam size (2.2 mm FWHM) determine the pump beam properties in the crystal. A broadband dual-wavelength half-waveplate (DHWP) was utilised inside the cavity in order to control the polarisation of pump and signal wavelengths inside the cavity. The crystal required a horizontal pump polarisation so the working operation of the polarisation-entangled state at the output of the interferometer can be understood as detailed below.

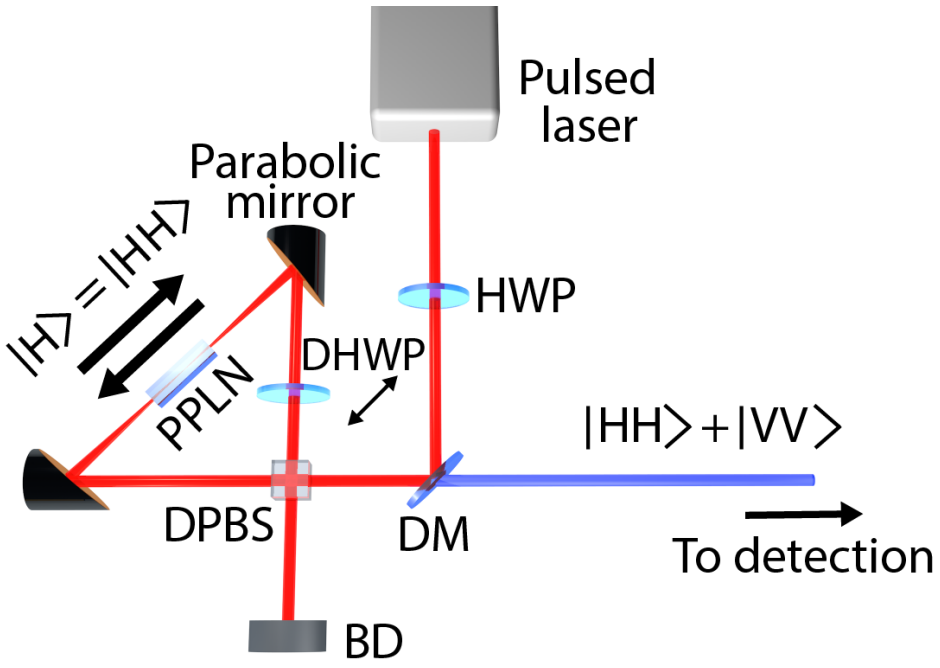

Figure 5.15: Experimental setup for NOON state generation using a Sagnac interferometer. A dichroic mirror (DM) directs the polarised pump field into bidirectional Sagnac cavity via a dual-wavelength polarising beam splitter (DPBS). Parabolic mirrors are used to focus the pump field into a Type-0 PPLN crystal to generate horizontally polarised photon pairs in each direction. Polarisation control using a dual-wavelength half-wave plate (DHWP) orientated at 45 degrees results in the desired state exiting the cavity. A beam dump (BD) and the dichroic optic were used to remove the pump field.

The reflected DPBS output is in the vertical polarisation basis $|V\rangle$ before passing through a DHWP fixed at 45° to generate a $|H\rangle$ polarised pump field for the PPLN to generate photon pairs in polarisation invariant basis $|HH\rangle$ expected from Type-0 down-conversion. In the alternative path, the transmitted DPBS beam in the form $|H\rangle$ is unchanged and pumps the PPLN

generating the expected $|HH\rangle$ state before being rotated by the DHWP after the crystal to the $|VV\rangle$ basis. When recombining on the DPBS, the polarisation-entangled state generated is of the form:

$$|\Phi^+\rangle = \frac{1}{\sqrt{2}}(|HH\rangle + e^{i\phi}|VV\rangle), \tag{5.15}$$

where ϕ denotes the accumulated phase difference between the two output amplitudes largely sensitive to the position of the crystal inside the cavity and the alignment of each optical path [30, 31]. The dichroic mirror (DM) is coated to transmit the down-converted wavelength whilst reflecting the pump wavelengths effectively acting as a filter for the generated quantum state. The generated N=2 NOON state (N=2) is significant due to its peculiar quantum properties enhancing measurement sensitivity by a factor of $\sqrt{2}$ in comparison to classical limits [32]. In a very similar fashion as discussed in detail in Chapter 3, coincidence detection with 50 nm bandpass filters was performed using the ID230 SPAD's used previously. A CAR measurement for this source was performed by collecting coincidences for varying input powers (single counts) with an integration time of 600 s. A peak CAR of 464 ± 109 was measured in the photon-starved regime. This measurement provides an insight into the best input power incident on the crystal to use for characterising the state entanglement. A pump power of 5 mW was used to ensure the purity of the state being measured but with sufficient count rates above the dark counts.

5.7.2 NOON state entanglement characterisation

In order to characterise the entanglement of the NOON state generated in the Sagnac cavity scheme, a projective polarisation detection scheme similar to the previous polarisation entanglement measurements performed at 2.1 μm in Chapter 3. The polarisation-entangled state generated was transmitted through an anti-reflection coated dichroic mirror at 1560 nm before being incident on a non-polarising 50:50 beamsplitter. Each separated beam was passed through a $\lambda/4$ plate, $\lambda/2$ plate mounted on motorised rotational stages and a thin-film polariser before being coupled to single-photon detectors. Since for each quantum state there exists four projection measurements corresponding to operators and we are considering two photon states with two possible polarisations, a collection of 16 total measurements are required.

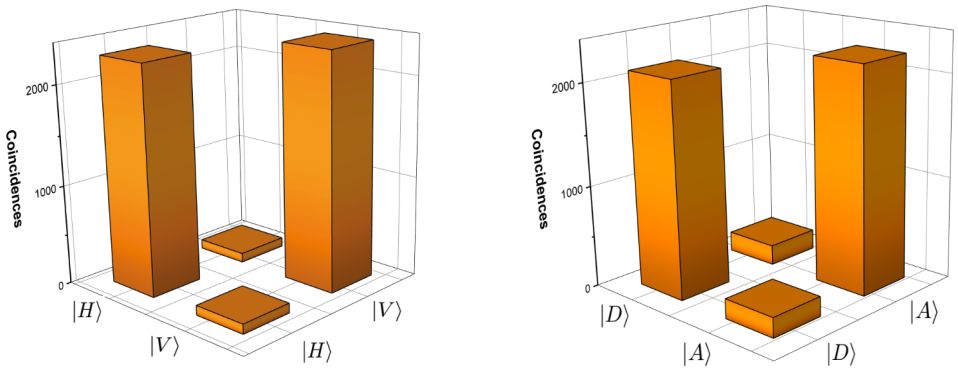

Figure 5.16: Tomographic reconstruction of the experimentally obtained two-photon $|\Phi^+\rangle$ state in all combinations of the bases $|H\rangle$ $|V\rangle$ $|D\rangle$ $|A\rangle$.

As before, the probabilities for each polarisation state are measured by obtaining coincidence counts from a time-correlated single-photon counting system (Hydraharp 400). Figure 5.16 shows the tomographic reconstruction for the generated $|\Phi^+\rangle$ state. Motorised stages were used to project onto measurement basis states in order to violate the CHSH inequality previously defined. Violation of this condition represents the validity of a non-local model of reality and constrains the polarisation correlation as a function of polariser angular displacement. Maximal violation of the CHSH inequality in the case of the maximally-entangled singlet state $|\Phi^+\rangle = \frac{1}{\sqrt{2}}(|HH\rangle + e^{i\phi}|VV\rangle)$ using orientation angles orientation angles of $\theta_A = 0°$, $\theta'_A = 45°$, $\theta_B = 22.5°$, $\theta'_B = 67.5°$. For each of the 4 orientations of polariser A are the corresponding polariser B angles (11.25°, 33.75°, 56.25°, 78.75°). Using these measurement orientations, the S-parameter obtained was $S = 2.39 \pm 0.02$ giving violation by 20 standard deviations clearly demonstrating entanglement. In order to unconditionally confirm a violation of the CHSH inequality, the fringe visibility also must be defined to exceed the threshold of $> 71\%$. For this source, this value of the S parameter measured corresponds to a visibility of $V = 88 \pm 0.1\%$.

5.8 Discussion and future work

The work demonstrates that time-resolved detection of THz single-cycle pulses can be performed using single-photon detectors. Using a lock-in style phase detection method and employing a squeezed vacuum probe, weak THz single-cycle pulse with peak amplitude of $\simeq 130$ V/cm with a signal-to-noise ratio of 5 for an acquisition time of 105 minutes was measured. Furthermore, sub-picosecond single-cycle THz pulses have been used to impart a < 0.5 mrad phase shift on a squeezed vacuum probe. The magnitude of this phase shift imparted on the probe was limited by the strength of the THz field generated by the PCA. Throughout this measurement, the PCA was operated close to its damage threshold to maximise the peak THz field. More ambitious measurements could utilise the scheme demonstrated here to impart full-wave phase shifts using larger THz peak fields to demonstrate ultrafast encoding of phase information [162]. Experimentally, there are many challenges to ensure the THz field generated is fully utilised in the electro-optic interaction. Great effort was taken to maximise the spatial overlap of the THz field and the probe however due to the long duration of these measurements marginal misalignment is almost unavoidable. The significant absorption of THz radiation in air was also minimised in these measurements by isolating and purging the THz enclosure with Nitrogen gas which was maintained at $\simeq 5$ % humidity throughout which could be further optimised in future measurements. Additionally, as we are using a tunable output, this

allows alternative wavelengths to be used for eventual photon counting as the SNSPD's being used optimised QE of 90% at 1400nm.

As previously discussed, while no quantum enhancement in measurement of the THz fields can be shown at this stage, this work lays the foundations for investigating utilising the properties of non-classical resources such as NOON states or single photons. Using the N = 2 NOON state characterised earlier in this chapter, a two-fold enhancement in phase shift sensitivity could be obtained with THz EOS in the low photon flux regime. The importance of maintaining a low photon flux is a prerequisite for all near-field time-resolved imaging to ensure the probe does not damage or contaminate the sample. Differently from above, the improvement induced by the non-classical nature of light in this case is not limited to situations requiring a very weak probe signal, as indeed twin beams maintain quantum behaviour even at high intensities. Therefore, in situations where the detection noise is determined by the shot noise of the probe beam, the signal to noise ratio can be increased by 4 dB below the classical limit [163, 164].

Bibliography

[1] R. W. Boyd, *Nonlinear optics*. Academic Press, 2008.

[2] Z. Y. J. Ou, *Multi-photon quantum interference*. Springer US, 2007.

[3] J. E. Sipe, L. G. Helt, and M. Liscidini, "How does it scale? Comparing quantum and classical nonlinear optical processes in integrated devices," *Journal of the Optical Society of America B*, vol. 29, pp. 2199–2212, 8 2012.

[4] D. Magde and H. Mahr, "Study in ammonium dihydrogen phosphate of spontaneous parametric interaction tunable from 4400 to 16 000 Å," *Physical Review Letters*, vol. 18, p. 905, 5 1967.

[5] R. L. Byer and S. E. Harris, "Power and bandwidth of spontaneous parametric emission," *Physical Review*, vol. 168, p. 1064, 4 1968.

[6] D. C. Burnham and D. L. Weinberg, "Observation of simultaneity in parametric production of optical photon pairs," *Physical Review Letters*, vol. 25, p. 84, 7 1970.

[7] I. Shoji, T. Kondo, A. Kitamoto, M. Shirane, and R. Ito, "Absolute scale of second-order nonlinear-optical coefficients," *Journal of the Optical Society of America B*, vol. 14, pp. 2268–2294, 9 1997.

[8] J. G. Rarity, K. D. Ridley, and P. R. Tapster, "Absolute measurement of detector quantum efficiency using parametric downconversion," *Applied Optics*, vol. 26, pp. 4616–4619, 11 1987.

[9] P. G. Kwiat, A. M. Steinberg, R. Y. Chiao, P. H. Eberhard, and M. D. Petroff, "Absolute efficiency and time-response measurement of single-photon detectors," *Applied Optics*, vol. 33, p. 1844, 4 1994.

[10] C. Zhang, Y. F. Huang, B. H. Liu, C. F. Li, and G. C. Guo, "Spontaneous parametric down-conversion sources for multiphoton experiments," *Advanced Quantum Technologies*, vol. 4, p. 2000132, 5 2021.

[11] K. Garay-Palmett, A. B. U'Ren, F. Kaneda, and P. G. Kwiat, "Heralded single-photon source utilizing highly nondegenerate, spectrally factorable spontaneous parametric downconversion," *Optics Express*, vol. 24, pp. 10733–10747, 5 2016.

[12] E. Martín-López, A. Laing, T. Lawson, R. Alvarez, X. Q. Zhou, and J. L. O'brien, "Experimental realization of Shor's quantum factoring algorithm using qubit recycling," *Nature Photonics*, vol. 6, pp. 773–776, 10 2012.

[13] T. D. Ladd, F. Jelezko, R. Laflamme, Y. Nakamura, C. Monroe, and J. L. O'Brien, "Quantum computers," *Nature*, vol. 464, pp. 45–53, 3 2010.

[14] D. Bouwmeester, J. W. Pan, K. Mattle, M. Eibl, H. Weinfurter, and A. Zeilinger, "Experimental quantum teleportation," *Nature*, vol. 390, pp. 575–579, 12 1997.

[15] R. Dalidet, F. Mazeas, E. Nitiss, O. Yakar, A. Stroganov, S. Tanzilli, L. Labonté, and C.-S. Brès, "Near perfect two-photon interference out of a down-converter on a silicon photonic chip," *Optics Express*, vol. 30, p. 11298, 2 2022.

[16] X. Guo, C. L. Zou, C. Schuck, H. Jung, R. Cheng, and H. X. Tang, "Parametric down-conversion photon-pair source on a nanophotonic chip," *Light: Science & Applications*, vol. 6, pp. 16249–16249, 11 2016.

[17] L. K. Shalm, E. Meyer-Scott, B. G. Christensen, P. Bierhorst, M. A. Wayne, M. J. Stevens, T. Gerrits, S. Glancy, D. R. Hamel, M. S. Allman, K. J. Coakley, S. D. Dyer, C. Hodge, A. E. Lita, V. B. Verma, C. Lambrocco, E. Tortorici, A. L. Migdall, Y. Zhang, D. R. Kumor, W. H. Farr, F. Marsili, M. D. Shaw, J. A. Stern, C. Abellán, W. Amaya, V. Pruneri, T. Jennewein, M. W. Mitchell, P. G. Kwiat, J. C. Bienfang, R. P. Mirin, E. Knill, and S. W. Nam, "Strong loophole-free test of local realism," *Physical Review Letters*, vol. 115, p. 250402, 12 2015.

[18] M. Giustina, M. A. Versteegh, S. Wengerowsky, J. Handsteiner, A. Hochrainer, K. Phelan, F. Steinlechner, J. Kofler, J. Åke Larsson, C. Abellán, W. Amaya, V. Pruneri, M. W. Mitchell, J. Beyer, T. Gerrits, A. E. Lita, L. K. Shalm, S. W. Nam, T. Scheidl, R. Ursin, B. Wittmann, and A. Zeilinger, "Significant-loophole-free test of Bell's theorem with entangled photons," *Physical Review Letters*, vol. 115, p. 250401, 12 2015.

[19] L. Mandel and E. Wolf, *Optical coherence and quantum optics*. Cambridge University Press, 1995.

[20] M. Taghinejad, Z. Xu, K. T. Lee, T. Lian, and W. Cai, "Transient second-order nonlinear media: Breaking the spatial symmetry in the time domain via hot-electron transfer," *Physical Review Letters*, vol. 124, p. 013901, 1 2020.

[21] M. M. Choy and R. L. Byer, "Accurate second-order susceptibility measurements of visible and infrared nonlinear crystals," *Physical Review B*, vol. 14, p. 1693, 8 1976.

[22] C. Chen and G. Liu, "Recent advances in nonlinear optical and electro-optical materials," *Annual Review of Materials Science*, vol. 16, pp. 203–243, 11 2003.

[23] A. Christ, A. Fedrizzi, H. Hübel, T. Jennewein, and C. Silberhorn, "Parametric down-conversion," *Experimental Methods in the Physical Sciences*, vol. 45, pp. 351–410, 1 2013.

[24] S. Karan, S. Aarav, H. Bharadhwaj, L. Taneja, A. De, G. Kulkarni, N. Meher, and A. K. Jha, "Phase matching in β-barium borate crystals for spontaneous parametric down-conversion," *Journal of Optics*, vol. 22, p. 083501, 6 2020.

[25] A. Yariv, *Quantum electronics*. John Wiley and Sons Inc., 1967.

[26] G. A. Magel, M. M. Fejer, and R. L. Byer, "Quasi-phase-matched second-harmonic generation of blue light in periodically poled $LiNbO_3$," *Applied Physics Letters*, vol. 56, p. 108, 6 1998.

[27] Y.-H. Kim, M. V. Chekhova, S. P. Kulik, M. H. Rubin, and Y. Shih, "Interferometric Bell-state preparation using femtosecond-pulse-pumped spontaneous parametric down-conversion," *Physical Review A*, vol. 63, p. 11, 3 2001.

[28] C. K. Hong, Z. Y. Ou, and L. Mandel, "Measurement of subpicosecond time intervals between two photons by interference," *Physical Review Letters*, vol. 59, pp. 2044–2046, 11 1987.

[29] J. Carvioto-Lagos, G. Armendariz P, V. Velázquez, E. López-Moreno, M. Grether, and E. J. Galvez, "The Hong–Ou–Mandel interferometer in the undergraduate laboratory," *European Journal of Physics*, vol. 33, pp. 1843–1850, 11 2012.

[30] T. Kim, M. Fiorentino, and F. N. C. Wong, "Phase-stable source of polarization-entangled photons using a polarization Sagnac interferometer," *Physical Review A*, vol. 73, p. 012316, 1 2006.

[31] H. Kim, O. Kwon, and H. S. Moon, "Pulsed Sagnac source of polarization-entangled photon pairs in telecommunication band," *Scientific Reports*, vol. 9, p. 5031, 12 2019.

[32] L. Zhang and K. W. C. Chan, "Scalable generation of multi-mode NOON states for quantum multiple-phase estimation," *Scientific Reports*, vol. 8, p. 11440, 12 2018.

[33] N. Bruno, E. Zambrini Cruzeiro, A. Martin, and R. Thew, "Simple, pulsed, polarization entangled photon pair source," *Optics Communications*, vol. 327, pp. 3–6, 9 2014.

[34] S. Prabhakar, S. G. Reddy, A. Aadhi, A. Kumar, C. P, G. K. Samanta, and R. P. Singh, "Spatial distribution of spontaneous parametric down-converted photons for higher order optical vortices," *Optics Communications*, vol. 326, pp. 64–69, 12 2013.

[35] H. Di Lorenzo Pires, F. M. G. J. Coppens, and M. P. van Exter, "Type-I spontaneous parametric down-conversion with a strongly focused pump," *Physical Review A*, vol. 83, p. 033837, 3 2011.

[36] N. Gisin, G. Ribordy, W. Tittel, and H. Zbinden, "Quantum cryptography," *Reviews of Modern Physics*, vol. 74, p. 145, 3 2002.

[37] M. D. Eisaman, J. Fan, A. Migdall, and S. V. Polyakov, "Invited review article: Single-photon sources and detectors," *Review of Scientific Instruments*, vol. 82, p. 071101, 7 2011.

[38] C. H. Bennett and G. Brassard, "Quantum cryptography: Public key distribution and coin tossing," *Theoretical Computer Science*, vol. 560, pp. 7–11, 3 2020.

[39] W. K. Wootters and W. H. Zurek, "A single quantum cannot be cloned," *Nature*, vol. 299, pp. 802–803, 10 1982.

[40] G. Brassard, N. Lütkenhaus, T. Mor, and B. C. Sanders, "Limitations on practical quantum cryptography," *Physical Review Letters*, vol. 85, p. 1330, 8 2000.

[41] C.-Z. Peng, J. Zhang, D. Yang, W.-B. Gao, H.-X. Ma, H. Yin, H.-P. Zeng, T. Yang, X.-B. Wang, and J.-W. Pan, "Experimental long-distance decoy-state quantum key distribution based on polarization encoding," *Physical Review Letters*, vol. 98, p. 010505, 1 2007.

[42] A. Fedrizzi, R. Ursin, T. Herbst, M. Nespoli, R. Prevedel, T. Scheidl, F. Tiefenbacher, T. Jennewein, and A. Zeilinger, "High-fidelity transmission of entanglement over a high-loss free-space channel," *Nature Physics*, vol. 5, pp. 389–392, 5 2009.

[43] S. K. Liao, W. Q. Cai, J. Handsteiner, B. Liu, J. Yin, L. Zhang, D. Rauch, M. Fink, J. G. Ren, W. Y. Liu, Y. Li, Q. Shen, Y. Cao, F. Z. Li, J. F. Wang, Y. M. Huang, L. Deng, T. Xi, L. Ma, T. Hu, L. Li, N. L. Liu, F. Koidl, P. Wang, Y. A. Chen, X. B. Wang, M. Steindorfer, G. Kirchner, C. Y. Lu, R. Shu, R. Ursin, T. Scheidl, C. Z. Peng, J. Y. Wang, A. Zeilinger, and J. W. Pan, "Satellite-relayed intercontinental quantum network," *Physical Review Letters*, vol. 120, p. 030501, 1 2018.

[44] S. K. Liao, H. L. Yong, C. Liu, G. L. Shentu, D. D. Li, J. Lin, H. Dai, S. Q. Zhao, B. Li, J. Y. Guan, W. Chen, Y. H. Gong, Y. Li, Z. H. Lin, G. S. Pan, J. S. Pelc, M. M. Fejer, W. Z. Zhang, W. Y. Liu, J. Yin, J. G. Ren, X. B. Wang, Q. Zhang, C. Z. Peng, and J. W. Pan, "Long-distance free-space quantum key distribution in daylight towards inter-satellite communication," *Nature Photonics*, vol. 11, pp. 509–513, 7 2017.

[45] ASTM E490-00a International, "Standard solar constant and zero air mass solar spectral irradiance tables," 2019. Available : https://www.astm.org/e0490-00ar19.html.

[46] H. Kaushal and G. Kaddoum, "Optical communication in space: Challenges and mitigation techniques," *IEEE Communications Surveys and Tutorials*, vol. 19, pp. 57–96, 1 2017.

[47] D. Grassani, E. Tagkoudi, H. Guo, C. Herkommer, F. Yang, T. J. Kippenberg, and C. S. Brès, "Mid infrared gas spectroscopy using efficient fiber laser driven photonic chip-based supercontinuum," *Nature Communications*, vol. 10, pp. 1–8, 4 2019.

[48] G.-L. Shentu, J. S. Pelc, J.-W. Pan, M. M. Fejer, Q. Zhang, Q.-C. Sun, and X.-X. Xia, "Upconversion detection near 2 μm at the single photon level," *Optics Letters*, vol. 38, pp. 4985–4987, 12 2013.

[49] X. Gu, K. Huang, H. Pan, E. Wu, and H. Zeng, "Efficient mid-infrared single-photon frequency upconversion detection with ultra-low background counts," *Laser Physics Letters*, vol. 10, p. 055401, 3 2013.

[50] T. Bach, T. R. W. Herrmann, A. Haecker, M. S. Michel, and A. Gross, "Thulium: Yttrium-aluminium-garnet laser prostatectomy in men with refractory urinary retention," *BJU International*, vol. 104, pp. 361–364, 8 2009.

[51] G. L. Mansell, T. G. McRae, P. A. Altin, M. J. Yap, R. L. Ward, B. J. Slagmolen, D. A. Shaddock, and D. E. McClelland, "Observation of squeezed light in the 2 μm region," *Physical Review Letters*, vol. 120, p. 203603, 5 2018.

[52] J. Steinlechner, I. W. Martin, A. S. Bell, J. Hough, M. Fletcher, P. G. Murray, R. Robie, S. Rowan, and R. Schnabel, "Silicon-based optical

mirror coatings for ultrahigh precision metrology and sensing," *Physical Review Letters*, vol. 120, p. 263602, 6 2018.

[53] A. Knights, C. G. Littlejohns, D. Hagan, D. J. Thomson, F. Gardes, G. Z. Mashanovich, G. T. Reed, G. Xin, H. Wang, J. Wang, K. Li, M. Nedeljkovic, M. S. Rouifed, S.-U. Alam, S. Liu, W. Wang, W. Cao, and W. Zhang, "High-speed silicon modulators for the 2 μm wavelength band," *Optica*, vol. 5, pp. 1055–1062, 9 2018.

[54] A. D. Ellis, J. Zhao, and D. Cotter, "Approaching the non-linear Shannon limit," *Journal of Lightwave Technology*, vol. 28, pp. 423–433, 2 2010.

[55] D. J. Richardson, "New optical fibres for high-capacity optical communications," *Philosophical Transactions of the Royal Society A: Mathematical, Physical and Engineering Sciences*, vol. 374, p. 20140441, 3 2016.

[56] P. J. Roberts, F. Couny, H. Sabert, B. J. Mangan, D. P. Williams, L. Farr, M. W. Mason, A. Tomlinson, T. A. Birks, J. C. Knight, and P. S. Russell, "Ultimate low loss of hollow-core photonic crystal fibres," *Optics Express*, vol. 13, pp. 236–244, 1 2005.

[57] R. Soref, "Enabling 2 μm communications," *Nature Photonics*, vol. 9, pp. 358–359, 5 2015.

[58] F. Poletti, N. V. Wheeler, M. N. Petrovich, N. Baddela, E. N. Fokoua, J. R. Hayes, D. R. Gray, Z. Li, R. Slavík, and D. J. Richardson, "Towards high-capacity fibre-optic communications at the speed of light in vacuum," *Nature Photonics*, vol. 7, pp. 279–284, 3 2013.

[59] B. Corbett and F. Gunning, "Time to open the 2-μm window?," *Optics and Photonics News*, vol. 30, pp. 42–47, 3 2019.

[60] L. M. Rosenfeld, L. M. Rosenfeld, D. A. Sulway, D. A. Sulway, G. F. Sinclair, V. Anant, M. G. Thompson, J. G. Rarity, and J. W. Silverstone, "Mid-infrared quantum optics in silicon," *Optics Express*, vol. 28, pp. 37092–37102, 12 2020.

[61] M. Lamy, C. Finot, J. Fatome, M. Brun, P. Labeye, S. Nicolleti, A. Bogris, D. Syvridis, M. A. Ettabib, D. J. Richardson, P. Petropoulos, and K. Hammani, "Ten gigabit per second optical transmissions at 1.98 µm in centimetre-long SiGe waveguides," *Electronics Letters*, vol. 53, pp. 1213–1214, 8 2017.

[62] S. Prabhakar, T. Shields, A. C. Dada, M. Ebrahim, G. G. Taylor, D. Morozov, K. Erotokritou, S. Miki, M. Yabuno, H. Terai, C. Gawith, M. Kues, L. Caspani, R. H. Hadfield, and M. Clerici, "Two-photon quantum interference and entanglement at 2.1 µm," *Science Advances*, vol. 6, pp. 5195–5222, 3 2020.

[63] A. C. Dada, J. Kaniewski, C. Gawith, M. Lavery, R. H. Hadfield, D. Faccio, and M. Clerici, "Near-maximal two-photon entanglement for quantum communications at 2.1 µm," *Physical Review Applied*, vol. 16, p. L051005, 11 2021.

[64] D. Ljunggren and M. Tengner, "Optimal focusing for maximal collection of entangled narrow-band photon pairs into single-mode fibers," *Physical Review A*, vol. 72, p. 062301, 12 2005.

[65] K. H. Kao, A. S. Verhulst, W. G. Vandenberghe, B. Soree, G. Groeseneken, and K. D. Meyer, "Direct and indirect band-to-band tunneling in germanium-based TFETs," *IEEE Transactions on Electron Devices*, vol. 59, pp. 292–301, 2 2012.

[66] K. I. Harada, H. Takesue, H. Fukuda, T. Tsuchizawa, T. Watanabe, K. Yamada, Y. Tokura, and S. I. Itabashi, "Frequency and polarization

characteristics of correlated photon-pair generation using a silicon wire waveguide," *IEEE Journal on Selected Topics in Quantum Electronics*, vol. 16, pp. 325–331, 1 2010.

[67] Y. J. Lu and Z. Y. Ou, "Optical parametric oscillator far below threshold: Experiment versus theory," *Physical Review A*, vol. 62, p. 033804, 8 2000.

[68] K. Guo, E. N. Christensen, J. B. Christensen, J. G. Koefoed, D. Bacco, Y. Ding, H. Ou, and K. Rottwitt, "High coincidence-to-accidental ratio continuous-wave photon-pair generation in a grating-coupled silicon strip waveguide," *Applied Physics Express*, vol. 10, p. 062801, 6 2017.

[69] S. Arahira, N. Namekata, T. Kishimoto, and S. Inoue, "Experimental studies in generation of high-purity photon-pairs using cascaded χ^2 processes in a periodically poled $LiNbO_3$ ridge-waveguide device," *Journal of the Optical Society of America B*, vol. 29, p. 434, 3 2012.

[70] J. Chen, A. J. Pearlman, A. Ling, J. Fan, A. Migdall, P. G. Kwiat, K. Mattle, H. Weinfurter, A. Zeilinger, A. V. Sergienko, and Y. Shih, "A versatile waveguide source of photon pairs for chip-scale quantum information processing," *Optics Express*, vol. 17, pp. 6727–6740, 4 2009.

[71] S. Miki, T. Yamashita, H. Terai, and Z. Wang, "High performance fiber-coupled NbTiN superconducting nanowire single photon detectors with Gifford-McMahon cryocooler," *Optics Express*, vol. 21, pp. 10208–10214, 4 2013.

[72] S. Miki, M. Yabuno, T. Yamashita, and H. Terai, "Stable, high-performance operation of a fiber-coupled superconducting nanowire avalanche photon detector," *Optics Express*, vol. 25, pp. 6796–6804, 3 2017.

[73] F. Bouchard, A. Sit, Y. Zhang, R. Fickler, F. M. Miatto, Y. Yao, F. Sciarrino, and E. Karimi, "Two-photon interference: the Hong–Ou–Mandel effect," *Reports on Progress in Physics*, vol. 84, p. 012402, 12 2020.

[74] M. S. Kim, W. Son, V. Buzžek, and P. L. Knight, "Entanglement by a beam splitter: Nonclassicality as a prerequisite for entanglement," *Physical Review A*, vol. 65, p. 032323, 2 2002.

[75] C. K. Hong, Z. Y. Ou, and L. Mandel, "Measurement of subpicosecond time intervals between two photons by interference," *Physical Review Letters*, vol. 59, pp. 2044–2046, Nov. 1987.

[76] V. Giovannetti, S. Lloyd, and L. Maccone, "Advances in quantum metrology," *Nature Photonics*, vol. 5, pp. 222–229, 4 2011.

[77] Y. Israel, S. Rosen, and Y. Silberberg, "Supersensitive polarization microscopy using NOON states of light," *Physical Review Letters*, vol. 112, p. 103604, 3 2014.

[78] Y. Israel, I. Afek, S. Rosen, O. Ambar, and Y. Silberberg, "Experimental tomography of NOON states with large photon numbers," *Physical Review A*, vol. 85, p. 022115, 2 2012.

[79] Z.-Y. Zhou, S.-L. Liu, S.-K. Liu, Y.-H. Li, D.-S. Ding, G.-C. Guo, and B.-S. Shi, "Superresolving phase measurement with short-wavelength NOON states by quantum frequency up-conversion," *Physical Review Applied*, vol. 7, p. 064025, 6 2017.

[80] A. Einstein, B. Podolsky, and N. Rosen, "Can quantum-mechanical description of physical reality be considered complete?," *Physical Review*, vol. 47, pp. 777–780, 5 1935.

[81] N. Bohr, "Can quantum-mechanical description of physical reality be considered complete?," *Physical Review*, vol. 48, p. 696, 10 1935.

[82] D. Bohm, "A suggested interpretation of the quantum theory in terms of 'hidden' variables.," *Physical Review*, vol. 85, p. 166, 1 1952.

[83] J. S. Bell, "On the Einstein Podolsky Rosen paradox," *Physics Physique Fizika*, vol. 1, p. 195, 11 1964.

[84] G. Grynberg, A. Aspect, C. Fabre, and C. Cohen-Tannoudji, *Introduction to quantum optics: From the semi-classical approach to quantized light*. Cambridge University Press, 2010.

[85] G. Jensen, C. Marsh, and S. To, "Entangled photons and Bell's inequality," 11 2013. Available: www2.optics.rochester.edu/workgroups/lukishova/QuantumOpticsLab.

[86] A. Aspect, P. Grangier, and G. Roger, "Experimental realization of Einstein-Podolsky-Rosen-Bohm gedankenexperiment: A new violation of Bell's inequalities," *Physical Review Letters*, vol. 49, p. 91, 7 1982.

[87] J. F. Clauser, M. A. Horne, A. Shimony, and R. A. Holt, "Proposed experiment to test local hidden-variable theories," *Physical Review Letters*, vol. 23, pp. 880–884, 10 1969.

[88] M. Ruzbehani, "Simulation of the Bell inequality violation based on quantum steering concept," *Scientific Reports*, vol. 11, pp. 1–11, 3 2021.

[89] D. Dehlinger and M. W. Mitchell, "Entangled photons, nonlocality and Bell inequalities in the undergraduate laboratory," *American Journal of Physics*, vol. 70, pp. 903–910, 9 2002.

[90] S. Prabhakar, G. Reddy, A. Aadhi, A. Kumar, G. K. Samanta, and R. P. Singh, "Spatial distribution of spontaneous parametric down-converted photons for higher order optical vortices," in *2012 International Conference on Fiber Optics and Photonics*, pp. 1–3, Dec. 2012.

[91] D. V. Reddy, D. V. Reddy, R. R. Nerem, S. W. Nam, R. P. Mirin, and V. B. Verma, "Superconducting nanowire single-photon detectors with 98 % system detection efficiency at 1550 nm," *Optica*, vol. 7, pp. 1649–1653, 12 2020.

[92] J. Chang, J. W. Los, J. O. Tenorio-Pearl, N. Noordzij, R. Gourgues, A. Guardiani, J. R. Zichi, S. F. Pereira, H. P. Urbach, V. Zwiller, S. N. Dorenbos, and I. E. Zadeh, "Detecting telecom single photons with $99.5 \pm 0.5\%$ system detection efficiency and high time resolution," *APL Photonics*, vol. 6, p. 036114, 3 2021.

[93] H. Zhou, Y. Pan, L. You, H. Li, Y. Wang, Y. Tang, H. Wang, X. Liu, and Z. Wang, "Superconducting nanowire single photon detector with efficiency over 60% for 2-μm-wavelength," *IEEE Photonics Journal*, vol. 11, pp. 1–7, 12 2019.

[94] Y. Pan, H. Zhou, L. Zhang, H. Li, Y. Tang, H. Yu, M. Si, L. You, and Z. Wang, "Superconducting nanowire single-photon detector made of ultrathin γ-Nb_4N_3 film for mid-infrared wavelengths," *Superconductor Science and Technology*, vol. 34, p. 074001, 5 2021.

[95] J. Chang, J. W. N. Los, R. Gourgues, S. Steinhauer, S. N. Dorenbos, S. F. Pereira, H. P. Urbach, V. Zwiller, and I. E. Zadeh, "Mid-infrared single-photon detection using superconducting NbTiN nanowires with sub-15 ps time resolution in a Gifford-McMahon cryocooler," 7 2021.

[96] G.-L. Shentu, X.-X. Xia, Q.-C. Sun, J. S. Pelc, M. M. Fejer, Q. Zhang, and J.-W. Pan, "Upconversion single photon detection near 2 μm," Oct. 2013. arXiv: 1310.7422.

[97] G. G. Taylor, D. Morozov, N. R. Gemmell, K. Erotokritou, S. Miki, S. Miki, H. Terai, and R. H. Hadfield, "Photon counting lidar at 2.3 μm wavelength with superconducting nanowires," *Optics Express*, vol. 27, pp. 38147–38158, 12 2019.

[98] G. L. Mansell, T. G. McRae, P. A. Altin, M. J. Yap, R. L. Ward, B. J. Slagmolen, D. A. Shaddock, and D. E. McClelland, "Observation of squeezed light in the 2μm region," *Physical Review Letters*, vol. 120, 5 2018.

[99] G. T. Jasion, T. D. Bradley, K. Harrington, H. Sakr, Y. Chen, E. N. Fokoua, I. A. Davidson, A. Taranta, J. R. Hayes, D. J. Richardson, and F. Poletti, "Hollow core NANF with 0.28 db/km attenuation in the C and L bands," *Optical Fiber Communication Conference Post-deadline Papers 2020 (2020), paper Th4B.4*, vol. Part F174-OFC 2020, p. Th4B.4, 3 2020.

[100] W. Ni, C. Yang, Y. Luo, R. Xia, P. Lu, D. J. J. Hu, S. Danto, P. P. Shum, and L. Wei, "Recent advancement of anti-resonant hollow-core fibers for sensing applications," *Photonics*, vol. 8, p. 128, 4 2021.

[101] G. Bouwmans, L. Farr, J. C. Knight, F. Luan, B. J. Mangan, P. S. J. Russell, and H. Sabert, "Properties of a hollow-core photonic bandgap fiber at 850 nm wavelength," *Optics Express*, vol. 11, pp. 1613–1620, 7 2003.

[102] W. C. Huang, J. C. Knight, M. G. Welch, W. J. Wadsworth, P. J. Mosley, and B. J. Mangan, "Ultrashort pulse compression and delivery in a hollow-core photonic crystal fiber at 540 nm wavelength," *Optics Letters*, vol. 35, pp. 3589–3591, 11 2010.

[103] D. G. Ouzounov, F. R. Ahmad, D. Müller, N. Venkataraman, M. T. Gallagher, M. G. Thomas, J. Silcox, K. W. Koch, and A. L. Gaeta, "Generation of megawatt optical solitons in hollow-core photonic band-gap fibers," *Science*, vol. 301, pp. 1702–1704, 9 2003.

[104] F. Poletti, "Nested antiresonant nodeless hollow core fiber," *Optics Express*, vol. 22, pp. 23807–23828, 10 2014.

[105] Y. Sagae, T. Matsui, T. Sakamoto, and K. Nakajima, "Ultra-low crosstalk multi-core fiber with standard 125-μm cladding diameter for 10,000km-class long-haul transmission," *IEICE Transactions on Communications*, vol. 103, pp. 1199–1205, 2020.

[106] W. Chang, M. I. Hasan, and N. Akhmediev, "Mid-infrared supercontinuum generation in supercritical xenon-filled hollow-core negative curvature fibers," *Optics Letters*, vol. 41, pp. 5122–5125, 11 2016.

[107] U. Nasti, H. Sakr, H. Sakr, I. A. Davidson, F. Poletti, and R. J. Donaldson, "Utilizing broadband wavelength-division multiplexing capabilities of hollow-core fiber for quantum communications," *Applied Optics*, vol. 61, pp. 8959–8966, 10 2022.

[108] Y. W. Zhou, Z. F. Li, J. Zhou, N. Li, X. H. Zhou, P. P. Chen, Y. L. Zheng, X. S. Chen, and W. Lu, "High extinction ratio super pixel for long wavelength infrared polarization imaging detection based on plasmonic microcavity quantum well infrared photodetectors," *Scientific Reports*, vol. 8, pp. 1–8, 10 2018.

[109] A. Taranta, E. N. Fokoua, S. A. Mousavi, J. R. Hayes, T. D. Bradley, G. T. Jasion, and F. Poletti, "Exceptional polarization purity in antiresonant hollow-core optical fibres," *Nature Photonics*, vol. 14, pp. 504–510, 5 2020.

[110] O. Alia, R. S. Tessinari, T. D. Bradley, H. Sakr, K. Harrington, J. Hayes, Y. Chen, P. Petropoulos, D. Richardson, F. Poletti, G. T. Kanellos, R. Nejabati, and D. Simeonidou, "1.6 tbps classical channel coexistence with DV-QKD over hollow core nested antiresonant nodeless fibre (HC-NANF)," *2021 European Conference on Optical Communication, ECOC 2021*, 6 2021.

[111] N. Savage, "MIT Technology Review - 10 Emerging Technologies That Will Change Your World," 2004. Available : www.technologyreview.com/10-breakthrough-technologies/2004/.

[112] M. Tonouchi, "Cutting-edge terahertz technology," *Nature Photonics*, vol. 1, pp. 97–105, 2 2007.

[113] S. Perkowitz, "Navigating the terahertz gap – Physics World," 2020. Available : www.physicsworld.com/a/navigating-the-terahertz-gap/.

[114] M. B. Johnston, D. M. Whittaker, A. Corchia, A. G. Davies, and E. H. Linfield, "Simulation of terahertz generation at semiconductor surfaces," *Physical Review B*, vol. 65, p. 165301, 3 2002.

[115] L. Luo, I. Chatzakis, J. Wang, F. B. P. Niesler, M. Wegener, T. Koschny, and C. M. Soukoulis, "Broadband terahertz generation from metamaterials," *Nature Communications*, vol. 5, p. 3055, 5 2014.

[116] J. A. Zeitler, P. F. Taday, D. A. Newnham, M. Pepper, K. C. Gordon, and T. Rades, "Terahertz pulsed spectroscopy and imaging in the pharmaceutical setting–a review," *The Journal of Pharmacy and Pharmacology*, vol. 59, pp. 209–223, 2 2007.

[117] Y. Chen, H. Liu, Y. Deng, D. Veksler, M. Shur, al Yunqing Chen, D. B. Veksler, M. S. Shur, X.-C. Zhang, D. Schauki, M. J. Fitch, R. Osiander, C. Dodson, J. B. Spicer, and X. C. Zhang, "Spectroscopic characterization of explosives in the far-infrared region," vol. 5411, pp. 1–8, International Society for Optics and Photonics, SPIE, 9 2004.

[118] H.-B. Liu, Y. Chen, G. J. Bastiaans, and X.-C. Zhang, "Detection and identification of explosive RDX by THz diffuse reflection spectroscopy," *Optics express*, vol. 14, p. 415, 1 2006.

[119] Y. C. Shen and B. B. Jin, "Terahertz applications in the pharmaceutical industry," *Handbook of Terahertz Technology for Imaging, Sensing and Communications*, pp. 579–614, 1 2013.

[120] K. Krügener, M. Schwerdtfeger, S. F. Busch, A. Soltani, E. Castro-Camus, M. Koch, and W. Viöl, "Terahertz meets sculptural and architectural art: Evaluation and conservation of stone objects with t-ray technology," *Scientific Reports*, vol. 5, pp. 1–7, 10 2015.

[121] R. A. Lewis, "Terahertz spectroscopy: The new tool to help detect art fraud," *Faculty of Engineering and Information Sciences - Papers: Part B. 125.*, 2017.

[122] J. Ma, N. J. Karl, S. Bretin, G. Ducournau, and D. M. Mittleman, "Frequency-division multiplexer and demultiplexer for terahertz wireless links," *Nature Communications*, vol. 8, pp. 1–8, 9 2017.

[123] T. Nagatsuma, G. Ducournau, and C. C. Renaud, "Advances in terahertz communications accelerated by photonics," *Nature Photonics*, vol. 10, pp. 371–379, 5 2016.

[124] X. C. Zhang and J. Xu, *Introduction to THz wave photonics*. Springer US, 2010.

[125] S. Cibella, M. Beck, P. Carelli, M. G. Castellano, F. Chiarello, J. Faist, R. Leoni, M. Ortolani, L. Sabbatini, G. Scalari, G. Torrioli, and D. Turcinkova, "Operation of a wideband terahertz superconducting bolometer responding to quantum cascade laser pulses," *Journal of Low Temperature Physics*, vol. 167, pp. 911–916, 6 2012.

[126] L. Xu, X. C. Zhang, and D. H. Auston, "Terahertz beam generation by femtosecond optical pulses in electro-optic materials," *Applied Physics Letters*, vol. 61, p. 1784, 6 1998.

[127] D. H. Auston and M. C. Nuss, "Electrooptic generation and detection of femtosecond electrical transients," *IEEE Journal of Quantum Electronics*, vol. 24, pp. 184–197, 1988.

[128] J. A. Valdmanis, G. A. Mourou, and C. W. Gabel, "Subpicosecond electrical sampling," *IEEE Journal of Quantum Electronics*, vol. 19, pp. 664–667, 4 1983.

[129] D. H. Auston, A. M. Johnson, P. R. Smith, and J. C. Bean, "Picosecond optoelectronic detection, sampling, and correlation measurements in amorphous semiconductors," *Applied Physics Letters*, vol. 37, p. 371, 7 2008.

[130] C. Kübler, R. Huber, S. Tübel, and A. Leitenstorfer, "Ultrabroadband detection of multi-terahertz field transients with gase electro-optic sensors: Approaching the near infrared," *Applied Physics Letters*, vol. 85, p. 3360, 10 2004.

[131] J.-M. Ménard, R. Huber, and M. Porer, "Shot noise reduced terahertz detection via spectrally postfiltered electro-optic sampling," *Optics Letters*, vol. 39, pp. 2435–2438, 4 2014.

[132] S. Virally, P. Cusson, and D. V. Seletskiy, "Enhanced electro-optic sampling with quantum probes," *Physical Review Letters*, vol. 127, p. 270504, 6 2021.

[133] S.-J. Yoon, J.-S. Lee, C. Rockstuhl, C. Lee, and K.-G. Lee, "Experimental quantum polarimetry using heralded single photons," *Metrologia*, vol. 57, p. 045008, 6 2020.

[134] M. Taylor, *Quantum microscopy of biological systems*. Springer International Publishing, 2015.

[135] T. Shields, A. C. Dada, L. Hirsch, S. Yoon, J. M. R. Weaver, D. Faccio, L. Caspani, M. Peccianti, and M. Clerici, "Electro-optical sampling of

single-cycle THz fields with single-photon detectors," *Sensors*, vol. 22, p. 9432, 8 2022.

[136] S. Namba, "Electro-optical effect of zincblende," *Journal of the Optical Society of America*, vol. 51, pp. 76–79, 1 1961.

[137] C. C. Davis, *Lasers and electro-optics : Fundamentals and engineering*. Cambridge University Press, 1996.

[138] P. C. M. Planken, H.-K. Nienhuys, H. J. Bakker, and T. Wenckebach, "Measurement and calculation of the orientation dependence of terahertz pulse detection in ZnTe," *Journal of the Optical Society of America B*, vol. 18, p. 313, 3 2001.

[139] G. Bell and M. Hilke, "Polarization effects of electro-optic sampling and over-rotation for high field THz detection," *Journal of Infrared, Millimeter, and Terahertz Waves*, vol. 41, pp. 880–893, 8 2020.

[140] Z. Zhao, F. Ospald, H. Lu, D. C. Driscoll, A. Schwagmann, J. H. Smet, and A. C. Gossard, "Thickness dependence of the terahertz response in ⟨110⟩-oriented GaAs crystals for electro-optic sampling at 1.55 µm," *Optics Express*, vol. 18, pp. 15956–15963, 7 2010.

[141] A. Dreyhaupt, S. Winnerl, T. Dekorsy, and M. Helm, "High-intensity terahertz radiation from a microstructured large-area photoconductor," *Applied Physics Letters*, vol. 86, p. 121114, 3 2005.

[142] A. Dreyhaupt, S. Winnerl, M. Helm, and T. Dekorsy, "Optimum excitation conditions for the generation of high-electric-field terahertz radiation from an oscillator-driven photoconductive device," *Optics Letters*, vol. 31, p. 1546, 5 2006.

[143] J. Z. Xu and X.-C. Zhang, "Optical rectification in an area with a diameter comparable to or smaller than the center wavelength of terahertz radiation," *Optics Letters*, vol. 27, p. 1067, 6 2002.

[144] M. González-Cardel, P. Arguijo, and R. Díaz-Uribe, "Gaussian beam radius measurement with a knife-edge: A polynomial approximation to the inverse error function," *Applied Optics*, vol. 52, pp. 3849–3855, 6 2013.

[145] Q. Wu and X. Zhang, "Free-space electro-optic sampling of terahertz beams," *Applied Physics Letters*, vol. 67, pp. 3523–3525, 12 1995.

[146] S. Lin, S. Yu, and D. Talbayev, "Measurement of quadratic terahertz optical nonlinearities using second-harmonic lock-in detection," *Physical Review Applied*, vol. 10, p. 044007, 10 2018.

[147] B. M. Fischer, D. Abbott, H. Lin, and W. Withayachumnankul, "Uncertainty in terahertz time-domain spectroscopy measurement," *Journal of the Optical Society of America B*, vol. 25, pp. 1059–1072, 6 2008.

[148] A. Rehn, D. Jahn, J. C. Balzer, M. Koch, . M. Walther, P. Plochocka, B. Fischer, H. Helm, and P. U. Jepsen, "Periodic sampling errors in terahertz time-domain measurements," *Optics Express*, vol. 25, pp. 6712–6724, 3 2017.

[149] C. Fattinger, D. Grischkowsky, and M. van Exter, "Terahertz time-domain spectroscopy of water vapor," *Optics Letters*, vol. 14, pp. 1128–1130, 10 1989.

[150] X. Xin, H. Altan, A. Saint, D. Matten, and R. R. Alfano, "Terahertz absorption spectrum of para and ortho water vapors at different humidities at room temperature," *Journal of Applied Physics*, vol. 100, p. 094905, 11 2006.

[151] M. Clerici, M. Peccianti, B. E. Schmidt, L. Caspani, M. Shalaby, M. Giguère, A. Lotti, A. Couairon, F. Légaré, T. Ozaki, D. Faccio, and R. Morandotti, "Wavelength scaling of terahertz generation by gas ionization," *Physical Review Letters*, vol. 110, p. 253901, 6 2013.

[152] N. C. J. van der Valk, T. Wenckebach, and P. C. M. Planken, "Full mathematical description of electro-optic detection in optically isotropic crystals," *Journal of the Optical Society of America B*, vol. 21, p. 622, 3 2004.

[153] J. G. Skellam, "The frequency distribution of the difference between two poisson variates belonging to different populations," *Journal of the Royal Statistical Society*, vol. 109, pp. 296–296, 5 1946.

[154] H. L. Gan and E. D. Kolaczyk, "Approximation of the difference of two poisson-like counts by skellam," *Journal of Applied Probability*, vol. 55, pp. 416–430, 6 2018.

[155] C. K. Hong, Z. Y. Ou, and L. Mandel, "Measurement of subpicosecond time intervals between two photons by interference," *Physical Review Letters*, vol. 59, p. 2044, 11 1987.

[156] R. A. Campos, C. C. Gerry, and A. Benmoussa, "Optical interferometry at the Heisenberg limit with twin Fock states and parity measurements," *Physical Review A*, vol. 68, p. 023810, 8 2003.

[157] H. Kim, S. M. Lee, and H. S. Moon, "Two-photon interference of temporally separated photons," *Scientific Reports*, vol. 6, pp. 1–9, 10 2016.

[158] K. J. Resch, K. L. Pregnell, R. Prevedel, A. Gilchrist, G. J. Pryde, J. L. O'Brien, and A. G. White, "Time-reversal and super-resolving phase measurements," *Physical Review Letters*, vol. 98, p. 223601, 5 2007.

[159] J. G. Rarity, P. R. Tapster, E. Jakeman, T. Larchuk, R. A. Campos, M. C. Teich, and B. E. Saleh, "Two-photon interference in a Mach-Zehnder interferometer," *Physical Review Letters*, vol. 65, p. 1348, 9 1990.

[160] S. Slussarenko, M. M. Weston, H. M. Chrzanowski, L. K. Shalm, V. B. Verma, S. W. Nam, and G. J. Pryde, "Unconditional violation of the

shot-noise limit in photonic quantum metrology," *Nature Photonics*, vol. 11, pp. 700–703, 11 2017.

[161] A. Fedrizzi, T. Herbst, A. Poppe, T. Jennewein, and A. Zeilinger, "A wavelength-tunable fiber-coupled source of narrowband entangled photons," *Optics Express*, vol. 15, pp. 15377–15386, 11 2007.

[162] F. Bouchard, D. England, P. J. Bustard, K. Heshami, and B. Sussman, "Quantum communication with ultrafast time-bin qubits," *PRX Quantum*, vol. 3, p. 010332, 3 2022.

[163] A. Heidmann, R. J. Horowicz, S. Reynaud, E. Giacobino, C. Fabre, and G. Camy, "Observation of quantum noise reduction on twin laser beams," *Physical Review Letters*, vol. 59, p. 2555, 11 1987.

[164] F. Cui, J. Gao, P. Kunchi, C. Xue, and C. Xie, "Generation and application of twin beams from an optical parametric oscillator including an α-cut KTP crystal," *Optics Letters*, vol. 23, pp. 870–872, 6 1998.

Appendices

Appendix A

Coincidence detection

This section gives further insight into the effect of variable input pump powers on the CAR for the correlated 2 μm source. The histogram shows that the coincidences are maximal at zero delay between the photon paths and that accidental coincidences occur at successive delays of 12.5 ns i.e. the inverse of the laser pulse repetition rate. Estimation of the CAR using different input pump powers results in coincidence histograms with different characteristics for constant integration time. When operating in the photon starved regime, if the pump power P_{pump} is very low the coincidence counts are limited by residual dark counts of the detection system and uncorrelated noise photons. Figure A.1 shows an example of a typical coincidence histogram where very low pump powers are used ($P_{\text{pump}} \ll 2\,mW$).

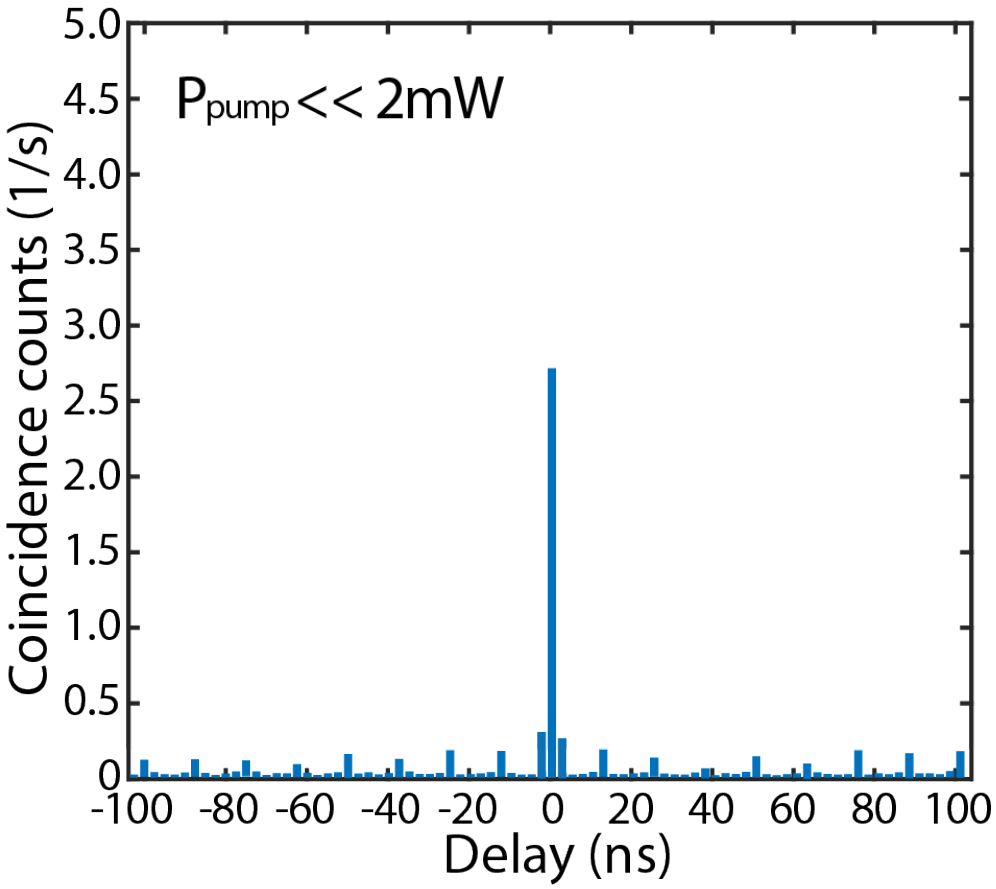

Figure A.1: Coincidence measurement histogram in the photon starved regime where very low input pump powers P_{pump} are used.

In the condition when the pump power P_{pump} is increased, the generation of multiple photons per pulse increases. The result can be observed by the increased coincidences recorded in the accidental peaks corresponding to the pulse repetition rate of the laser. The rise in the accidental counts as a result of the increased pump power, reduces the CAR by the factor inversely proportional to the P_{pump} as discussed in text. At high pump powers, the

uncorrelated noise and dark counts can be neglected in comparison with the generated SPDC photons. Figure A.2 shows this effect on a coincidence histogram where $P_{\text{pump}} \gg 40\,mW$).

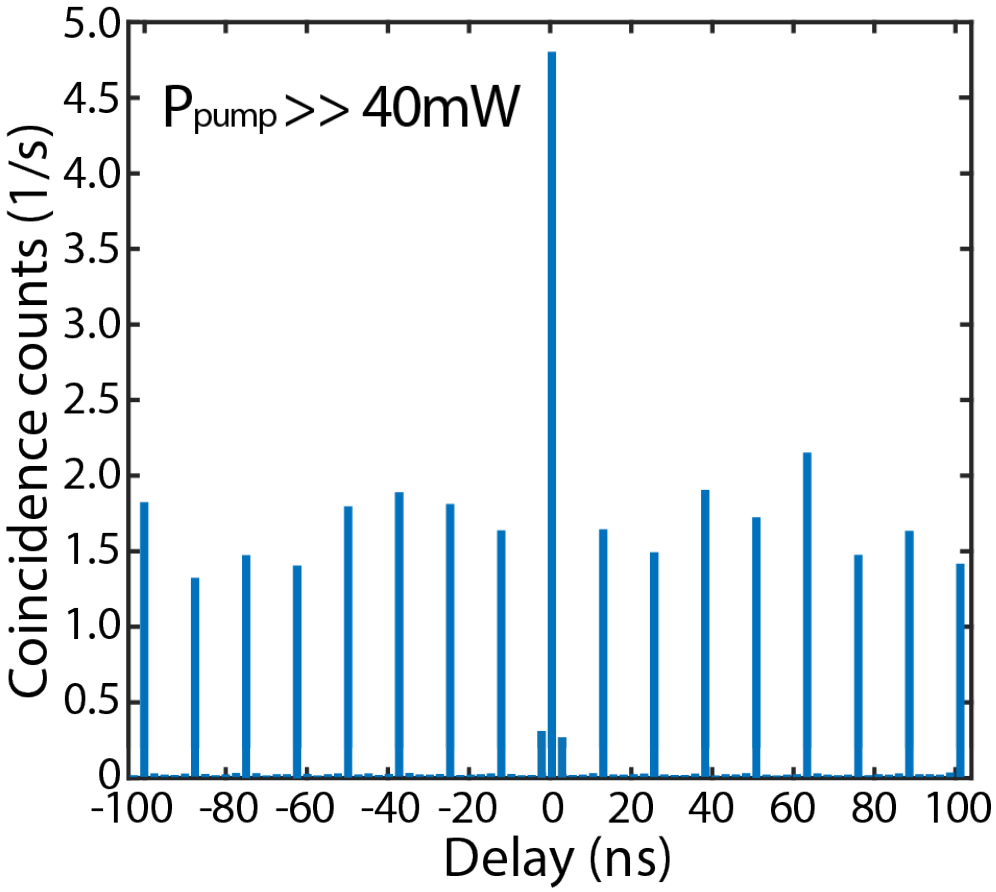

Figure A.2: Coincidence measurement histogram where higher input pump powers P_{pump} are used.

Appendix B

Characterisation of Type-2 Crystal

Due to the reduced efficiency of the Type-2 crystal compared with the Type-0 configuration, this characterisation was performed directly with single photon counting using a 50 nm filter with the SNSPD's used throughout. A reflective coupler collected the SPDC field into a SM2000 fibre directed into the same SNPSD system used throughout this work. Figure B.1 shows the characterisation of the 7 crystal poling periods using the generated singles measured with single-photon detection. For a fixed pump power, the number of single photon counts recorded using a 50 nm bandpass filter was recorded for various crystal temperatures. As with the Type-0 characterisation, temperature testing started at 30 degrees which was sufficiently above room temperature. The generation was optimised for Type-2 phase matching at a

poling period of 13.4 μm at a temperature of 110 degrees. These conditions were maintained throughout these measurements.

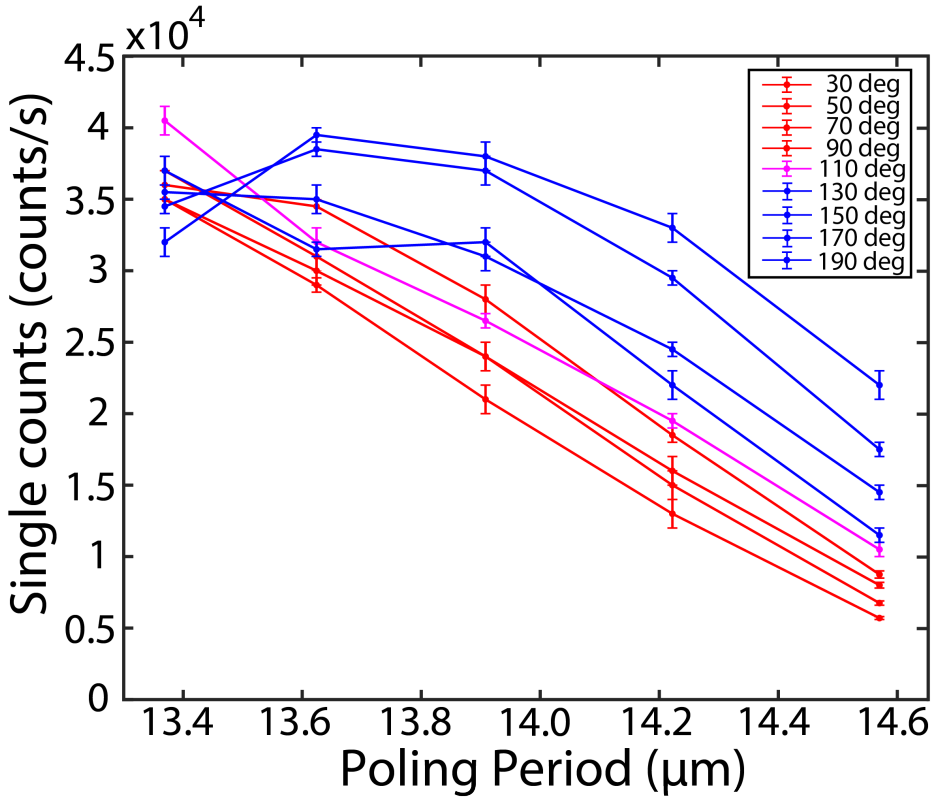

Figure B.1: Characterisation of the Type-2 PPLN crystal for possible poling periods over numerous temperatures using single counts from SNSPD's for detection.

Appendix C

Numerical Investigation on dynamic range of balanced detection

In order to better understand the experimental conditions required for the THz balanced detection with single photons, a numerical investigation was performed into how the dynamic range (DR) scales for certain photon number and integration configurations. We simulated numerically the problem of generating two Poissonian random numbers with varying average number of photon per pulse (not total measurement time) and compared the dynamic range. We expect the dynamic range of the balanced detection to scale as

$$DR = \delta\sqrt{2Nt}\,, \tag{C.1}$$

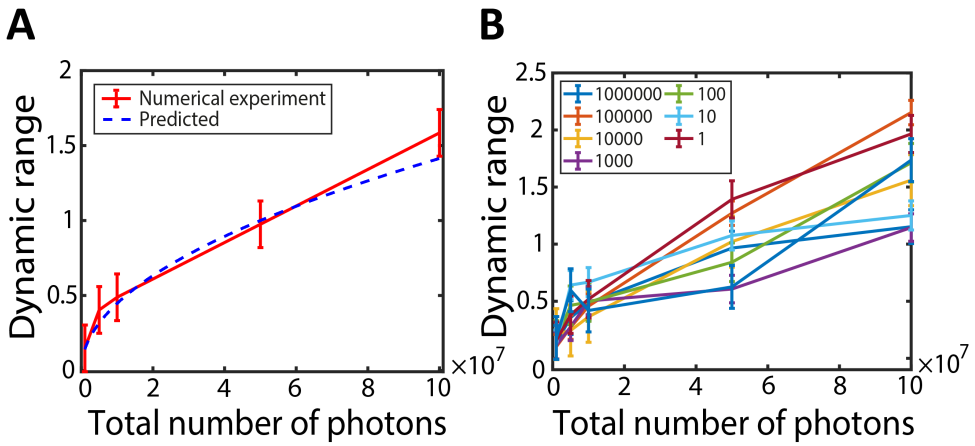

Figure C.1: Numerical problem of generating two Poissonian random numbers with varying average number of photons per pulse. Numerical results match the expected.

where $\delta = \frac{\delta Nt}{Nt}$ is the relative effect on the THz pulse on the balanced detection and Nt is the total number of photons in the measurement. Figure C.1 shows the numerical modelling of varying the number of photons per pulse and the effect on the DR. As show in the figure, there is no evidence of a dependence of the DR on such a parameter i.e. average number of photons per antenna period.

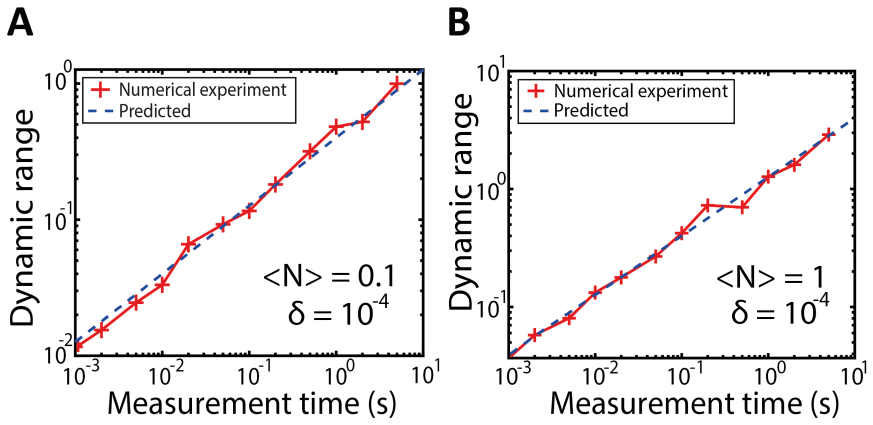

Figure C.2: Dependence of the dynamic range on the measurement time at fixed average number of photons per pulse.

Figure C.2 shows the dependence of the DR on the measurement time at fixed average number of photons per pulse $\langle N \rangle$. With fixed average of number of photons per pulse, we confirm the expected trend in equation (C.1). With DR increasing linearly with THz field and $\sqrt{N}$, the conditions on improving the DR of the measurement were better understood. The measurement can be enhanced by increasing the THz amplitude by increasing power incident on the antenna or by using a pulse picker by decreasing average power.

Conferences and awards

Conferences and workshops

2022 IEEE Photonics Society Summer Topicals Meeting Series (SUM)
Invited Conference Talk - "*Quantum optics in the infrared: Single-cycle THz fields electro-optical sampling with single-photon detectors*" Cabo San Lucas, Mexico, 11-13th July, 2022

SPIE Defense and Commerical Sensing Conference
Invited Conference Talk (Virtual) - "*Mid-infrared two-photon interference and polarization entanglement*" Orlando, Florida , 12-16th April 2021

OSA High-brightness and Light-driven Interactions Congress
Post-deadline Conference Talk (Virtual) - "*Mid-infrared Quantum Interference and Polarization Entanglement*" Prague, Czech Republic, 20th November 2020

QTech 2020 Quantum Technology International Conference
Conference Talk (Virtual) - "*Generation and detection of polarization entanglement at 2.1 micron*" Barcelona, Spain, 4th November 2020.

CLEO Europe
Conference Talk - "*Photon Pair Generation at 2.080 μm by Down-conversion*" Munich, Germany, 23 - 27th June 2019.

UK URSI Symposium 2019
Conference Talk - "*Generation and Detection of Down-converted Photon Pairs at 2.080 micrometre* National Physical Laboratory, 10th January 2019

ESGI European Study Group with industry Conference - University of Cambridge, 8-12th April 2019

ESGI European Study Group with industry Conference - University College Dublin, Ireland, 25-29th June 2018

Awards

UK-URSI Best Conference Talk Award - "*Generation and Detection of Down-converted Photon Pairs at 2.080μm*", National Physical Laboratory (NPL), January 2019

Training Courses and Outreach

Internal training courses

Labview, Python programming, Matlab programming, LaTeX, Data Management, Research Integrity, Terminalfour, Numerical Methods Demonstration, Medical Imaging Demonstration, Engineering Electromagnetics demonstration, Jupyter Notebooks, Agresso, CoreHR.

External training courses

Artificial Intelligence and Machine Learning – MIT Online Course, 30-31st August 2018

Introduction to Julia – MIT Online Course, 13-14 August 2018

Terahertz Technology and Applications – National Physical Laboratory (NPL), 11-12 April 2019

Outreach

UoG Quantum Technology Summer School - School of Engineering, University of Glasgow, 11-12th September 2019